2020

IDENTIFICATION OF ADSORBATE FT-IR BANDS USING IN-SITU TECHNIQUES: Pd SPECIATION AND ADSORPTION CHEMISTRY OF Pd-ZEOLITES FOR PASSIVE NOx ADSORPTION

Robert Bruce Pace III
University of Kentucky, robert.pace@uky.edu
Author ORCID Identifier:
https://orcid.org/0000-0002-2764-2631
Digital Object Identifier: https://doi.org/10.13023/etd.2020.483

STUDENT AGREEMENT:

I represent that my thesis or dissertation and abstract are my original work. Proper attribution has been given to all outside sources. I understand that I am solely responsible for obtaining any needed copyright permissions. I have obtained needed written permission statement(s) from the owner(s) of each third-party copyrighted matter to be included in my work, allowing electronic distribution (if such use is not permitted by the fair use doctrine) which will be submitted to UKnowledge as Additional File.

I hereby grant to The University of Kentucky and its agents the irrevocable, non-exclusive, and royalty-free license to archive and make accessible my work in whole or in part in all forms of media, now or hereafter known. I agree that the document mentioned above may be made available immediately for worldwide access unless an embargo applies.

I retain all other ownership rights to the copyright of my work. I also retain the right to use in future works (such as articles or books) all or part of my work. I understand that I am free to register the copyright to my work.

REVIEW, APPROVAL AND ACCEPTANCE

The document mentioned above has been reviewed and accepted by the student's advisor, on behalf of the advisory committee, and by the Director of Graduate Studies (DGS), on behalf of the program; we verify that this is the final, approved version of the student's thesis including all changes required by the advisory committee. The undersigned agree to abide by the statements above.

Robert Bruce Pace III, Student

Dr. Mark Crocker, Major Professor

Dr. Yinan Wei, Director of Graduate Studies

IDENTIFICATION OF ADSORBATE FT-IR BANDS USING IN-SITU TECHNIQUES: Pd SPECIATION AND ADSORPTION CHEMISTRY OF Pd-ZEOLITES FOR PASSIVE NO_X ADSORPTION

DISSERTATION

A dissertation submitted in partial fulfillment of the
requirements for the degree of Doctor of Philosophy in the
College of Arts and Sciences
at the University of Kentucky

By

Robert Bruce Pace III

Lexington, Kentucky

Co- Directors: Dr. Mark Crocker, Professor of Chemistry

and Dr. John P. Selegue, Professor of Chemistry

Lexington, Kentucky

2020

https://orcid.org/0000-0002-2764-2631

ABSTRACT OF DISSERTATION

IDENTIFICATION OF ADSORBATE FT-IR BANDS USING IN-SITU TECHNIQUES: Pd SPECIATION AND ADSORPTION CHEMISTRY OF Pd-ZEOLITES FOR PASSIVE NO_X ADSORPTION

To meet increasingly stringent automotive emissions standards, further improvements in catalytic converter design are necessary. Current automotive catalyst systems are effective at eliminating emission of nitrogen oxides (NO_x) once the catalyst reaches operational temperature (~200 °C). NO_x emitted at lower catalyst temperatures now comprises most of the NO_x released during a typical test cycle. Referred to as "the cold start problem" this issue has come to the forefront of automotive catalyst development, as mitigating these emissions is necessary to further reduce automotive emissions. Passive NO_x adsorbers present an appealing solution to the cold start problem, these being a class of materials that chemisorb exhaust components such as NO_x, carbon monoxide (CO) and hydrocarbons at near-ambient temperatures, and then desorb these compounds once the downstream catalyst has reached operational temperature. An effective passive NO_x adsorber must have several properties: high NO_x adsorption at near-ambient temperatures, near-complete NO_x desorption at temperatures within the operational range, high thermal stability, and resistance to automotive exhaust components at high temperatures. The potential environmental impact of such a system is substantial, as NO_x emissions currently result in the formation of millions of tons of smog and acid rain each year.

Pd-exchanged zeolites have shown promise for deployment as Passive NO_x adsorbers, though much remains to be understood about their adsorption chemistry and deactivation. In-situ Diffuse Reflectance Infrared Fourier Transform Spectroscopy (DRIFTS) provides a convenient probe of adsorbed species, most automotive exhaust components possessing IR-active chemical bonds. By examining the evolution of IR bands under various pretreatments and adsorbates, the overall Pd-speciation and adsorptive zeolite sites of each material can be characterized, and the identities of IR bands can be deduced. In this work, microreactor-MS analysis of the adsorption and desorption behavior of these materials was also examined, these results being coupled with in-situ DRIFTS temperature programmed desorption (TPD) to correlate desorption events with specific adsorbed species.

A pair of zeolite frameworks of similar Si/Al ratio but differing pore size were examined, Beta zeolite (BEA) and Chabazite (CHA) representing a medium- and small-pore framework, respectively. The effect of Pd-loading on BEA was examined, as well as the various deactivation pathways and active sites of each material.

KEYWORDS: Passive NO_x Adsorber, Automotive Catalysis, Environmental Catalysis, Palladium, Zeolite, DRIFTS

Robert Bruce Pace III

11/16/2020

Date

IDENTIFICATION OF ADSORBATE FT-IR BANDS USING IN-SITU TECHNIQUES: Pd SPECIATION AND ADSORPTION CHEMISTRY OF Pd-ZEOLITES FOR PASSIVE NO_X ADSORPTION

By
Robert Bruce Pace III

Mark Crocker
Co-Director of Dissertation

John P. Selegue
Co-Director of Dissertation

Yinan Wei
Director of Graduate Studies

11/16/2020
Date

DEDICATION

To my wife Stephanie, without whom none of this would have been possible.

ACKNOWLEDGMENTS

This dissertation represents an individual work, though without the contributions of others it would never have come about. First and foremost, I would like to thank my committee chair, Dr. Mark Crocker for his insight, wisdom, and patience in guiding me through my time as a graduate student. I would also like to thank my co-chair Dr. John Selegue for his unerring ability to always find that one reference that helps my data make sense. I would also like to thank Dr. Marcelo Guzman and Dr. Yang-Tse Cheng for their insight and commentary that has helped keep me on course to graduation.

I would also like to thank Mr. Trevor Lardinois and Dr. Raj Gounder for their significant intellectual and experimental contributions to this work, their efforts in material preparation and characterization serve as the foundation for the work presented here. I would also like to thank Dr. Yaying Ji for her contributions to this work, her initial studies have been invaluable for the interpretation of data collected in the later stages of this effort. This project involved many collaborations, and I would specifically like to thank Prof. Alexis T. Bell, Dr. Jeroen Van der Mynsbrugge, Dr. Andrew "Bean" Getsoian, Dr. Joe Theis, Dr. Christine Lambert, and Dr. Olivier Heinz who all contributed to this work either intellectually or through experimental data. I would also like to thank Dr. Eduardo Santillan-Jimenez for his advice and guidance. Finally, I would like to thank the U.S. Department of Energy for funding this work.

TABLE OF CONTENTS

LIST OF TABLES

LIST OF FIGURES

CHAPTER 1. INTRODUCTION

1.1 Automotive Catalytic Conversion Systems

Internal combustion engines have facilitated the rapid development of the industrialized world for over a century, though only now are the full implications and negative impact of this technology being adequately understood. Combustion of hydrocarbon fuels leads to the formation of a distribution of undesirable byproducts, including particulate matter, partially combusted hydrocarbons, carbon monoxide (CO), carbon dioxide (CO_2), an assortment of nitrogen oxides (NO_x), along with other byproducts such as hydrogen (H_2) and sulfur compounds. Some of these species are especially problematic; annually millions of tons of NO_x is emitted and these species react with ozone and hydrocarbons, and with water, to generate photochemical smog (NO_2) and acid rain (HNO_3), respectively.[1] To reduce the emission of these species, automotive catalytic converters were developed to convert NO_x, CO, and hydrocarbons to more benign CO_2, water, and N_2 under the necessary operational conditions of the vehicular exhaust stream. Since a wide variety of engine types and fuels exists, a wide range of catalytic converter technologies have also been developed to meet the specific needs of each vehicle and fuel type. However, factors in automotive development such as greater fuel-efficiency, and thus lower operating exhaust temperatures, are driving these technologies to their functional limits.[2, 3]

One of the most important aspects of catalytic converter design is the air-to-fuel ratio the intended engine system requires, three typical ranges being established: a reducing or rich regime where oxygen is the limiting reactant, an oxidizing or lean regime where CO and hydrocarbons are the limiting reagent, and finally a stoichiometric regime in which the quantity of oxygen is stoichiometrically adequate to convert all of the available CO and hydrocarbons to CO_2. Each of these conditions has advantages, and some catalyst technologies even require various stoichiometries to provide for catalyst regeneration. Generally speaking, two strategies have been employed in both engine development and NO_x reduction strategy, one being the lean-burn diesel engine coupled with a diesel oxidation catalyst (DOC) followed by lean NO_x-trap (LNT) and or selective

catalytic reduction (SCR) systems, in addition to stoichiometric gasoline engines that employ a three-way catalyst (TWC) to reduce NO_x. Stoichiometric gasoline engines represent the bulk of small, general-use vehicles on the road today.

1.1.1 Modern Technologies

1.1.1.1 LNT-SCR systems

Lean-burn diesel vehicles employ a series of catalytic conversion technologies, each performing a different function in the exhaust treatment process. First, a diesel oxidation catalyst (DOC) uses supported platinum group metals to oxidize CO, hydrocarbons and particulate matter to CO_2, while also having the disadvantageous side effect of oxidizing most NO to NO_2.[4-6] Since the oxidation catalyst eliminates any reducing species from the exhaust stream, the problem of NO_x reduction can be approached in two ways; either by adding a reductant to the gas stream to be used in the reduction of NO_x, or by storing NO_x to be reduced under a deviation to rich conditions. The former method represents the process implemented in a SCR system, while the latter describes a LNT system.[7, 8]

SCR systems are employed primarily on larger vehicles due to the necessity of carrying an additional quantity of reductant which is introduced to the exhaust from an external tank. Commonly called diesel exhaust fluid (DEF), this reductant is either aqueous ammonia or urea.[8] Three reactions (Equations 1-3) are involved in the SCR process, the first being the most prevalent:

$$4NH_3 + 4NO + O_2 \rightarrow 4N_2 + 6H_2O \qquad (1)$$

$$2NH_3 + NO + NO_2 \rightarrow 2N_2 + 3H_2O\ (fast) \qquad (2)$$

$$8NH_3 + 6NO_2 \rightarrow 7N_2 + 12H_2O\ (very\ slow) \qquad (3)$$

Depending on the application, various catalysts have been employed in this process. Stationary lean-burn engines have typically been outfitted with catalysts consisting of vanadium oxide supported on titania with a tungsten oxide promoter.[9] While this catalyst achieves excellent NO_x reduction at intermediate temperatures, at

higher temperatures it can lead to the oxidation of ammonia, formation of SO_3, as well as N_2O.[10] Conversely, at lower temperatures this system has insufficient NO_x conversion to meet modern emission standards. While conversion can be improved by increasing vanadium loading, this also yields a corresponding decrease in selectivity to N_2.[8] Other metal oxides have been investigated for their activity in this process, as NO_x reduction at lower temperatures would also be advantageous for stationary internal combustion systems.[11] Manganese oxide materials have received special attention, though their usefulness is limited by the heavily phase-dependent nature of their activity.[11, 12] The introduction of various metal oxides as dopants served to remediate some of these issues; iron, copper and ceria all stabilize the active phase of the catalyst, and thus improve the low-temperature NO_x conversion.[13, 14]

More recently, metal-exchanged zeolites have attracted significant attention, Fe-ZSM-5 and Cu-SSZ-13 being shown to have excellent high- and low-temperature NO_x conversion, respectively. These materials have higher NO_x conversion efficiencies than metal oxide catalysts, making them candidates for meeting future emissions targets.[10, 15] Some metal-zeolite formulations have other advantageous properties such as reduced ammonia slip, or ammonia released by the exhaust, as well as enhanced low-temperature activity when copper is employed as the active metal.[16, 17] Further, the preparation technique was found to exert influence over the activity of the materials, sublimation of $FeCl_3$ being found to produce a more resilient active phase in Fe-based formulations.[18]

The differing active temperature ranges of SCR catalysts can be understood by examining the mechanistic pathways that have been proposed to occur on these materials. Two potential pathways have been proposed for the metal oxide-type catalysts, one being a Langmuir-Hinshelwood mechanism involving ammonia and adsorbed nitrate species, and the other being the more generally accepted Eley-Rideal mechanism, in which ammonia is adsorbed at Lewis acid sites that react with gaseous NO and NO_2. Mechanistic considerations for metal-loaded zeolites are more complex, reactions being intermediated by N_2O_3 in the case of an active MnO_x phase, while other materials possess active copper or iron ions as well as metal oxide oligomers.[19-22]

As mentioned above, much of the NO present in the exhaust feed is converted to NO_2 by the DOC upstream from the SCR system. Since reduction of NO_2 only occurs through the fast SCR reaction, and since this reaction is kinetically favorable at low temperatures, special attention must be paid to the mechanisms through which this reaction proceeds.[23] Zeolites have been shown to have high fast SCR activity through a variety of intermediates depending on the metal present.[19, 20] However, SCR catalysts alone still present several disadvantages in the engineering and upkeep required to maintain the catalyst.

LNT catalysts were initially developed as an alternative to SCR technologies. LNT catalysts must exhibit several functionalities.[24, 25] The operation of these systems can be broken down into three steps, the first being oxidation of NO to NO_2, though this reaction is kinetically limited at low temperatures.[26, 27] Enhancement of oxidation activity is achieved through addition of Pt or Rh, the prototypical LNT formulation being $Pt/BaO/Al_2O_3$.[28] The next step in the process is storage of NO_2 as nitrates or nitrites on a basic metal oxide such as BaO. While enhancing the Ba loading to increase the capacity of these materials is attractive, increased Ba loading has been shown to result in interactions with platinum and decreased oxidation activity either by blocking active Pt sites, or by stabilization of Pt oxides.[29, 30] The oxidation of NO to NO_2 is of critical importance as only nitrates appear on these materials in spectroscopic studies at temperatures above 200 °C, an indication that NO does not interact with these materials at operational temperatures; nitrites (indicative of NO adsorption) only being observed at lower temperatures.[31-33] However, when an oxidative component is added to these materials, nearly identical behavior is observed whether NO or NO_2 is supplied at high temperatures when the oxidation reaction is not kinetically limited.[34] Additionally, Pt and Ba have been found to interact to provide additional NO_x storage capacity at the Pt-Ba interface, nitrites being preferentially converted to nitrates in the presence of oxygen.[27] Unfortunately, other exhaust species are problematic for these materials and the initial state of the trapping medium also exerts an influence, the reactivity of Ba species to NO_2 being in the order oxide > hydroxide > carbonate.[35] This presents a significant challenge to the operation of these materials as CO, CO_2, and water all

compete for adsorption sites or contribute to the loss of NO_2 through alternative reduction pathways.[36]

The final step of the LNT process is the desorption and reduction of stored NO_x, decomposition of nitrates achieved by the equilibrium change associated with deviation to rich conditions, followed by reduction of the released NO_x achieved by reductants adsorbed at precious metal sites.[27] The most challenging aspect of this process is the rapid reduction of a large quantity stored NO_x, though these materials have demonstrated remarkable effectiveness in carrying out this reduction. The mechanism by which this reaction proceeds is still debated.[30]

LNT catalysts also present problems with deactivation, increasing NO_x and ammonia slip being observed as the catalyst is aged.[37] To resolve these issues, tandem LNT-SCR systems were demonstrated to have a high degree of effectiveness while still eliminating the need to introduce an external reductant for SCR activity.[7, 24, 37] In this configuration, the LNT catalyst produces ammonia, which is adsorbed on the SCR catalyst under rich conditions and serves as a NO_x reductant in lean mode, thus reducing NO_x that fails to adsorb on the LNT material. Cu-chabazite SCR materials are especially advantageous for this configuration as they can also reduce NO_x using adsorbed hydrocarbons as reductant while also limiting N_2O slip.[7, 38, 39]

1.1.1.2 TWC systems

Stoichiometric gasoline engines require different pollutant mitigation strategies due to the nature of the fuel and exhaust stream. The only catalytic system capable of meeting modern emissions standards in gasoline vehicles is the three-way catalyst (TWC), so called because of the three functionalities the catalyst possesses.[40, 41] These materials are composed of a high-surface-area alumina material washcoated onto a monolith, which serves as a support for the active metals, while Pt, Pd, and or Rh comprise the active supported metals, and finally Ce/Zr mixed oxides act to store oxygen for release under rich conditions.[40, 42-44] These catalysts are active in three catalytic processes: reduction of NO_x to N_2, oxidation of CO to CO_2, as well as oxidation of hydrocarbons to CO_2. These catalysts are also active in the steam reforming and water

gas shift reactions that produce CO and H_2, and H_2 and CO_2 respectively.[40, 41] Stoichiometric conditions provide H_2, partially combusted hydrocarbons, and CO as reducing agents with oxygen and NO_x providing the oxidative counterbalance. The air-fuel equivalence ratio is commonly denoted by λ, or the ratio of the current air-fuel ratio to the stoichiometric value. An air/fuel ratio of 14.7 represents a stoichiometrically equal quantity of oxidants and reductants by weight, while the formula used to derive λ is presented in Equation 4.[45] A λ value of 1 therefore represents stoichiometric conditions, while a λ of less than 1 or greater than 1 indicates rich and lean conditions, respectively. The λ of the automotive exhaust is measured by sensors both before and behind the catalyst bed and is controlled by the fuel injection system through a feedback loop that oscillates slightly above and below true stoichiometry.[40] This oscillation is beneficial to maintaining the catalyst's NO_x reduction functionality by preventing total oxidation of the NO_x reduction component, while still achieving oxidation under rich conditions through the oxygen storage function of the Ce/Zr oxides incorporated in the catalyst washcoat.[46, 47]

$$\lambda = \frac{\mathrm{Air/Fuel}_{current}}{\mathrm{Air/Fuel}_{stoichiometric}} \quad (4)$$

The noble metal or metals deposited on the catalyst determine the functions the catalyst can perform. The most important metal for the NO_x reduction process is Rh, this metal's ability to dissociatively adsorb NO into adsorbed N and O atoms being a key feature of the NOx reduction process. The adsorbed N atoms then combine to form N_2, while adsorbed C and O combine to form CO_2. Molecularly adsorbed NO is also capable of reacting with the adsorbed N atoms to form N_2 and adsorbed O.[48-50] The adsorbed O atoms can then combine with adsorbed CO to form CO_2 via a Langmuir-Hinshelwood mechanism.[51] As the exhaust composition fluctuates from rich to lean conditions, Rh is oxidized from its metallic state to form Rh oxides, which have been shown to be less effective at adsorbing NO_x and CO.[51] As a result, preventing over-oxidation of Rh is of prime importance to maintaining NO_x conversion efficiency, thus limiting this technology to operation under stoichiometric conditions. Addition of Pt to the catalyst such that both Pt and Rh sites are present greatly enhances the conversion of CO over these materials by enhancing oxidation activity.[52] Recent developments in this

technology have focused on the development of Pd-only TWCs due to the increasing costs of Pt and Rh. The development of Pd-catalysts accompanied various engine design changes that allowed the catalyst to be placed closer to the engine, and therefore achieve a higher operating temperature. This advantage serves to mitigate the negative impacts of removing Rh and Pt from the catalyst and has led to widespread adoption of this technology.[53] Additional developments in washcoat components and trimetallic formulations have also been explored.[53]

Various undesirable side reactions can also occur on these materials, including the formation of ammonia and SO_3. These products are yielded by oxidation of SO_2 and by over-reduction of NO_x with H_2. Ammonia is undesirable due to its noxious odor while SO_3 is corrosive and can damage exhaust components, though trimetallic catalyst formulations have shown excellent selectivity toward N_2 and SO_2.[40, 44, 51, 53] Automotive catalysts must show exceptional durability due to the long lifetimes and harsh conditions demanded by their operational conditions. Various deactivation paths have been studied over exhaust treatment materials, with metal particle agglomeration, heavy metal poisoning if leaded gasoline is used, support degradation by thermal stress and fouling all being important considerations. Fuel contaminants such as sulfur, fuel and engine oil additives, and corrosion products can all harm the function of the catalytic converter.[54] As a specific example, high fuel concentrations of sulfur can lead to the formation of sulfates on ceria that either remain adsorbed, thus blocking adsorption sites, or are eliminated as H_2S, a foul-smelling gas. The blocking of adsorption sites by sulfates was found to be limited when zirconia is employed as an additive to ceria.[43, 55]

1.1.2 The Cold Start Problem

Catalytic converter technologies that reduce NO_x have achieved nearly universal adoption, leading to a 44% decrease in anthropogenic NO_x emissions in the United States between 1991 and 2011.[56] Modern catalysis technologies are capable of achieving excellent results in both NO_x reduction and CO oxidation, nearly complete conversion being achieved under ideal operating conditions. However, emissions standards continue to become more stringent and in the face of an ever-growing fleet of vehicles and stationary NO_x sources, near-total elimination of NO_x from exhaust streams is of

increasing importance. Considering the effectiveness of modern catalytic systems, further improvement is an especially difficult challenge and must involve enhancement of NO_x conversion outside of the optimal performance regions of current technologies.

The most attractive area for catalyst improvement is in the initial phases of vehicle startup. During this period, that concerns only the first seconds of vehicle operation, the catalyst is in a temperature regime where the reactions it typically catalyzes are kinetically limited, thus the catalyst is largely ineffective at NO_x reduction. This difficulty is commonly referred to as "the cold-start problem" or, the need to bring the catalyst to its operating temperature as quickly as possible. Catalyst heaters and operation under rich conditions (additional combustion leading to higher temperatures) have both been evaluated to achieve faster temperature increase, but additional engineering controls and operation with excess fuel are undesirable in the context of efforts to improve fuel economy. A more attractive pathway for improvement is to enhance the low-temperature effectiveness of the catalyst system, though other materials must be considered. LNT systems are somewhat effective at lower temperatures, and thus present an appealing starting point for further development, though the reactivity limitations at near-ambient temperatures suggest passive adsorption as a more realistic option. Such a passive NO_x adsorber (PNA) material would ideally be placed upstream from the current catalyst and adsorb NO_x and other pollutants at low temperature, then desorb these species at elevated temperatures, at which point the downstream catalyst is active.

1.1.3 Passive NO_x Adsorbers

The PNA concept was described as early as 1997, initial efforts focusing on the employment of mixed metal oxides.[57] This concept is advantageous in several respects, as it requires no additional monitoring or controls and is broadly applicable to a variety of engine systems. However, the usual durability requirements of automotive catalysts still apply to any material to be deployed as a PNA. Specifically, any PNA material candidate must exhibit high hydrothermal stability, high NO_x storage at near ambient temperatures, operability in the presence of competing adspecies such as water, and durability under typical operating conditions.[58] Also of importance to PNA function is the ideal NO_x desorption temperature range, in which little NO_x desorbs below ~200 °C, while all NO_x

must desorb by the maximum operating temperature of the system. Any species that remains adsorbed above this temperature would effectively poison the PNA active sites, and thus decrease the longevity and effectiveness of the material by blocking adsorption sites during the next cold-start event.[59] Further, any PNA must also have a high-rate of NO_x adsorption, this being necessary to handle the large volume and high flow rate of the exhaust gas while limiting the quantity and thus cost of the PNA material. Early PNA formulations included Pt and Pd on alumina, ceria, ceria/zirconia mixed oxides, as well as alumina-supported copper oxide, nickel oxide and chromium oxide.[57, 60-64] More recent formulations have included the use of silver as the active storage component, in addition to Pd-promoted tungstated zirconia, along with other metal support combinations.[59, 62, 63, 65-67]

Studies of Pt and Pd on ceria and alumina have found overall greater NO_x storage over Pt formulations due to the ability of Pt to store NO_x as both nitrites and nitrates, while mainly nitrites are observed on Pd formulations.[62, 64, 68] Nitrates are more thermally stable and are thus undesirable as their desorption point is near the maximum of ideal catalyst operating temperatures.[69] Pd-based catalysts therefore achieve greater total NO_x desorption and received further attention, lean environments being found to greatly enhance NO_x storage capacity while also maintaining the active sites on the ceria support.[70] However, ceria materials show a high sensitivity to poisoning by sulfur through formation of sulfates that are more thermally stable than nitrates.[71] This is problematic for the use of metal oxide supports as regeneration from sulfur poisoning is difficult, although increasing catalyst acidity through the use of rare-earth promoters has been shown to improve sulfur resistance on MnO_x-based materials.[67]

Another group of materials that has attracted significant attention for employment as PNA's are Pd-loaded zeolites, the high NO_x desorption efficiency of Pd and high sulfur tolerance of the zeolite support being especially appealing. Rather than acting as a support for either metallic or metal oxide particles, zeolites provide sites where metal ions can ion exchange directly at zeolite Al-O(H)-Si species, providing higher metal dispersion and thus greater NO_x storage capacity than is achievable on other materials.[72] Other properties of the zeolite are also desirable for these applications, the

aluminosilicate framework providing a high degree of thermal stability, especially in small-pore zeolites whose internal cavities are too small for dealumination reactions to readily occur in the presence of water.[73] The Si/Al ratio of the zeolite is an important factor in determining the speciation of the supported metal as well as the overall stability of the framework. Zeolites with lower Si/Al ratio have a greater abundance of Al sites, and therefore a greater abundance of aluminum sites that occupy next-nearest-neighbor (NNN) and next-next-nearest neighbor (NNNN) positions to other Al atoms and are therefore able to support divalent metal cations.[72, 74] Since dealumination reactions are the primary pathway of hydrothermal degradation, low Si/Al ratio materials are also more susceptible to deactivation. Conversely, high Si/Al ratio materials show a greater abundance of isolated Al sites that can support a monovalent metal ion, though the overall abundance of metal-exchange sites is also lower in these materials.[75] Therefore, intermediate Si/Al zeolites are desirable for this application as these materials balance the number of active sites with the stability of the material. However, the distribution of sites and metal speciation is more complex on these materials, and thus their mechanism of action is more ambiguous.[76]

Another important parameter in the metal-zeolite interaction is the crystallographic nature of the framework and the number of distinct positions within the framework that Al can occupy. Relatively simple frameworks such as chabazite (CHA) possess only a single crystallographically unique Al or "T" site, so called because of the tetrahedral coordination geometry of the trivalent Al atom.[77] More complex materials have an abundance of distinct T sites; for example, beta (BEA) zeolite has nine such sites. The pore size is also important as this parameter influences reactivity through the limitations placed on the size of molecules that can be included within the zeolite framework. Discussion of the specific details of the chemistry that occurs over these materials is facilitated by an introduction of the various characterization techniques that are most prevalently employed to make these assessments.

1.2 Analytical Techniques

An array of analytical techniques has been used to study metal-loaded zeolites employed as PNA materials and on metal-loaded zeolites more broadly. Typical catalyst characterization techniques are applicable to these materials, including pore volume analysis by N_2 physisorption coupled with the Brunauer-Emmett-Teller (BET) adsorption isotherm, metal reducibility analysis by H_2 temperature-programmed reduction (TPR), as well as a wide array of in-situ adsorption and desorption techniques. Various detectors are employed in these experiments, including infrared spectrometers (FT-IR), mass spectrometers (MS), and thermal conductivity detectors (TCD). FT-IR and MS techniques are especially useful as these methods allow for the identification of specific molecules that adsorb and desorb from the experimental material, temperature-programmed desorption (TPD) being the primary method by which NO_x storage is quantified. Other techniques are useful in the study of the zeolite framework, including ^{27}Al magic-angle spinning nuclear magnetic resonance spectroscopy (MAS-NMR), a method that allows the identification of variously coordinated Al within the zeolite framework. X-ray diffraction (XRD) is a useful probe of the crystallinity of the zeolite framework and provides a convenient tool to assess the extent of zeolite degradation.

Analyzing the supported metal is especially important in the design of catalytic systems, Pd being appealing for use as a PNA metal for reasons enumerated above. Generally, X-ray techniques have been used to study Pd speciation, especially X-ray photoelectron spectroscopy (XPS), though these studies are often complicated by the high degree of band overlap between the various Pd species. Further complicating differentiation of Pd 3d XPS bands is the low concentration of Pd typically supported by the zeolite framework, and thus low intensity of the Pd 3d bands. Another useful, if underutilized, technique for analyzing Pd speciation is electron paramagnetic resonance (EPR) spectroscopy, which can be used to ascertain the presence and quantity of paramagnetic Pd ions such as Pd^{+} and Pd^{3+}.

By far, the most convenient probe of the reactivity of Pd-loaded zeolites is in-situ diffuse-reflectance FT-IR spectroscopy (DRIFTS), a technique that allows direct observation of surface adsorbates that have IR-active chemical bonds. Fortunately, the IR

spectra of NO_x, CO, and a plethora of other species have been extensively characterized by this method, CO adsorption being instrumental in the elucidation of Pd speciation. DRIFTS is the primary analytical technique employed in this contribution, though each of the techniques described above will be used to provide further context and information to aid in deriving DRIFTS band assignments.

1.2.1 In-situ DRIFTS and Microreactor Studies

Specific experimental procedures employed for this work are provided in Appendix 1, though generally experiments in both the DRIFTS and microreactor systems can be described by three steps: pretreatment in either inert or active atmosphere at high temperature followed by cooling to near-ambient temperatures, adsorption of a desired probe gas at near-ambient temperatures, and finally desorption of the probe molecule via TPD with a ramp rate of 10 °C/min. The literature is rich with IR spectroscopy studies of adsorbate molecules on zeolites and Pd-loaded zeolites specifically, though much disagreement remains as to the identities of many of the observed IR bands. Discussion of these apparent inconsistencies will be outlined in detail below, especially revolving around the adsorption of CO and NO as probe molecules.

1.2.1.1 Adsorption of Carbon Monoxide on Pd-loaded Zeolites

The identification of active metal and zeolite sites using CO as a probe molecule dates to the early 1970s, with analysis of many zeolite IR-active bonds also being of paramount significance.[78, 79] A seminal study by Naccace et al. examined the behavior of Pd-Y zeolite under various conditions and established the presence of Pd in oxidation states of +1, +2, and +3, the odd-numbered ions being examined by EPR. The zeolite in this study was of a Si/Al ratio of ~4, so most of the Pd can be assumed to be Pd^{2+} due to the high abundance of proximal Al sites. This led the authors to conclude that the Pd^{+} and Pd^{3+} observed by EPR occurred in concentrations too low to account for any of the observed CO bands.[78] The observed $Pd^{n+}(CO)$ bands occurred at 2135 and 2110 cm^{-1} and were assigned by the authors as CO adsorbed at two different Pd^{2+} sites. Upon a temperature increase, these species are found to shift to lower wavenumbers, this shift being proposed to result from the formation of $Pd^{2+}(CO)_2$ species at elevated

temperature.[78] Additional studies on low Si/Al ratio zeolites (Si/Al <10) have been conducted by Khivantsev et al., $Pd^{n+}(CO)$ bands of the type $Pd^{2+}(CO)_2$ (2193-2214 cm^{-1}), $Pd^{2+}(CO)$ and $Pd^{2+}(CO)(OH)$ (2115-2150 cm^{-1}), and $Pd^{+}(CO)$ at 2075 cm^{-1} all observed, although a later contribution amended this last assignment to $Pd^{0}(CO)$ species, an assignment more consistent with other reports.[72, 74] The identities of the $Pd^{2+}(CO)_2$ bands bear further examination, the CO stretching frequencies of this species being substantially above the gas-phase stretching frequency of the CO molecule. This Pd species is classified as a "super-electrophile" by Khivantsev et al., analogous to the inorganic complex $[Pd(CO)_4][Sb_2F_{11}]_2$ synthesized by Willner et al. that also expresses symmetric and asymmetric CO stretches at 2212 and 2189 cm^{-1} respectively.[74, 80] Such a label indicates that the Pd in question is adequately electrophilic to eliminate π-backbonding with the coordinated CO molecules. In its inorganic complex form, this Pd species is highly reactive to water, though Khivantsev et al. observed a remarkable stability of this Pd even when water is present in a small pore SSZ-13 zeolite with Si/Al ratio of 6.[74] The super-electrophilic Pd is found to dominate the FT-IR spectrum after CO adsorption onto low Si/Al SSZ-13 materials, the stability of this species being proposed to result from the small pore diameter of this material.[74] The connectivity of this species to the framework is still unclear, though a "pore confinement" effect has been proposed, rather than a more classical exchange at Si-O(H)-Al sites. In previous studies, CO bands in this region were assigned to species associated with Pd^{3+} ions, though EPR studies have shown inadequate quantities of Pd^{3+} to support this assignment considering the intensity of the observed Pd(CO) bands.[75, 76, 81, 82]

Intermediate Si/Al zeolite materials show a more complex CO band structure than those observed for low Si/Al materials, super-electrophilic $Pd^{2+}(CO)$ bands still being observed, though they are often less stable and less abundant.[76, 82] A greater number and intensity of $Pd^{n+}(CO)$ bands occurs in the range 2110–2185 cm^{-1}, the identities of these species being variously assigned to $Pd^{+}(CO)$, $Pd^{2+}(CO)$, and $Pd^{2+}(CO)(OH)$, though disagreement exists as to the exact range and behavior of each of these proposed species.[74, 76, 78, 82] CO-TPD analysis of various zeolite frameworks with similar Si/Al showed a pair of $Pd^{n+}(CO)$ bands that remain to higher temperatures, though these were not observed to decrease in wavenumber upon CO desorption as shown on the low Si/Al

material described above.[76] As a result the authors assign these bands to CO adsorbed on "naked" $Pd^{+/2+}$ ions exchanged onto the zeolite framework, while the other $Pd^{n+}(CO)$ bands in this range are assigned to Pd with active oxygen ligands, presumably $[Pd^{2+}(OH)]^{+}$. Conversely, a study by Aylor et al. does observe a wavenumber decrease during TPD and assigns this pair of bands to $Pd^{2+}(CO)_2$ in agreement with Naccace et al., the reason for these contradictory results not being immediately obvious.[78, 82] Pd^{+} species are generally described as possessing lower CO stretching frequencies than Pd^{2+}, $Pd^{+}(CO)$ bands being assigned in the range 2110–2130 cm^{-1} while $Pd^{2+}(CO)$ bands are assigned to the range 2130–2185 cm^{-1}.[76, 82] The exception to this consensus is the work of Khivantsev et al. who describes all species in the range 2110-2185 cm^{-1} as being associated with Pd^{2+}, either in the form of $Pd^{2+}(CO)$ or $Pd^{2+}(CO)(OH)$, results that are supported by computational and other spectroscopic methods.[72, 74, 83] Given that Pd^{+} and Pd^{3+} are paramagnetic ions, analysis by EPR would be of great benefit. Unfortunately, EPR studies present in the literature are confined to zeolite materials of very low (Si/Al<10) and very high Si/Al ratios (Si/Al>20), situations in which Pd^{+} would be unlikely to exist given the high abundance of proximal Al sites and the low total abundance of Al sites respectively, though some Pd^{+} is still observed in either case.[75, 81] This limits the current understanding of the quantities of Pd^{+} present on intermediate Si/Al zeolites, these materials also presenting the strongest evidence of Pd^{+} by CO adsorption.

CO also adsorbs on metallic Pd particles, the CO adsorption behavior over metallic Pd being significantly better understood than that of the $Pd^{n+}(CO)$ bands. CO adsorption on Pd metal occurs in four distinct manners; singly adsorbed CO molecules on Pd defect sites (2095–2110 cm^{-1}), singly adsorbed CO molecules on Pd edge sites (2060–2095 cm^{-1}), doubly bridging CO of the type $(Pd^{0})_2(CO)$ (1850–1990 cm^{-1}) and finally, triply bridging $(Pd^{0})_3(CO)$ (1780–1830 cm^{-1})[74, 82, 84-86]. Previous studies on Pt-loaded zeolites have suggested a linear relationship between CO stretching frequency and metal particle size, the addition of each Pt atom being found to increase the frequency of the CO band by approximately 7 cm^{-1}, a behavior also proposed to be relevant to Pd-loaded materials.[86, 87] Of special note is the appearance of sharp $(Pd^{0})_2(CO)$ bands in the

presence of a narrow distribution of Pd particle sizes, whereas broad bands indicate a wider distribution of Pd particle sizes.[84]

The zeolite acid sites can also adsorb CO to a lesser degree, bands appearing on various H-form materials associated with CO adsorbed at Brønsted acid OH occurring at ~2175 cm^{-1}. Zeolites also have a pair of distinct Lewis acidic sites that interact with CO, bands appearing at 2195–2200 and 2225–2230 cm^{-1}. These bands are proposed to represent CO adsorbed to extra-framework alumina debris (EFAl) and partially-hydrolyzed framework Al (P-HAl) respectively.[79, 88] These bands are typically much lower in intensity than those resulting from CO adsorption at Pd.

1.2.1.2 Adsorption of Nitrogen Oxides on Pd-loaded Zeolites

The intended application of these materials also makes the IR examination of adsorbed NO_x species such as NO and NO_2 pivotally important, a wealth of such studies appearing in the literature. Both NO and NO_2 have been extensively explored as adsorbates, dating to early studies by Hadjivanov et al. and Descorme et al. in the 1990s that dealt with Cu-and Pd-loaded materials, respectively.[89, 90] Bands in the NO stretching region typically fall into three categories: bands representing NO^+ species that occur in the range 2100–2200 cm^{-1}, nitrosyl bands of the type $Pd^{n+}(NO)$ appearing in the range 1800–1900 cm^{-1}, and finally molecularly adsorbed NO_2 and nitrate bands in the range 1550–1660 cm^{-1}.[59, 90-92] There is broad agreement as to the identities of these various band groups; however, the identities of the nitrosyl bands are still debated to some degree. Early studies by Descorme et al. suggested that the two bands observed in the nitrosyl region represent $Pd^+(NO)$ and $Pd^+(NO)(NO_2/water)$ respectively, though more recent studies ascribe these species to a higher frequency feature representing $Pd^{2+}(NO)$ and a lower frequency feature representing $Pd^+(NO)$.[74, 90] A pair of bands assigned to $Pd^{n+}(NO)_2$ is also observed at higher frequencies than the respective mono-nitrosyl bands, though this species is proposed to play no role in PNA applications as it decays readily under vacuum.[74] In contrast, Mihai et al. assign bands in the 1700-1800 cm^{-1} range to dinitrosyl complexes ($Pd^{n+}(NO)_2$) according to the works of Hess et al.[91, 93] Some studies propose that NO reduces Pd^{2+} and or $[Pd^{2+}(OH)]^+$ to Pd^+ upon adsorption, while others propose that the super-electrophilic Pd^{2+} is the species that is reduced.[74, 91] The former

supposition is supported by Mihai et al. who explored the effect of Si/Al ratio on NO_x adsorption by NO-DRIFTS, showing that the band associated with Pd^{2+}(NO) is extremely weak at high Si/Al (38, 300), both materials presenting largely isolated Al sites, and thus a greater relative abundance of Pd^{+}.[91]

The behavior of NO bands in the range 2100–2200 cm^{-1} has also been extensively examined, initially being assigned to NO^{2+} by Descorme et al., but more recently being ascribed to NO^{+} that results from the reduction of Pd^{2+} to Pd^{+}, and also from interaction of NO with the zeolite Brønsted acid sites, thus explaining the appearance of these bands on H-form zeolite materials.[91, 94] These bands are also more prominent when oxygen is present, due to enhanced formation of higher nitrogen oxides under these conditions.[74, 95] However, the stability of these species varies from study to study, being found to decompose readily in the presence of water and under vacuum, while under dry inert gas these bands are stable and persist to higher temperatures.[91, 94, 95]

IR bands related to the higher nitrogen oxides are also well documented, NO_2 NO_3^{-}, N_2O_3, and an HNO_2* activated complex all being reported.[92] A number of nitrate features are often apparent upon adsorption of NO_2, this molecule being proposed to adsorb at cationic zeolite sites such as P-HAl and EFAl.[59, 92, 96] A trio of coordination modes is available to this species as evidenced by a triplet of FT-IR bands representing bridging (1600–1650 cm^{-1}), bidentate (1585–1500 cm^{-1}), and monodentate nitrates (1530–1480 cm^{-1}). These species have high thermal stability and represent a NO_x storage pathway that is less desirable for PNA materials as a result. N_2O_3 bands appear at 1950 and 1570 cm^{-1} on BEA, a result that indicates N_2O may also be stabilized by the zeolite BEA pores.[94] The NO stretch of HNO_2* has been observed at 1621 cm^{-1} on ZrO_2, this species forming in the presence of H_2 over zeolites.[92, 97]

1.2.2 Pd-loaded zeolites as passive NO_x adsorbers

The properties of zeolites as potential PNAs has been explored for various materials, but many questions remain..[59] Several factors must be considered in developing PNA materials: the total NO_x storage capacity, the utilization efficiency of precious metals (NO_x/Pd ratio), as well as the rate of NO_x uptake, a parameter that has a

heavy influence on the NO_x storage efficiency, that is, the percentage of the total NO_x that is removed from the feed.

The NO_x to precious metal ratio has been evaluated over a wide range of materials using both Pt and Pd alone and in combination as the active metal. NO_x/Pd ratios as high as 1 have been reported for materials with near total atomic dispersion of Pd, values of 0.5–0.7 being more typical.[59, 72] Unfortunately, these high ratios are only achievable to loadings of 1–2 wt%, after which the metal utilization decreases, suggesting saturation of exchange sites occurs near 1 wt.% of active metal.[59, 72] The NO_x/Pd ratio was shown by Ryou et al. to be improved after hydrothermal treatment, indicating that during preparation of the material both ion-exchanged Pd and PdO_x clusters are formed, the latter being re-distributed to ion-exchanged positions after hydrothermal treatment.[98] This and other contributions indicate high mobilities of small PdO_x and Pd metal species that can be increased by the presence of water and high temperatures, while other studies suggest the formation of pore-confined metal particles that are stabilized when they are larger than the pore openings, in a "ship in a bottle" process.[76, 84, 99, 100]

Unfortunately, PdO_x clusters do not adsorb CO or NO to any great degree, thus rendering this Pd population invisible to IR examination. These results show the importance of Pd speciation to NO_x storage and demonstrates the high sensitivity of these materials to synthesis and pretreatment conditions. The overall rate of NO_x storage over these materials has not been extensively explored, though the near-ambient temperature activity of NO_x adsorption suggests a low activation barrier and thus a process that is driven primarily by mass diffusion effects.[59] Several zeolite materials have exhibited NO_x storage efficiencies near 100 % for periods up to 60 s, such behavior being sufficient to mitigate most cold start NO_x emissions.[76, 97, 101, 102] Of further consideration is the behavior of NO_x in the presence of other automotive exhaust components, the reaction chemistry in these cases being more complex.

The NO_x desorption temperature is also a key parameter, as adsorbates that remain after exposure to the maximum catalyst temperature effectively act as catalyst poisons. The observed behavior is found to substantially depend on the ramp rate employed during TPD studies, though a rate of 10 °C/min is most common and allows

adequate differentiation of adsorbates for kinetic evaluation.[59] However, such a slow ramp rate is unrealistic under real application due to the rapid temperature changes that occur during a cold start, further investigation revealing a non-linear relationship between ramp rate and desorption temperature, though above rates of ~100 °C/min the changes in desorption temperature are less pronounced.[102-104] Generally, either one or two desorption events are observed, one at lower temperatures (100–250 °C) and another at higher temperatures (200–500 °C).[59] Desorption temperatures vary widely depending on the zeolite framework, metal dispersion, and presence of other exhaust species, though generally any desorption below 200 °C is undesirable, as this will lead to incomplete NO_x reduction on the downstream catalyst.[24]

The NO_x desorption behavior is heavily influenced by the speciation of adsorbed NO_x, six distinct adsorption pathways being identified in the literature by Gu et al. that lead to three distinct groups of adsorbates.[59] The species that exhibit the lowest temperature desorption are NO^+ and NO_2^+ weakly interacting with zeolite acid sites, these species comprising much of the NO_x that desorbs below optimal temperatures.[105] Nitrosyl species are found to comprise NO_x that desorbs near and somewhat above the optimum temperature, though the desorption range of these species is again heavily dependent on the preparation and pretreatment conditions, as well as the presence of other exhaust species.[74, 83, 91] Finally, species related to NO_2 adsorbed as nitrates desorb at intermediate to high temperatures (300–500 °C), these species representing a less desirable adsorption pathway due to the potential failure of these species to completely desorb.[106]

1.2.2.1 Effect of Reductants

The effects of CO on PNA materials have been thoroughly explored during all parts of the PNA process on a variety of zeolite frameworks. The presence of CO during high-temperature pretreatment has been found to be especially problematic for the long-term activity of these materials, CO being found to lead to greater Pd^0 particle mobility and agglomeration with concurrent loss of PNA activity.[36, 103, 107] The agglomeration of large Pd^0 particles outside the zeolite framework is proposed to be responsible for the loss of PNA activity, these particles failing to re-disperse to ion-exchanged Pd upon oxidative

regeneration.[5, 100, 107, 108] During low-temperature adsorption of NO_x, CO is found to have a promotional effect on PNA behavior both through increased NO_x storage capacity and elevation of NO_x desorption temperature.[76, 103] These results were initially proposed to be a result of the reduction of Pd to lower oxidation state, i.e. Pd^+, that binds NO more strongly. Other studies have suggested that this promotional effect results from the formation of a Pd^{2+}(NO)(CO) co-adsorbed complex that allows for greater quantities of NO_x to adsorb while also representing a more thermally stable species than NO adsorbed alone.[83] Other pathways have also been proposed, including the formation of an NCO species like that observed on ceria supported metals, though this band occurs in a similar range to the CO stretch of the reported co-adsorbed complex and thus differentiation between these two species is difficult.[97]

The effect of H_2 on Pd-loaded zeolites is more benign, reduction at high temperatures in H_2 demonstrated to be more reversible due to the formation of smaller Pd particles that are more readily re-dispersed to exchanged Pd ions.[100, 108] Theis et al. found H_2 to promote NO_x adsorption capacity, and suggested the formation of HNO_2* species, hydrocarbons having a similar effect.[97] The reaction of hydrocarbons over Pd-loaded zeolite materials is more complex, with the participation of water gas shift and steam reforming reactions being significant.[40, 41] The presence of hydrocarbons at high temperature leads primarily to combustion under lean conditions, though ethylene was shown to promote N_2O formation at high temperatures on Pd-loaded ceria/zirconia through an unselective NO_x reduction pathway.[58] The formation of alkyl nitrites is also proposed to promote NO_x adsorption on ceria-based materials, though these last reactions are not in evidence for zeolite-based materials.[58, 97]

1.2.2.2 Effect of Oxidants

Oxidizing agents typically consist of O_2 and NO_2, the presence of these species exerting influence in all aspects of PNA reactivity. The presence of O_2 in the gas feed leads to enhanced oxidation of NO to NO_2, thus many of these effects are also interrelated. This oxidation pathway is found to enhance NO_x storage capacity through the formation of nitrates at EFAl sites in addition to the formation of NO^+ and NO_2^+, these reactions being active even at near-ambient temperatures.[76, 90, 95] However, NO

oxidation competes with the process of NO_x adsorption and desorption, though the specifics of this relationship are still poorly understood.[59] Oxidation of NO to NO_2 is observed both during and after NO_x storage and is proposed to occur through three mechanisms:

$$Z^- - Pd^{2+} - OH + NO \rightarrow NO_2 + H_2O + Z^- - Pd^+ \quad (5)$$ [90]

$$Z^- - Pd^{2+} - O - Pd^{2+} - Z^- + NO \rightarrow NO_2 + 2[Z^- - Pd^+] \quad (6)$$ [76, 109]

$$PdO_2 + 2NO \rightarrow NO_2 + NO - PdO \quad (7)$$ [76, 109]

In each case Pd is reduced during NO_2 formation, thus indicating that the role of Pd^+ species is significant, as NO is proposed to adsorb at the reduced Pd sites. The presence of lower oxidation state Pd after NO_x adsorption was confirmed by FT-IR and XPS spectroscopy performed by Zheng et al. but again, quantitative analysis of these species is challenging.[76] Furthermore, direct storage of NO at Pd^{2+} is proposed in many cases, and as a result the ratio of NO removed from the feed to NO_2 formed cannot readily be differentiated, preventing deconvolution of adsorption and oxidation activity.[59] An additional complication to understanding these processes is the weak interaction between NO_x and the zeolite Brønsted acid sites that results in formation of NO^+ and NO_2^+ even in the absence of active metals.[82] The oxidizing effects of NO_2 on ionic Pd species has not been well characterized by FT-IR experiments, though an equimolar quantity of NO and NO_2 has been shown to enhance the activity of Cu-zeolite SCR catalysts and other results on Pd zeolites suggest this is the case for these materials as well.[76, 110]

1.2.2.3 Effect of Water

Water has been shown to influence various aspects of PNA behavior. Treatment of these materials in the presence of water at high temperatures is referred to as hydrothermal aging, this process being shown to impact both the zeolite and the exchanged metal. Several studies have explored the hydrothermal stability of assorted zeolite frameworks under relevant conditions, in addition to Pd on ceria/zirconia and

SCR catalysts.[19, 70, 73, 98] Dealumination of the zeolite is an important deactivation pathway for these materials and is facilitated by water. Elimination of Al sites from the framework has been shown to lead to metal particle agglomeration and loss of zeolite NO_x storage sites.[100, 111] Generally, smaller pore zeolite frameworks are more resilient to dealumination by hydrolysis due to the smaller volume available for the reaction to take place, though the hydrophobicity of the framework is also important for the lability of the Al species involved in this reaction.[94] The Si/Al ratio is also important to the dealumination process, as lower Si/Al ratio materials simply have more sites at which this process can occur and are more hydrophilic in nature. Hydrothermal aging has also been shown to facilitate Pd migration in small pore zeolites such as SSZ-13, initial Pd deposition leading to the formation of PdO_x particles due to diffusion limitations within the zeolite framework.[98, 111] These PdO_x particles are redispersed into ion-exchange sites upon hydrothermal aging, as demonstrated by the appearance of a new NO_x desorption feature and through H_2 TPR of the treated and untreated materials. The effect of water on Pd speciation is less thoroughly understood, though the formation of hydrated Pd^{n+} complexes is proposed to decrease NO_x storage.[59, 102]

Water also has an impact on the NO_x adsorption behavior, as water interacts strongly with the zeolite framework at near-ambient temperatures and thus competes for adsorption sites during the initial seconds of PNA operation.[76] This result is a discouraging one for the implementation of these materials as water has been demonstrated to dramatically suppress NO_x adsorption at 100 °C and below.[76, 112] This has been proposed to be a result of either the inhibition of NO oxidation, or of the blocking of zeolite Brønsted acid sties.[102, 112] However, the inhibitive effects of water have been shown to be tempered somewhat by the presence of other exhaust components such as CO and H_2 at low temperatures.[76, 103] The presence of ethylene was found to inhibit NO_x storage to a greater degree than water alone on Pd ceria/zirconia materials, while CO and H_2 as reductants failed to produce a similar result.[113] These results are explained by the influence of water on three disparate reactive intermediates, including alkyl nitrates and nitrites, NCO, and finally HNO_2*. These intermediates are shown to be produced by ethylene, CO, and H_2 respectively, though these species have not been observed on zeolite-based materials.[113]

1.3 Dissertation Aims and Scope

From the preceding discussion, several key areas of investigation become apparent. First and foremost, the identification of FT-IR bands through careful experimental observation is clearly indicated in the absence of adequately corroborating techniques. To achieve this goal, a wide variety of adsorbates and pretreatment conditions must be employed over a consistent set of materials to provide a more complete picture of the effects of individual gas species present in the automotive exhaust stream. The next chapter of this thesis revolves around the Pd speciation present on the two zeolite frameworks chosen for this study, Pd-BEA and Pd-CHA. Pd-BEA was prepared at various Pd loadings to better understand the thermodynamic favorability of Pd species, while also providing much needed information for Pd^{n+}(CO) band identification. Both of these materials are of intermediate Si/Al ratio (12–15) and as a result are representative of the most complex Pd^{n+}(CO) band structure as observed by Zheng et al.[76] A further advantage of comparing materials of similar Si/Al is the more facile deconvolution of framework-related effects from other processes, these two frameworks possessing widely different pore size and framework structure complexity. The effects of water on these materials will also be examined at both high and near-ambient temperatures.

The next chapter will explore the effects of oxidizing and reducing pretreatment conditions on the Pd speciation of these materials. The effect of reductants such as H_2 and CO on Pd speciation will be examined to gain better understanding of the deactivation modes of these materials. Next, the role of zeolite sites in PNA activity will be more fully explored through examination of the H-form zeolite materials in comparison to their Pd-loaded counterparts to derive better understanding of the FT-IR bands resulting from adsorption of NO_x and the zeolite sites responsible for the formation of these species. The role of partially hydrolyzed Al sites on zeolite BEA in NO_x storage is examined, as well as their potential interaction with Pd, a special focus being placed on deconvolution of the behavior of NO and NO_2.[88] Finally, the effects of NO and NO_2 on these materials will be examined during and after pretreatment, as well as the adsorption and desorption behavior from these materials pretreated in other reducing and oxidizing environments.

CHAPTER 2. EFFECT OF Pd LOADING AND WATER ON Pd-SPECIATION

2.1 Introduction

This chapter will focus on a basic description of the zeolite materials used in this work, as well as initial experiments undertaken to derive FT-IR band assignments. The resulting CO band assignments will be presented for both BEA and CHA. The effects of Pd-loading on BEA will also be described, these data providing evidence on the preference of Pd for certain exchange sites. Finally, an examination of the effects of water on these materials will be performed, the effects of water examined both during pretreatment and during CO adsorption. The catalyst materials and data presented in Table 2.1 were contributed by Mr. Trevor Lardinois at Purdue University, while XPS spectra were collected by Dr. Olivier Heintz at the University of Burgundy, France.

2.2 Effect of Pd-loading on Pd-BEA

2.2.1 Catalyst Characterization

The catalyst materials were prepared as described in Appendix 2 and characterized by a combination of techniques. The BEA zeolite was obtained commercially, while the CHA zeolite was synthesized at Purdue University according to the methods of Di Iorio et al.[114, 115] Zeolites were initially prepared in Na^+ form, Pd being added by incipient wetness impregnation, followed by drying and calcination at 550 °C. For each material, the Si/Al, Pd wt%, extent of Pd exchange, and crystallinity were evaluated. In total, seven materials were examined in this work, H-CHA and H-BEA, in addition to 0.1, 0.6, and 1.4 wt% Pd-BEA and 0.6 wt% Pd-CHA. Lastly, a 1 wt% Pd-Si-BEA material was prepared, a sample in which no Al is incorporated into the BEA framework, providing an example of a material in which all Pd is present as PdO_x particles. In each case, atomic absorption spectroscopy was used to determine the Si/Al and the Pd wt%, XRD was used to examine the crystallinity of the materials and finally, H_2-TPR was employed to assess the extent of Pd exchange. The results of these analyses

are presented in Table 2.1, while the experimental data used to determine these values are presented in Appendix 2.

Table 2.1 Characterization of air-treated (550 °C) Pd-zeolite materials

Sample	Si/Al*	Pd wt %*	Pd/Al*	Pd_{iso}/Pd_{tot}+
1% Pd-Si-BEA	∞	0.96	--	0.00
0.1% Pd-BEA	12.5	0.13	0.009	0.67
0.6% Pd-BEA	12.5	0.60	0.04	0.78
1.4% Pd-BEA	12.5	1.36	0.09	0.75
0.7% Pd-CHA	14	0.68	0.06	0.30

*Determined by atomic absorption spectroscopy +Determined by H_2 TPR

The Si/Al ratio of the materials is intentionally similar, to limit the effect of this parameter on the Pd speciation and PNA behavior. The Pd_{iso}/Pd_{tot} is an especially important parameter, as this is an indication of the extent to which Pd is ion-exchanged rather than present as PdO_x particles. This determination was made possible by the differing reduction temperatures of exchanged Pd cations and PdO_x particles, the former exhibiting a reduction event at 35–200 °C and the latter reducing at -10–35 °C. The quantity of ion-exchanged Pd was then estimated assuming a 1:1 stoichiometric ratio of H_2 to Pd^{2+} ions, as determined by a calibrated TCD signal. This also assumes the majority of Pd cations are divalent after pretreatment in air, an assumption shown to be valid by DRIFTS results presented in the next section. H_2 consumption was also observed at –40 °C on both the H- and Pd-form materials, this being a result of Ar desorption from the zeolite micropores during TPR rather than a true reduction event.[116]

The high degree of Pd ion-exchange on the BEA materials is notable, showing that ion-exchanged Pd represents greater than two-thirds of Pd present. Meanwhile, for the 0.7% Pd-CHA material only about 30% of Pd was found to be present in an ion-exchanged state, while the remainder is present as PdO_x and Pd^0 particles. This result is consistent with other reports on CHA and SSZ-13 frameworks, the extent of Pd dispersion being limited by the rate of diffusion through the small pores of these materials.[100] The framework structure of each material was found to be consistent with XRD analyses published elsewhere, thus confirming the framework structures remained intact through Pd impregnation and calcination.[117, 118] The pore size of the two

frameworks is substantially different, CHA having a pore diameter of 3.7 × 3.7 Å, while BEA, a partially disordered material, has both straight and sinusoidal channels with diameters of 6.6 × 6.7 Å and 5.6 × 5.6 Å, respectively. The framework complexity of these materials is also substantially different, CHA consisting of 8-, 6-, and 4-membered rings and a single T site, while BEA is constituted of 4-, 5-, 6-, and 12-membered rings with 9 distinct T sites.[77]

2.2.2 CO-DRIFTS

To examine the Pd speciation, each of the BEA materials was pretreated in air or Ar for 1 h at 500 °C to remove water from the zeolite prior to adsorption. CO was then adsorbed at room temperature and a concentration of 1000 ppm in Ar on each of the BEA materials for ten minutes, as shown in Figure 2.1. The band assignments and associated references are shown in Table 2.2.

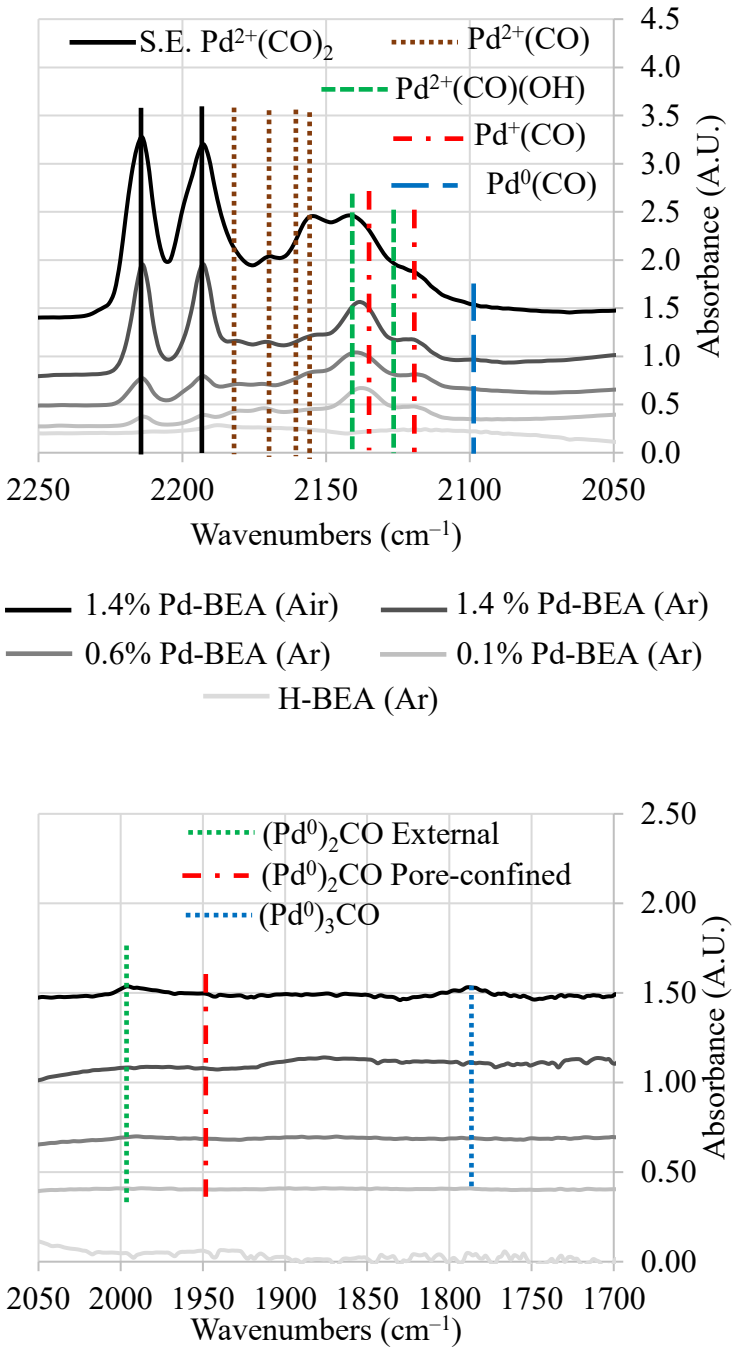

Figure 2.1 DRIFT spectra of CO adsorbed on Pd-BEA pretreated at 500 °C for 1 h with air or Ar rigorously dried by cold trap. To visualize Pd speciation, 1000 ppm CO in Ar was adsorbed for 10 min at 25 °C. Top: ionic Pd range. Bottom: metallic Pd range.

Table 2.2 Pd(CO) DRIFTS band assignments and references for BEA materials

Band (cm^{-1})	Assignment	Position	References
1790	$(Pd^0)_3(CO)$	External Pd^0	82, 119
1950	$(Pd^0)_2(CO)$	Pore-confined Pd^0	82, 119
1990	$(Pd^0)_2(CO)$	External Pd^0	82, 119
2078	$Pd^0(CO)$	Pd^0 defect	82, 119
2098	$Pd^0(CO)$	Pd^0 defect	82, 119
2113	$Pd^+(CO)$	Isolated Al	75, 76, 78, 82, 102
2125	$Pd^{2+}(CO)(OH)$	Isolated Al	78, 102
2132	$Pd^+(CO)$	Isolated Al	78, 102
2144	$Pd^{2+}(CO)(OH)$	Isolated Al	75, 76, 78, 102
2154	$Pd^{2+}(CO)$	Paired Al	82, 102
2160	$Pd^{2+}(CO)$	Paired Al	82, 102
2169	$Pd^{2+}(CO)$	Paired Al	82, 102
2183	$Pd^{2+}(CO)$	Paired Al	82, 102
2189	Super-electrophilic $Pd^{2+}(CO)_2$	Pore-confined ion	74, 80
2212	Super-electrophilic $Pd^{2+}(CO)_2$	Pore-confined ion	74, 80

These spectra were collected under rigorously dry conditions, a cold trap being used to remove residual water from the pretreatment gas. As expected, CO adsorption on the H-BEA material is weak, the only obvious feature being a CO stretch related to CO adsorbed at Lewis acid sites at 2185 cm^{-1}. A pair of much weaker and broader features is also observed in the ranges 2075–2140 and 2140–2180 cm^{-1}, these representing CO condensed in the zeolite pores and CO adsorbed at Brønsted acid sites, respectively.[88, 120] The 0.1 wt% Pd material shows the presence of the various $Pd^{n+}(CO)_x$ bands, all bands observed on the more highly Pd-loaded materials being in evidence. This suggests the thermodynamic stability of the various Pd species is not highly differentiated, though the most intense bands occur at frequencies typically associated with $Pd^{+}(CO)$ (2119 and 2134 cm^{-1}), indicating a slight preference for the filling of isolated Al sites at low Pd loading.[76] The high-frequency $Pd^{n+}(CO)$ bands (>2150 cm^{-1}) can be identified as $Pd^{2+}(CO)$ species (2154, 2160, 2169, and 2183 cm^{-1}) and the symmetric and asymmetric stretches of super-electrophilic $Pd^{2+}(CO)_2$ species (2189, 2212 cm^{-1}). The literature broadly agrees on the assignment of these bands as CO adsorbed at divalent Pd cations, though the true nature of the super-electrophilic complex was only recently described by Khivantsev et al.[74, 76] The abundance of $Pd^{2+}(CO)$ bands is indicative of the BEA framework complexity, five electronically distinct Pd^{2+} species being observed. Under these rigorously dry conditions, only very weak metallic $Pd^{0}(CO)$ bands are observed at frequencies consistent with bulk Pd particles, suggesting that only limited auto-reduction to Pd^{0} occurred during inert treatment.[82]

On the 0.6 wt% Pd material, $Pd^{+}(CO)$ bands are again the most intense, though the frequency of the band at 2134 cm^{-1} increases to 2136 cm^{-1}, an observation that suggests the presence of multiple $Pd^{n+}(CO)$ species of similar CO frequency, the increase or decrease in abundance of one species leading to a shift of the local band maximum. This band occurs in an area of overlap between $Pd^{+}(CO)$ and $Pd^{2+}(CO)$ bands, and thus the assignment of this species is ambiguous, based on the available literature.[74, 76, 82] The Ar-pretreated 1.4% Pd material continues this trend, the band appearing at 2140 cm^{-1}, though at this point $Pd^{2+}(CO)$ bands become dominant in intensity. The frequency increase of this band occurs simultaneously with the increasing abundance of Pd^{2+}, the first indication that the high-frequency contributor to this band represents a divalent Pd cation.

The air-pretreated 1.4% Pd-BEA further reinforces this conclusion, as this band shifts again to 2144 cm^{-1} with the concurrent appearance of a shoulder to the $Pd^{+}(CO)$ band (2119 cm^{-1}) at a frequency of approximately 2125 cm^{-1}. The air-pretreated 1.4% Pd-BEA shows a predominance of $Pd^{2+}(CO)$ species and points to the conclusion that most Pd is present as Pd^{2+} in this state, thus demonstrating the validity of the 1:1 H_2 to Pd stoichiometry used in H_2-TPR calculations. These results reveal a complex $Pd^{n+}(CO)$ band structure in the range 2110–2145 cm^{-1}, at least four distinct Pd species exhibiting CO bands in this range.

An EPR study of Pd-BEA zeolite carried out by Stokes et al. revealed that more than one $Pd^{+}(CO)$ complex is formed during CO adsorption, due to a heterogeneity of EPR signals upon exposure of Pd-BEA to CO, though the CO coordination number per Pd was not determined and Pd^{+} was not quantified.[75] EPR studies have been conducted on other Pd-loaded zeolites, establishing the presence of Pd^{+} species on a variety of frameworks, though none of these studies provide an example of an intermediate Si/Al material, and thus the quantities of Pd^{+} observed are always low.[75, 78, 81] Taking these studies into account, it can be inferred that some of the $Pd^{n+}(CO)$ bands observed in the region 2110–2145 cm^{-1} represent $Pd^{+}(CO)$ bands, while the others likely represent additional divalent Pd species.

More information can be gleaned from the TPD of CO from air-pretreated 1.4% Pd-BEA as shown in Figure 2.2, spectra being recorded every 100 °C. As the temperature is increased from 25 °C to 100 °C, the bands in the range 2110–2145 cm^{-1} become readily distinguishable into four features at 2144, 2132, 2125, and 2119 cm^{-1}, though this last band is only evident as a weak shoulder to the band at 2125 cm^{-1}. A pair of bands also appears in the metallic $Pd^{0}(CO)$ frequency range at 100 °C (2078, 2098 cm^{-1}), these representing CO at Pd^{0} particle defect sites. By 200 °C nearly all the CO has desorbed, but a pair of bands remains at 2132 and 2113 cm^{-1}, these disappearing by 300 °C. The shifting of bands to lower frequency upon TPD has been observed previously and has been explained either as an effect of decreasing CO coverage, or as a more thermally stable $Pd^{n+}(CO)_2$ species.[78, 82] However, neither of these explanations withstands scrutiny; CO coverage effects are only described over metal particles and a polycarbonyl species

would be expected to occur at higher wavenumber, the opposite direction of the observed behavior. Further, Zheng et al. do not observe this behavior on any of the Pd-loaded frameworks examined in their study.[76] The appearance of Pd^0(CO) bands with increasing temperature provides a valuable clue however, as this is indicative of Pd reduction by CO. Since Pd^+(CO) bands are generally agreed to be at lower frequency than Pd^{2+}(CO) bands, the observed decrease in band frequency can therefore be interpreted as the reduction of Pd^{2+} ions to Pd^+ with the simultaneous appearance of Pd metal particles that likely results from further reduction of Pd^+. Due to the entangled effects of Pd reduction and CO desorption, the extent to which the high-frequency Pd^{2+} features are reduced in this process cannot be readily discerned, though the frequencies of these bands remain relatively unaffected during desorption.

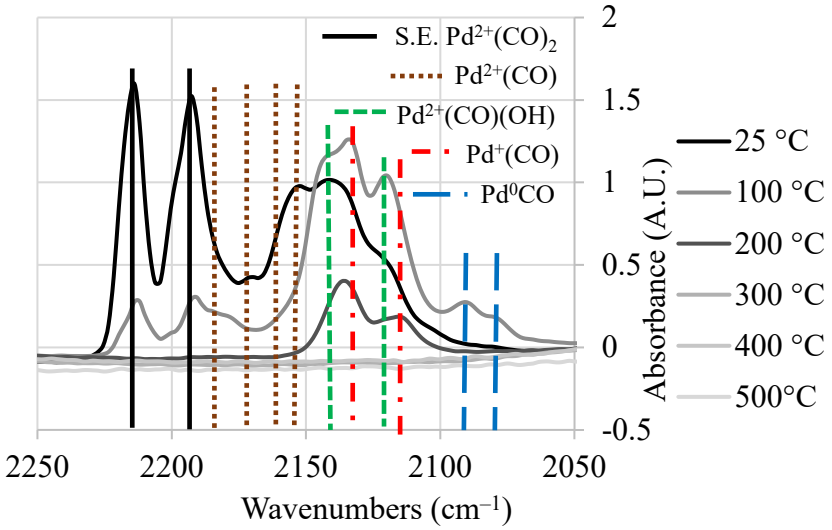

Figure 2.2 1.4% Pd-BEA: DRIFT spectra of CO desorption after pretreatment at 500 °C for 1 h with air which has been rigorously dried by cold trap. CO was adsorbed for 10 minutes at 25 °C before the catalyst was purged for 10 minutes in Ar prior to ramping to remove gas-phase CO. Temperature was ramped at 10 °C/min to 500 °C with spectra being collected every 100 °C.

These observations suggest the presence of three distinct populations of Pd^{2+} ions, the super-electrophilic Pd^{2+} ions, a group of Pd^{2+} ions exchanged at the zeolite framework of intermediate electrophilicity, and finally a group of easily reducible Pd^{2+} species that have electrophilic character similar to that of Pd^+. The CO stretching frequencies of these

bands can be used as a relative measure of the metal electrophilicity due to the effects of π-backbonding, in which electron density is transferred from the filled metal d-orbitals to the empty antibonding orbital (LUMO) of CO, thus lengthening the CO bond and altering its stretching frequency. These observations point to the possibility of a Pd^{2+} species that is already ligated by another species, $[Pd^{2+}(OH)]^{+}$ being proposed to also present CO bands in this region.[74, 94] Examination of the OH region of the FT-IR spectra would theoretically reveal the presence of a Pd(OH) stretch, though zeolite OH bands also occur in this region and exert convoluting effects during CO adsorption. To facilitate observation of changes in the zeolite OH region relative to the H-form material, the spectrum of the H-form material was employed as the background spectrum for the dehydrated Pd-loaded materials such that any bands that rise above the baseline would indicate the development of additional OH species relative to the H-form zeolite. The results of this analysis are presented in Figure 2.3.

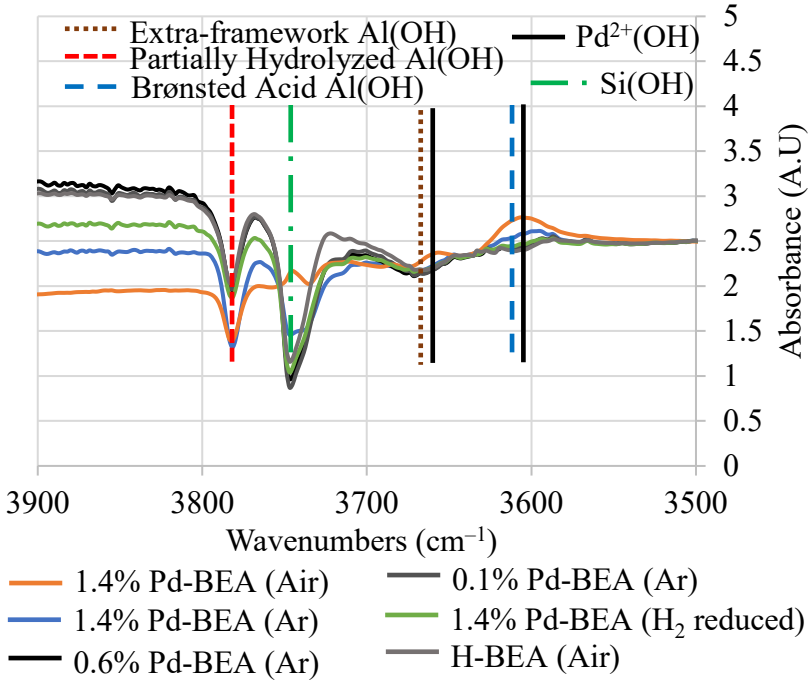

Figure 2.3 BEA: DRIFT spectra of the OH region of the dehydrated 1.4%, 0.6%, 0.1% Pd-BEA and H-BEA materials after pretreatment at 500 °C for 1 h with Ar rigorously dried by cold trap. The spectrum of H-BEA was used as the background for these spectra. Materials were cooled in dried Ar to 25 °C prior to collection. Spectra of H-BEA pretreated in air at 500 °C and 1.4% Pd-BEA treated in H_2 at 500 °C are also shown.

Zeolite-exchanged transition metal OH bands are not well documented in the literature, though recent identification of a Cu(OH) band on Cu-SSZ-13 at 3660 cm^{-1} provides some indication of where such species may occur.[121] In fact, examination of the variously loaded Pd-BEA materials shows increasing intensity of a pair of OH bands at 3604 and 3660 cm^{-1} with increasing Pd loading, reaching maximum intensity on the air-treated 1.4% Pd-BEA material. These bands mirror the behavior of the bands at 2144 and 2125 cm^{-1}, providing evidence that these CO bands represent the CO stretch of a Pd^{2+}(OH)(CO) complex, this species readily reducing to Pd^{+}(CO) at elevated temperature.

To further confirm the identity of the OH bands, the spectra of the air pretreated H-BEA material and the H_2-reduced 1.4% Pd-BEA material are also included. The putative Pd(OH) bands overlap both zeolite Brønsted acid and EFAl(OH) bands though the air-

treated H-BEA shows no analogous intensity increase in these areas, discounting the possibility that these bands result from changes in the zeolite OH distribution during pretreatment. Further, the H_2-reduced 1.4% Pd-BEA also fails to show these bands, thereby confirming their association with ion-exchanged Pd. The CO band assignments presented above provide a consistent explanation of the available literature results, the frequency shift observed upon TPD by Naccace et al. and Aylor et al. being explained by reduction of $[Pd^{2+}(OH)]^+$ to Pd^+, while the failure of Zheng et al. to observe this behavior can be explained by the absence of $[Pd^{2+}(OH)]^+$, the $Pd^{n+}(CO)$ bands observed in that case resulting from "bare" Pd^{n+} ions in agreement with the conclusions of the authors.[76, 78, 82] These differences in speciation can be explained by the dependence of this parameter on the preparation methods employed in each case.

CO adsorption was also carried out on the 1% Pd-Si-BEA material to characterize the interaction of CO with PdO_x particles, shown in Figure 2.4. No sharp Pd(CO) bands appear, only the pair of broad features previously described on H-BEA that represent CO condensed in the zeolite pores and CO interaction with zeolite OH sites.

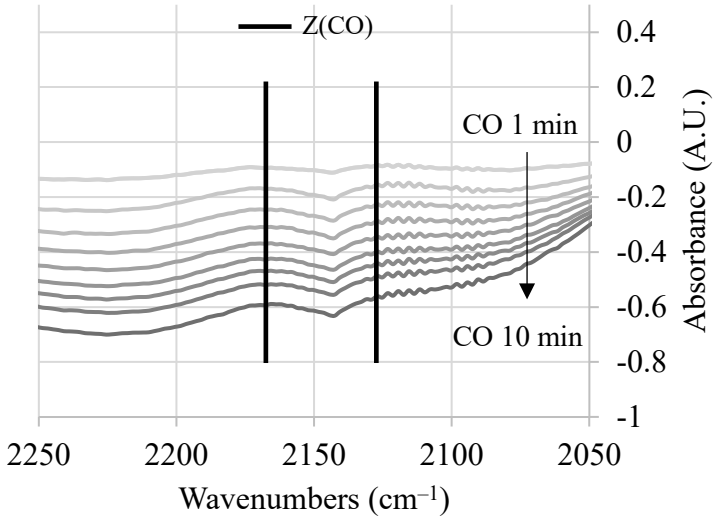

Figure 2.4 1% Pd-Si-BEA: DRIFT spectra of CO adsorption after pretreatment at 500 °C for 1 h with Ar which has been rigorously dried by cold trap. CO was adsorbed for 10 minutes at 25 °C.

To summarize, Pd^{+} and Pd^{2+} of intermediate electrophilicity fill the zeolite first (presumably at isolated and paired Al sites, respectively), followed by an increasing abundance of super-electrophilic Pd^{2+} with increasing Pd loading. Finally, oxidation of Pd^{+} to the least electrophilic Pd^{2+} ions (2154 cm^{-1}) and $[Pd^{2+}(OH)]^{+}$ at isolated Al sites is observed under air treatment. The band at 2154 cm^{-1} is likely representative of Pd^{2+} at NNN Al sites, this species possessing greater stability than its higher frequency counterparts (that would represent NNNN Al sites) as described in section 2.4. Meanwhile, isolated Al sites support Pd^{+} ions under inert pretreatment, these species being largely converted to $[Pd^{2+}(OH)]^{+}$ upon oxidizing treatment. The high intensity of the super-electrophilic $Pd^{2+}(CO)_2$ bands is also notable, these bands being much weaker on BEA zeolites shown in the literature, while these species are shown to predominate on Pd-SSZ-13 of low Si/Al.[74, 76] Of further note is the near-total absence of metallic Pd(CO) bands under rigorously dry conditions, an observation to be discussed extensively in section 2.3.

2.3 Comparison to Pd-CHA

The 0.7% Pd-CHA material was treated in Ar and compared to 1.4% Pd-BEA as shown in Figure 2.5, a listing of band assignments being presented in Table 2.3. Even though 0.7% Pd-CHA presents a much lower degree of Pd ion exchange, the Pd(CO) bands are much more intense than those observed on 1.4% Pd-BEA. This suggests either that the extinction coefficients of these bands differ substantially from framework to framework, or the lower abundance of differing sites leads to more intense bands on CHA. Using the band assignments for Pd-BEA and the similarity of CO band structure between the two materials, a set of assignments can be derived for 0.7% Pd-CHA. Again, the super-electrophilic Pd^{2+} bands are intense, though the symmetric/asymmetric stretch ratio differs from that observed on Pd-BEA. This, coupled with a slight shift of these bands to lower frequency, suggests the smaller CHA pore is imposing geometric constraints on this species that increase the extent of π back-bonding with CO. The number of putative NNNN and NNN Al-sited Pd^{2+} bands is lower than that observed on BEA, only a pair of bands being observed at 2175 and 2154 cm^{-1} in this region. This is

reflective of the less complex CHA framework, a narrower distribution of these sites being available for exchange.

The low-frequency region of the 0.7% Pd-CHA spectrum also presents an intriguing feature. A very sharp band appears at 1890 cm^{-1} representing $(Pd^0)_2(CO)$ adsorbed on a group of Pd metal particles with a very narrow particle size range.[119] This band likely represents CO adsorbed at Pd metal particles trapped within the zeolite framework that consist of a very few Pd atoms as described by Sheu et al.[84] The appearance of such a species on CHA is again a result of the smaller CHA pore size, BEA apparently having less propensity to form such species.

Table 2.3 Pd(CO) DRIFTS band assignments and references for CHA materials

Band (cm^{-1})	Assignment	Position	References
1790	$(Pd^0)_3(CO)$	External Pd^0	[27, 28]
1890-1920	$(Pd^0)_2(CO)$	Pore-confined Pd^0	[27, 28]
1990	$(Pd^0)_2(CO)$	External Pd^0	[27, 28]
2113	$Pd^+(CO)$	Isolated Al	[3, 16, 20, 27, 29]
2125	$Pd^{2+}(CO)(OH)$	Isolated Al	[3, 20]
2132	$Pd^+(CO)$	Isolated Al	[3, 20]
2142	$Pd^{2+}(CO)(OH)$	Isolated Al	[3, 16, 20, 29]
2154	$Pd^{2+}(CO)$	Paired Al	[3, 16]
2175	$Pd^{2+}(CO)$	Paired Al	[3, 16]
2188	Super-electrophilic $Pd^{2+}(CO)_2$	Pore-confined ion	[17, 30]
2212	Super-electrophilic $Pd^{2+}(CO)_2$	Pore-confined ion	[17, 30]

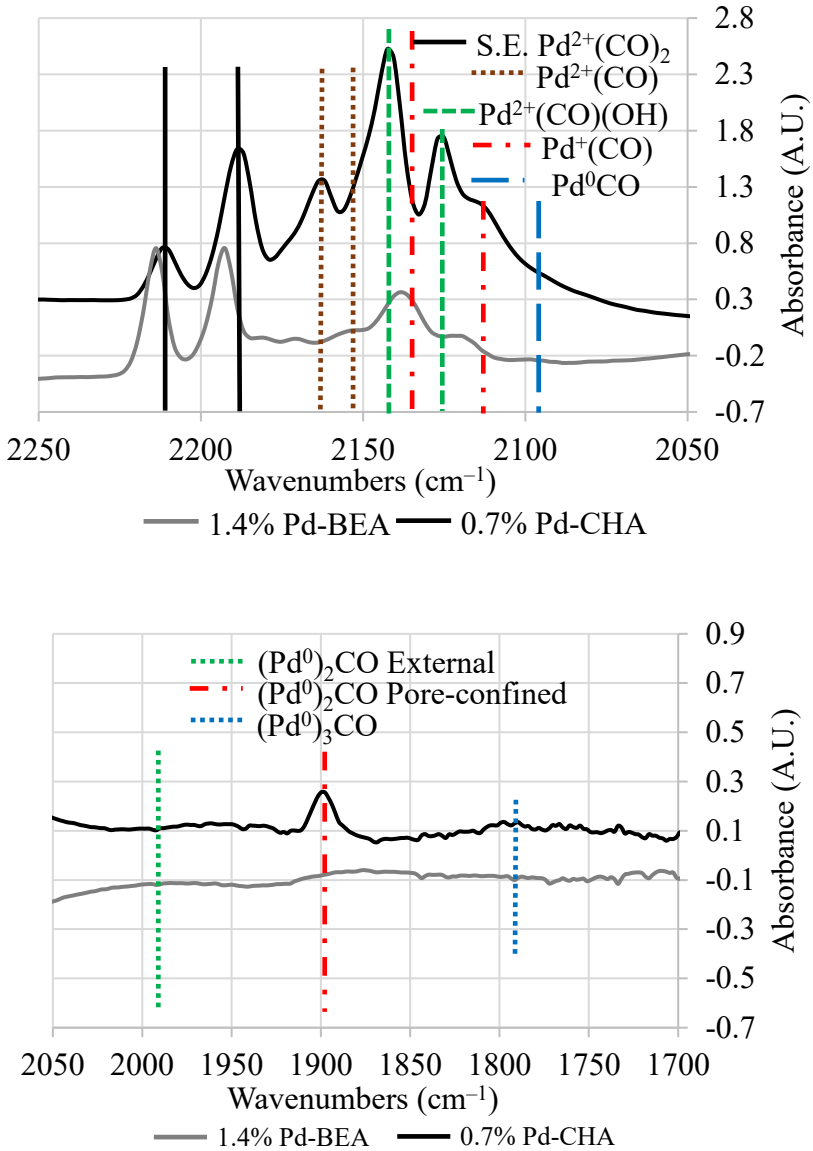

Figure 2.5 DRIFT spectra of CO adsorbed on 0.7% Pd-CHA and 1.4% Pd-BEA pretreated at 500 °C for 1 h with Ar rigorously dried by cold trap. To visualize Pd speciation, 1000 ppm CO in Ar was adsorbed for 10 min at 25°C. Top: Ionic Pd range. Bottom: metallic Pd range.

Pd^{2+}-(OH)(CO) bands are also observed in conjunction with Pd^{+}(CO) bands, these occurring at frequencies nearly identical to those observed on Pd-BEA. The desorption behavior of 0.7% Pd-CHA was also analyzed, shown in Figure 2.6. Again, four distinct Pd^{n+}(CO) species appear in the range 2110–2145 cm^{-1}, bands at 2113, 2125, 2132, and 2142 cm^{-1} being observed at a temperature of 120 °C, the band maxima again shifting to lower frequency with increasing temperature. This behavior indicates a similar CO band

structure to that observed on 1.4% Pd-BEA, so the OH region of the CHA zeolite was also examined to determine the presence of any Pd(OH) bands. Shown in Figure 2.7, these data do not reveal the obvious presence of any Pd(OH) bands due to the greater intensity of the overlapping zeolite OH bands on the CHA materials, though this does not preclude the existence of $[Pd^{2+}(OH)]^{+}$.

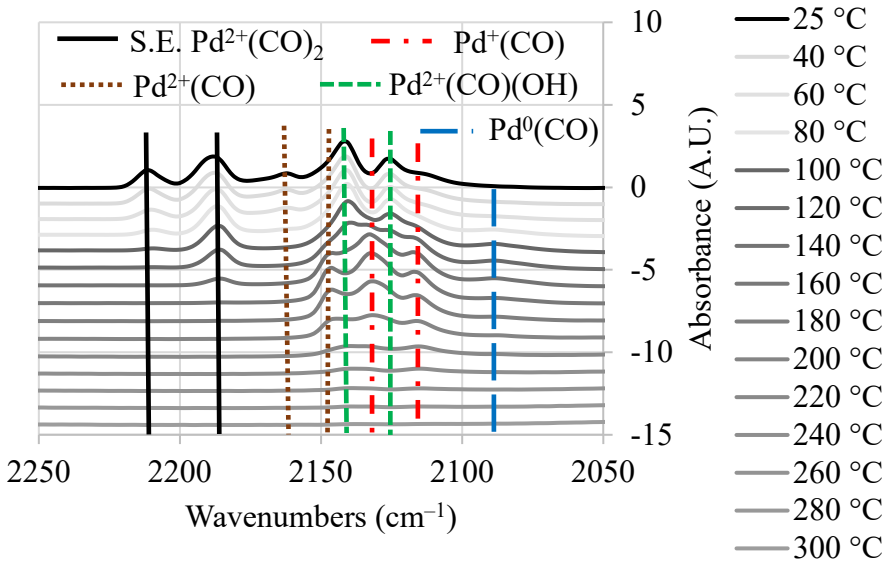

Figure 2.6 0.7% Pd-CHA: DRIFT spectra of CO desorption after pretreatment at 500 °C for 1 h with rigorously dried Ar. CO was adsorbed for 10 minutes at 25 °C before the material was purged for 10 minutes in Ar prior to ramping to remove gas phase CO. Temperature was ramped at 10 °C/min to 500 °C with spectra being collected every 20 °C.

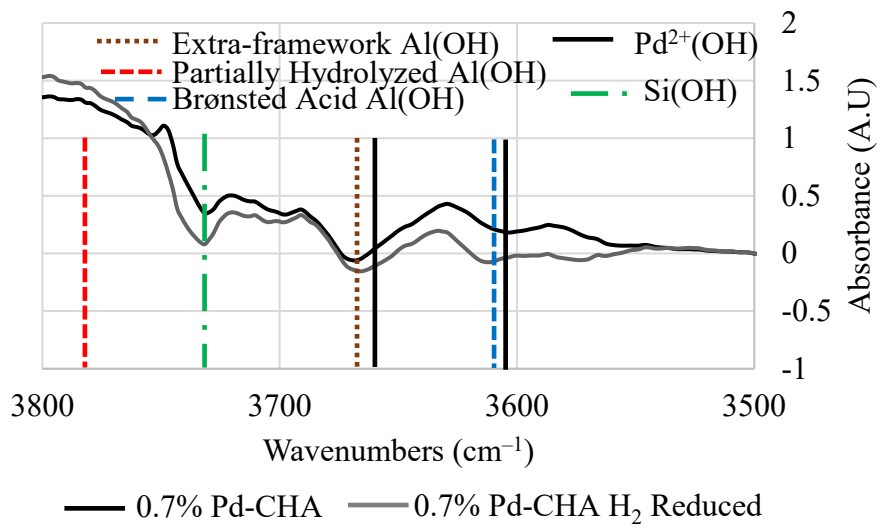

Figure 2.7 DRIFT spectra of the OH region of the dehydrated 0.7% Pd-CHA materials after pretreatment at 500 °C for 1 h with Ar rigorously dried by cold trap. The spectrum of H-CHA was used as the background for these spectra. Materials were cooled in dried Ar to 25 °C prior to collection. The spectrum of 0.7% Pd-CHA treated in H_2 at 500 °C are also shown.

2.4 Effect of Water During Pretreatment

As described above, the Pd speciation of Pd-loaded zeolite materials is sensitive to the pretreatment conditions applied. The presence of water during high temperature treatment was shown to enhance Pd dispersion of materials with high concentrations of PdO_x particles.[98] However, the effect of water on ion-exchanged Pd is less completely understood, though the behavior of metal migration during hydrothermal treatment has been shown to be dependent on the framework structure and pore size of the material.[59, 122] The effect of water on the FT-IR spectrum of oxide materials that contain aluminum (such as zeolites and alumina) further complicates this analysis, as water association with zeolite OH sites leads to broad spectral intensity shifts over much of the IR range. This phenomenon results in the appearance of pseudo-maxima that can easily be misinterpreted as real spectral features.[74, 123] To provide example and comparison for later spectra, the time-resolved adsorption of water over 1.4% Pd-BEA and 0.7% Pd-CHA is shown in Figure 2.8. These fingerprints will be used to identify water-related pseudo-maxima throughout this work. It is especially notable that water pseudo-maxima appear

in the NO and CO stretching regions, and even trace quantities of water present in the gas feed leads to the appearance of these features. This is a further indication of the importance of rigorous gas drying in deconvoluting the effects of water from other adsorbates.

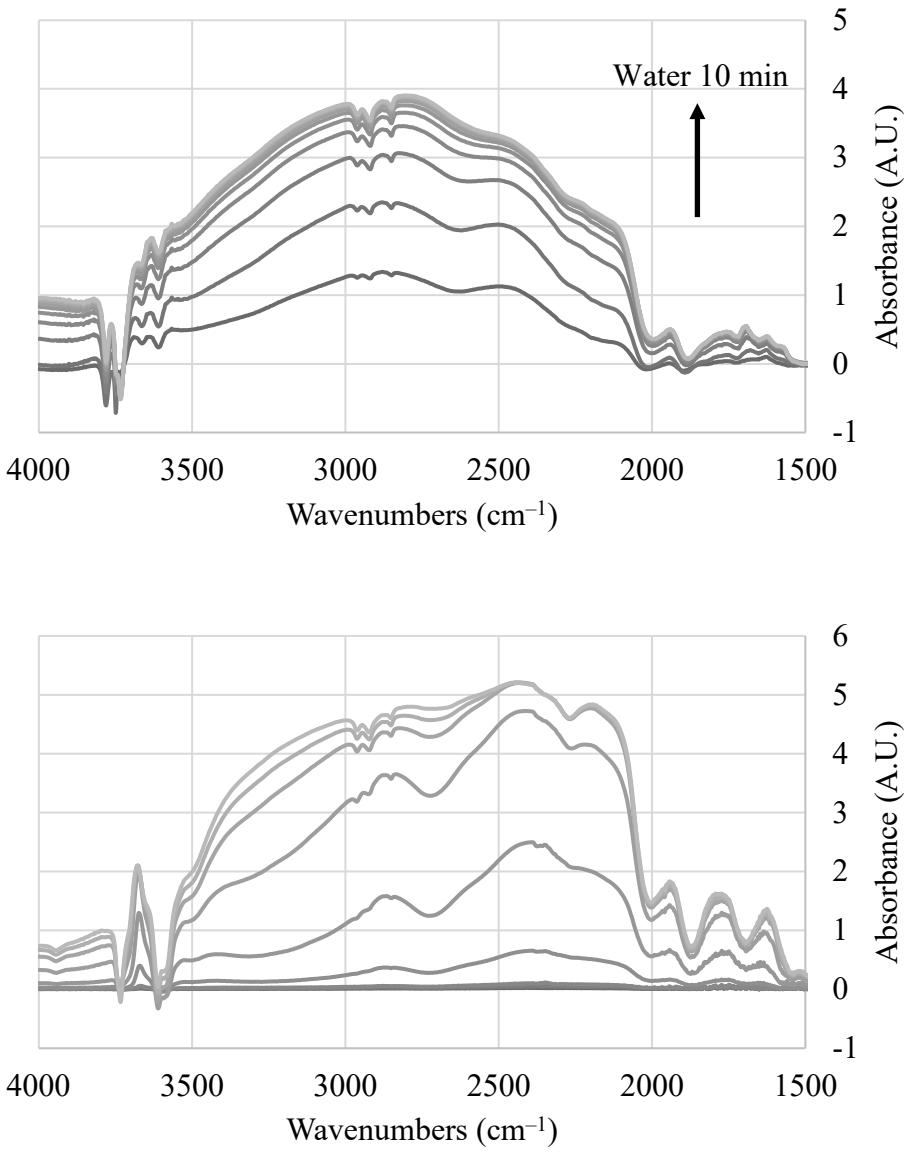

Figure 2.8 1.4% Pd-BEA (top), 0.7% Pd-CHA (bottom): DRIFT spectra of water adsorption after pretreatment at 500 °C for 1 h with Ar rigorously dried by cold trap. The materials were cooled in dried Ar to 25 °C prior to adsorption. 1-2% water in Ar was adsorbed for 10 min, Ar being wetted by room temperature bubbler.

2.4.1 1.4 % Pd-BEA

To assess the impact of water on Pd speciation, 1.4% Pd-BEA was subjected to treatment at 500 °C in either Ar or air with varying amounts of water present in the feed gas, followed by CO adsorption at 25 °C (Figure 2.9). The DRIFT spectrum obtained after treatment of 1.4% Pd-BEA in dried Ar shows a predominance of Pd^{+} and super-electrophilic Pd^{2+}, while use of untreated Ar (i.e., Ar fed directly from the gas cylinder) results in a loss of super-electrophilic Pd^{2+} and $[Pd^{2+}(OH)]^{+}$ in favor of Pd^{+} and Pd^{0}. This trend continues for the material treated in wetted Ar, the only remaining $Pd^{n+}(CO)$ bands appearing at 2154, 2130, and 2119 cm^{-1}, with total elimination of $[Pd^{2+}(OH)]^{+}$ and super-electrophilic Pd^{2+}. Metallic $Pd^{0}(CO)$ bands are largely absent on the material pretreated in dried Ar. The appearance of Pd^{0} after treatments containing water can be interpreted as the reduction of ion-exchanged Pd to Pd^{0} particles. Notably, the least electrophilic of the Pd^{2+} species (2154 cm^{-1}) is more resilient to water exposure than the other four divalent Pd species. The super-electrophilic bands are totally absent after exposure to water, an indication that these species have undergone reduction to Pd^{0} particles as described in Equation 8.

$$Pd(II) - (Z)_2 + H_2O \rightarrow Pd(0) + 2H^{+}Z^{-} + \frac{1}{2}O_2 \quad (8)$$

The fact that the least electrophilic divalent Pd is less susceptible to reduction by water suggests that this process occurs with Pd acting as electrophile and water acting as a nucleophile, though the intricacies of this mechanism remain to be determined. These data also indicate that this Pd is in a substantially different environment than its counterparts, i.e. NNN Al sites vs NNNN Al sites. Additionally, since this reaction produces O_2, the equilibrium must lie to the right given that the presence of O_2 does not prevent water from reducing Pd (see Figure 2.9). This mechanism also implies the need for Pd site proximity, since two Pd atoms would need to be reduced to produce one O_2 molecule. It is possible that PdO_x particles are also reduced to Pd^{0} by water, though their role cannot be readily ascertained from these data, due to their lack of CO adsorption. However, the role of PdO_x particles will be discussed more thoroughly in the next section.

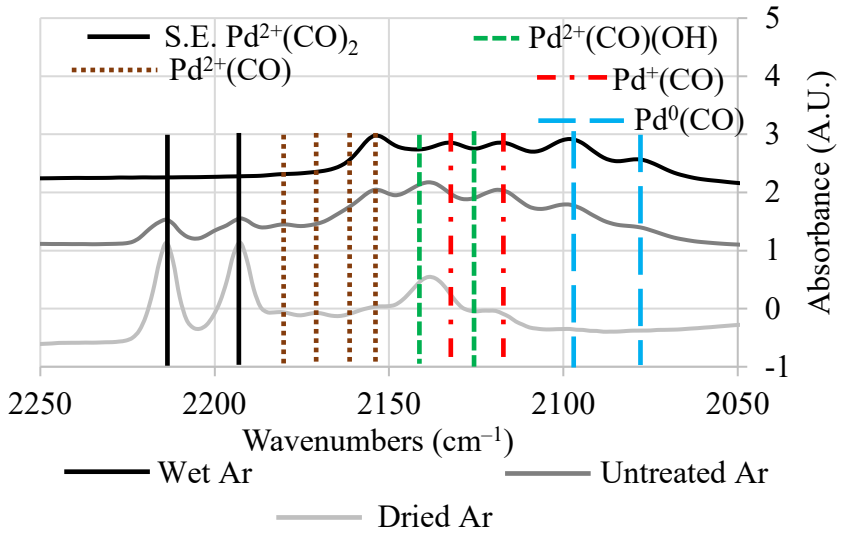

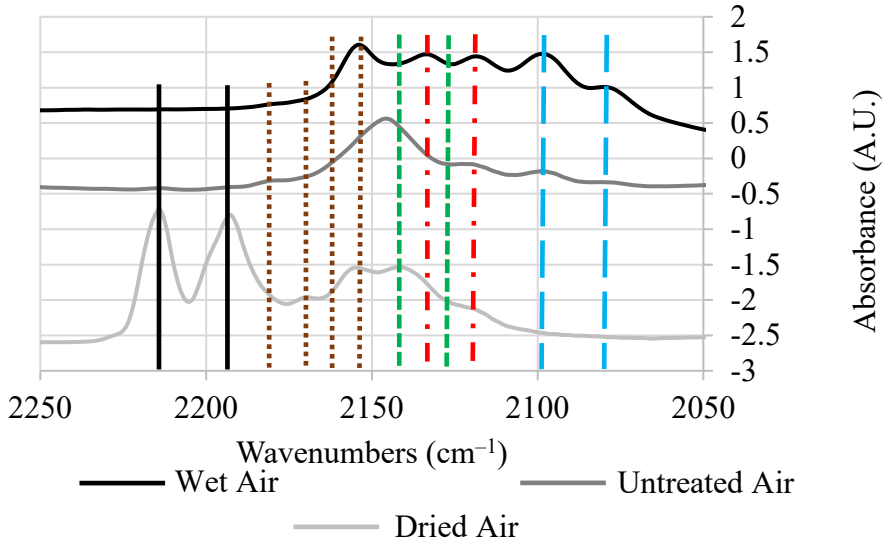

Figure 2.9 DRIFT spectra of CO adsorption onto 1.4% Pd-BEA after pretreatment at 500 °C for 1 h with Ar (top) or air (bottom) wetted by bubbler, untreated, or rigorously dried by cold trap. The material was cooled in dried Ar to 25 °C prior to adsorption. 1000 ppm CO in Ar was adsorbed for 10 min at 25 °C.

The results of pretreatment in air are also shown, the behavior being somewhat different while also reinforcing the above conclusions. The material pretreated in dried air reveals an abundance of Pd^{2+}, $[Pd^{2+}(OH)]^{+}$ and super-electrophilic Pd^{2+} as well as lesser quantities of Pd^{+}. Untreated air produces a broad band centered around 2144 cm^{-1} that consists primarily of $[Pd^{2+}(OH)]^{+}$, though this feature also includes contributions in

the range of Pd^{2+} (2154 cm^{-1}) and Pd^{+} (2132 cm^{-1}). Super-electrophilic Pd^{2+} is absent here, suggesting a greater concentration of trace water in the air cylinder and thus providing an explanation for the appearance of weak Pd^{0}(CO) bands in this spectrum while the majority of other Pd is maintained in the divalent state. The spectrum of the material pretreated in wetted air closely resembles the spectrum of the material treated in wetted Ar, a result indicating that while O_2 partial pressure exerts an influence at low water partial pressure by oxidizing Pd^{+}, this effect is eventually negated at higher water pressures.

The corresponding spectra of the low-frequency metallic $(Pd^{0})_x$(CO) bands are shown in Figure 2.10. Both of the wetted feed gases lead to the formation of a strong $(Pd^{0})_2$(CO) band at 1950 cm^{-1} while the dried and untreated spectra show only very weak bands at 1950, 1990, and 1790 cm^{-1}. The band at 1950 cm^{-1} is presumably a species analogous to that observed at 1890 cm^{-1} on Pd-CHA, representing CO adsorbed on a pore-confined Pd metal particle. The higher wavenumber of this band on 1.4% Pd-BEA is an effect of the greater BEA pore diameter, allowing a greater number of Pd atoms to agglomerate before becoming trapped, thus shifting the frequency of adsorbed CO to higher wavenumbers.[119] The band is also broader than that observed on Pd-CHA, this again being an effect of the framework structure, as BEA zeolite has irregular channels with a greater diversity of pore diameters that can support a greater diversity of Pd particle sizes. It can therefore be inferred that the band at 1990 cm^{-1} represents CO adsorbed on bulk Pd particles outside the framework, as this band appears on both zeolites examined here and on other materials in literature reports.[82, 124] The appearance of small quantities of doubly and triply bridging CO on the material treated under dry conditions can be explained by the work of Vannace et al. that shows the extinction coefficients of metallic Pd(CO) bands increase with decreasing frequency, indicating small populations of $(Pd^{0})_2$(CO) and $(Pd^{0})_3$(CO) can be apparent even when Pd^{0}(CO) bands are absent.[125]

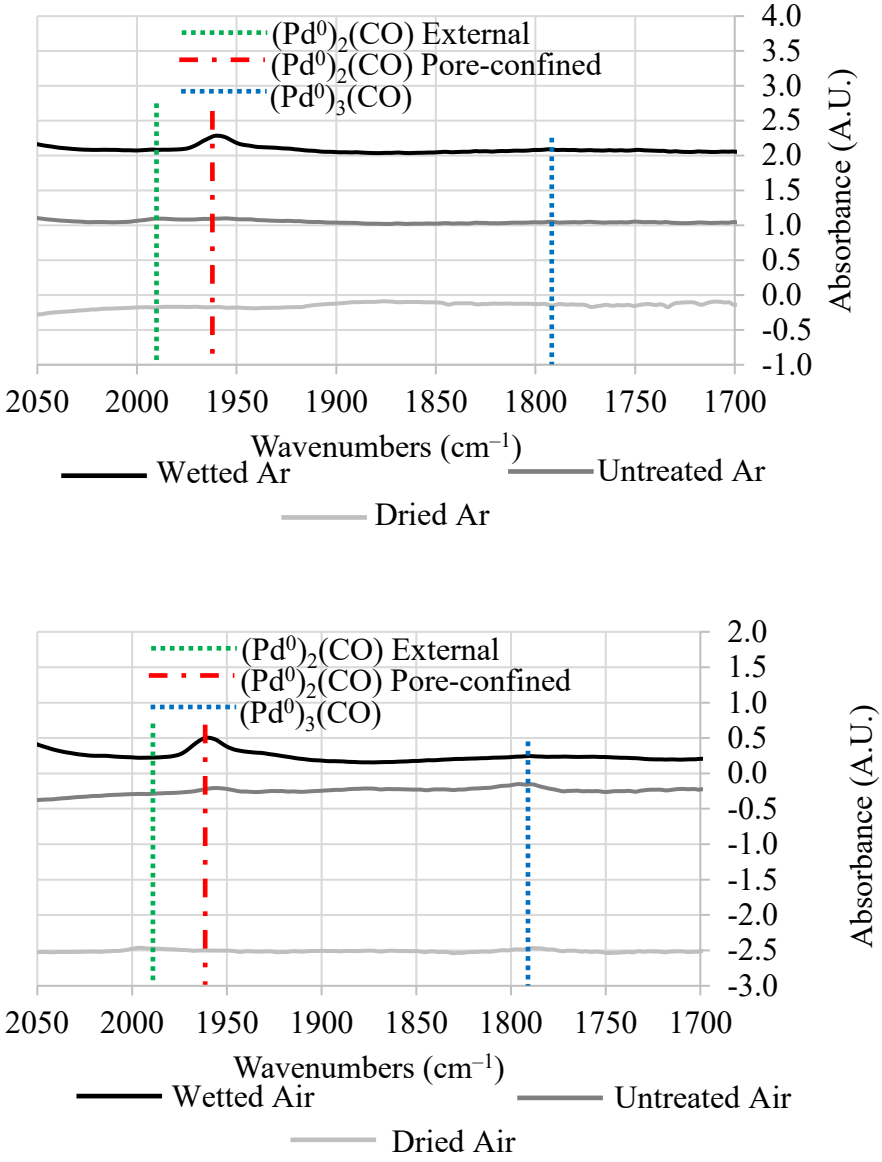

Figure 2.10 DRIFT spectra of CO adsorption onto 1.4% Pd-BEA after pretreatment at 500 °C for 1 h with Ar (top) or air (bottom) wetted by bubbler, untreated, or rigorously dried by cold trap. The material was cooled in dried Ar to 25 °C prior to adsorption. 1000 ppm CO in Ar was adsorbed for 10 min at 25 °C. Spectra correspond to those presented in Figure 2.9.

2.4.2 0.7 % Pd-CHA

Similar experiments were performed on 0.7% Pd-CHA, the results being shown in Figure 2.11. The Pd speciation of this material is much more stable in the presence of water at high temperatures, even the super-electrophilic Pd^{2+} remaining after treatment in wetted Ar. This agrees with the result of Khivantsev et al., who have previously reported the stability of this species on Pd-SSZ-13 in the presence of water at room temperature.[74] This is a remarkable result as the $[Pd(CO)_4][Sb_2F_{11}]_2$ complex that exhibits CO bands similar to this species readily undergoes reduction upon exposure to water as observed for Pd-BEA.[80] Nonetheless, the material pretreated in wetted Ar does show a decrease in the abundance of $[Pd^{2+}(OH)]^+$ and super-electrophilic Pd^{2+}, while Pd^+ species grow more abundant along with the appearance of a shoulder at 2090 cm^{-1} corresponding to CO adsorbed at metallic Pd. The low-frequency region also shows an increase in the intensity of the band corresponding to pore-confined $(Pd^0)_2(CO)$ again indicating reduction by water leads primarily to the production of small, pore-confined Pd metal particles. Other studies have shown the preferential production of such particles over larger particles outside the framework can lead to improved Pd dispersion upon re-oxidation.[59, 107] The spectra of 0.7% Pd-CHA treated in air with various concentrations of water (not shown) are practically identical to those of the material pretreated in Ar, another indication that the Pd exchanged onto this material is more resilient to reduction.

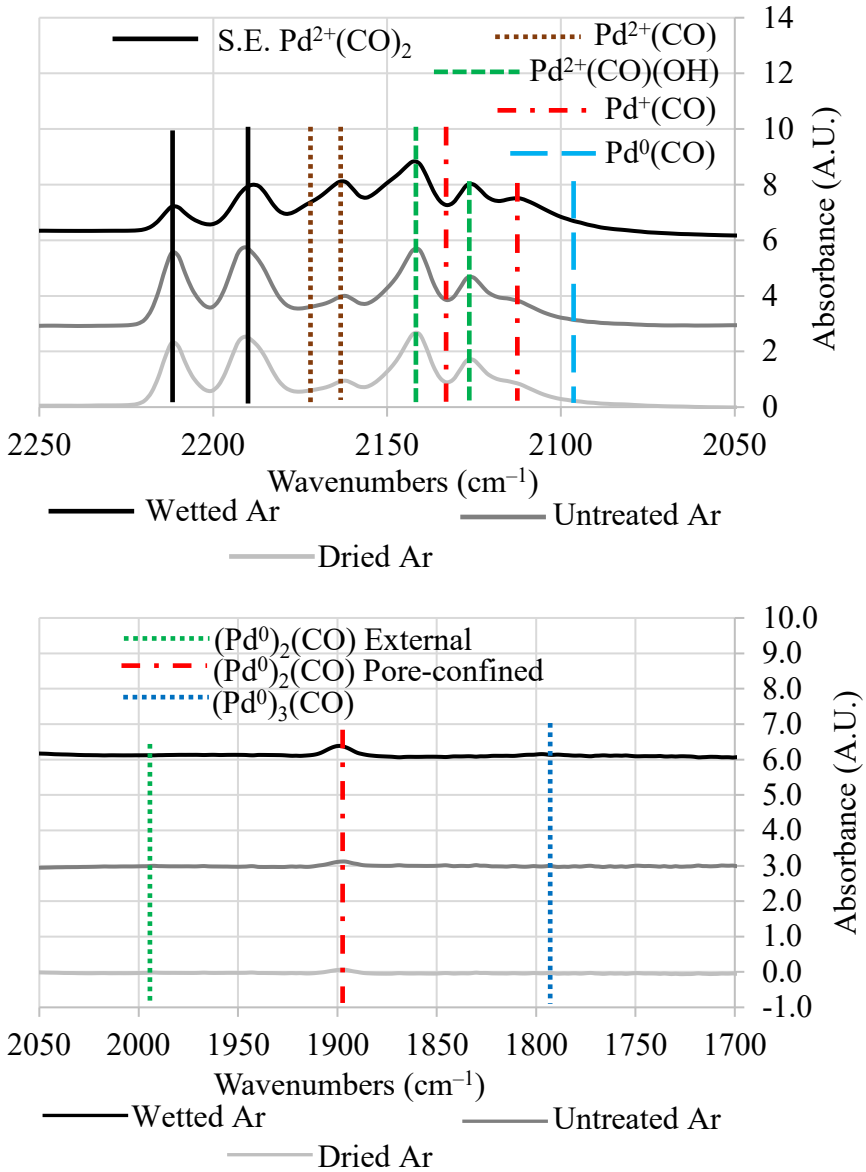

Figure 2.11 DRIFT spectra of CO adsorption onto 0.7% Pd-CHA after pretreatment at 500 °C for 1 h with Ar wetted by bubbler, untreated, or rigorously dried by cold trap. The material was cooled in dried Ar to 25 °C prior to adsorption. 1000 ppm CO in Ar was adsorbed for 10 min at 25 °C. Top: Ionic Pd range. Bottom: metallic Pd range.

Whether or not PdO_x particles can be reduced by water is difficult to ascertain, though the higher concentration of these particles on 0.7% Pd-CHA means reduction of PdO_x on this material should be more obvious. To further understand the reducing effects of water on Pd-CHA, the material treated in wet air was subsequently treated in dry air at 500 °C for 1 h prior to CO adsorption to ascertain the degree of reversibility of water

reduction. The comparison of this spectrum with the CO adsorption spectrum of the as-prepared material pretreated in air is shown in Figure 2.12. Remarkably, full restoration of ionic Pd is observed upon re-oxidation in dried air along with a slight increase in the abundance of super-electrophilic Pd^{2+} over the as-prepared material. The low-frequency region is also notable as the abundance of pore-confined Pd particles increases as well, along with the appearance of a shoulder below 1890 cm^{-1} that indicates the presence of still smaller Pd particles. The increased intensity of both ionic and metallic Pd(CO) bands after re-oxidation suggests that some PdO_x particles have been reduced to Pd metal by water and then are either re-distributed as ion-exchanged Pd cations or attain sufficient particle size to become trapped and stabilized by the zeolite pore. The PdO_x particles susceptible to reduction in water likely consist of only the smallest particles in the PdO_x population. It is notable that this result is similar to the effects produced by treatment in H_2, PdO_x reduction being proposed to occur through a pathway that also yields primarily small Pd particles.[82, 103, 108, 122]

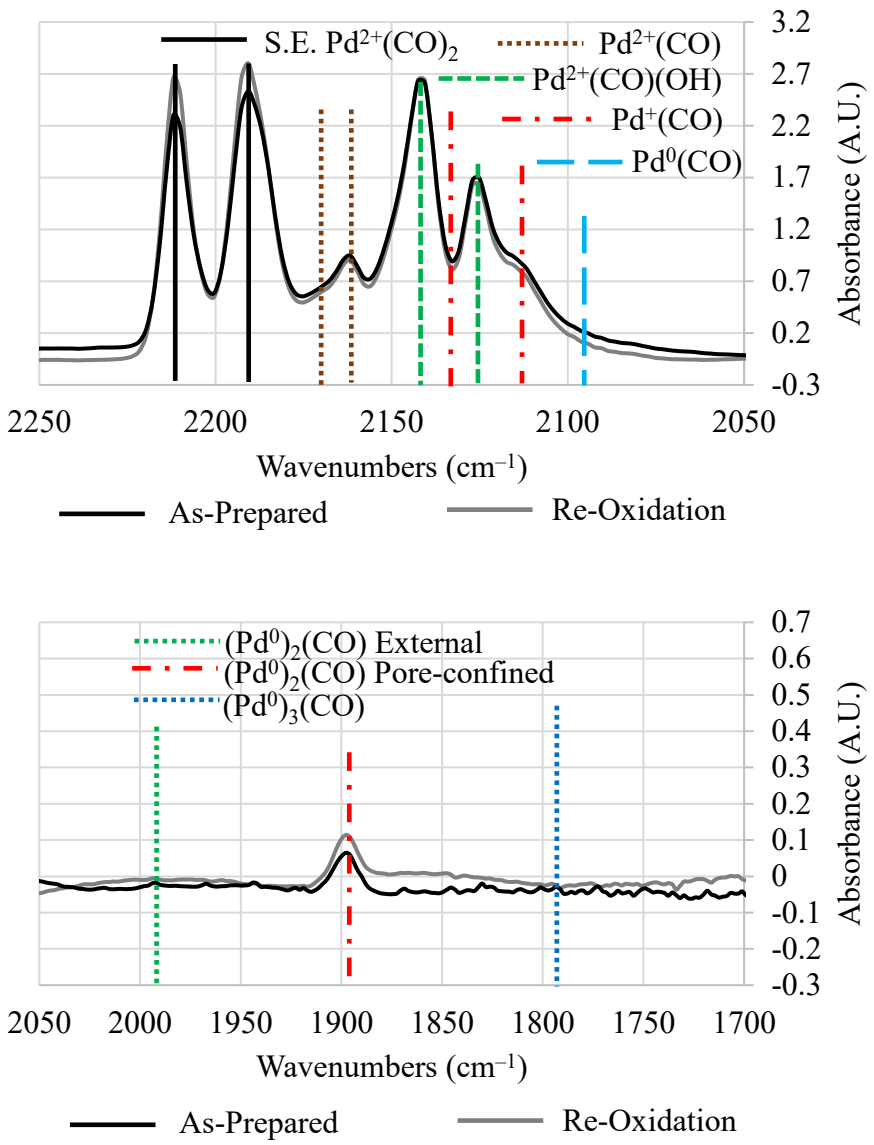

Figure 2.12 0.6% Pd-CHA: DRIFT spectra of CO adsorption after sequential pretreatment at 500 °C for 1 h with dried air, air wetted by bubbler, and finally dried air. Only the as-prepared and re-oxidized spectra are shown for clarity. The material was cooled in dried Ar to 25 °C prior to adsorption. 1000 ppm CO in Ar was adsorbed for 10 min at 25 °C between each pretreatment. Top: ionic Pd range. Bottom: metallic Pd range.

The above results show the negative impact of water on ion-exchanged Pd, even trace quantities of water being demonstrated to reduce cationic Pd on the larger pore BEA zeolite. The super-electrophilic Pd^{2+} species is shown to be especially susceptible to the presence of water on 1.4% Pd-BEA, while this species is stabilized to a remarkable degree by the smaller CHA pore structure. Further, reduction by water is shown to lead to the preferential formation of small Pd metal particles confined within the zeolite framework, a positive result that indicates much of the reduced Pd can be recovered by re-oxidation. The reduction of Pd by water is shown to be sensitive to the electrophilicity of Pd^{2+}, the least electrophilic of these species being more resilient to reduction under these conditions. This reaction is also shown to be insensitive to the presence of oxygen above a certain concentration of water, though effects are observable when only trace quantities of water are applied. Water is also proposed to lead to the reduction of small PdO_x particles on 0.7% Pd-CHA, the increased CO band intensity after re-oxidation resulting from the re-distribution of these particles as both ion-exchanged Pd and as Pd metal particles that grew large enough to be stabilized by the zeolite pores. Overall, the Pd speciation of the CHA material is much more stable than that of BEA, a behavior again attributable to the smaller CHA pores.

2.5 Effect of Water at Near-ambient Temperature

The observed sensitivity of 1.4% Pd-BEA to water demonstrates the need for evaluation of these reductive processes at temperatures relevant to PNA behavior. 1.4% Pd-BEA pretreated in dried Ar was subjected to sequential adsorption of CO and water to gain insight into the behavior of these adsorbates within this temperature regime. Figure 2.13 shows the results of adsorption of CO followed by adsorption of water for 10 min each in a balance of Ar. When CO is cut off and water was supplied, water pseudo-maxima appear immediately, and CO bands begin to diminish in intensity. Interestingly, evidence of $Pd^{+}(CO)$ remains even after 10 minutes of water exposure, suggesting that CO is bound more strongly to Pd^{+} than Pd^{2+}, a supposition supported by the higher CO desorption temperature of these species as described above. The super-electrophilic $Pd^{2+}(CO)_2$ bands disappear within five minutes, in conjunction with the appearance of a $(Pd^{0})_2(CO)$ band at 1950 cm^{-1} that reaches its maximum intensity at about the same time.

This indicates that the reduction of super-electrophilic Pd^{2+} by water proceeds even at 25 °C on Pd-BEA, a result that serves to explain the high degree of variability in the intensity of these species in literature reports.[76, 82, 103]

The opposite experiment was also carried out; Figure 2.14 shows the effect of saturating the material with water prior to CO adsorption. In this case, the CO band structure is extremely weak and so the spectrum of the water pseudo-maxima was used as the background. This results in considerable spectral noise as water begins to desorb, though $Pd^{n+}(CO)$ bands can still be resolved. Under these conditions, $Pd^{2+}(OH)(CO)$ bands are observed, suggesting that in the previous experiment, water merely displaces CO from these species rather than acting to reduce $[Pd^{2+}(OH)]^{+}$ to Pd^{+}. The $Pd^{2+}(CO)_2$ bands do not appear in this spectrum, confirming that the reduction of this species by water occurs even when this cation is not ligated by CO. The $(Pd^{0})_2(CO)$ band at 1950 cm^{-1} also appears in this spectrum, though examination of its behavior over time is complicated by an overlapping water pseudo-maximum.

The observation of differing CO adsorption behavior depending on the order in which adsorbates are applied is intriguing as this suggests the energies of adsorption for these two adsorbates are similar. The observation of the interaction of CO with $[Pd^{2+}(OH)]^{+}$ on the water saturated material is also notable, these species being suggested to be a key adsorption site in low-temperature PNA behavior.[59, 90, 107]

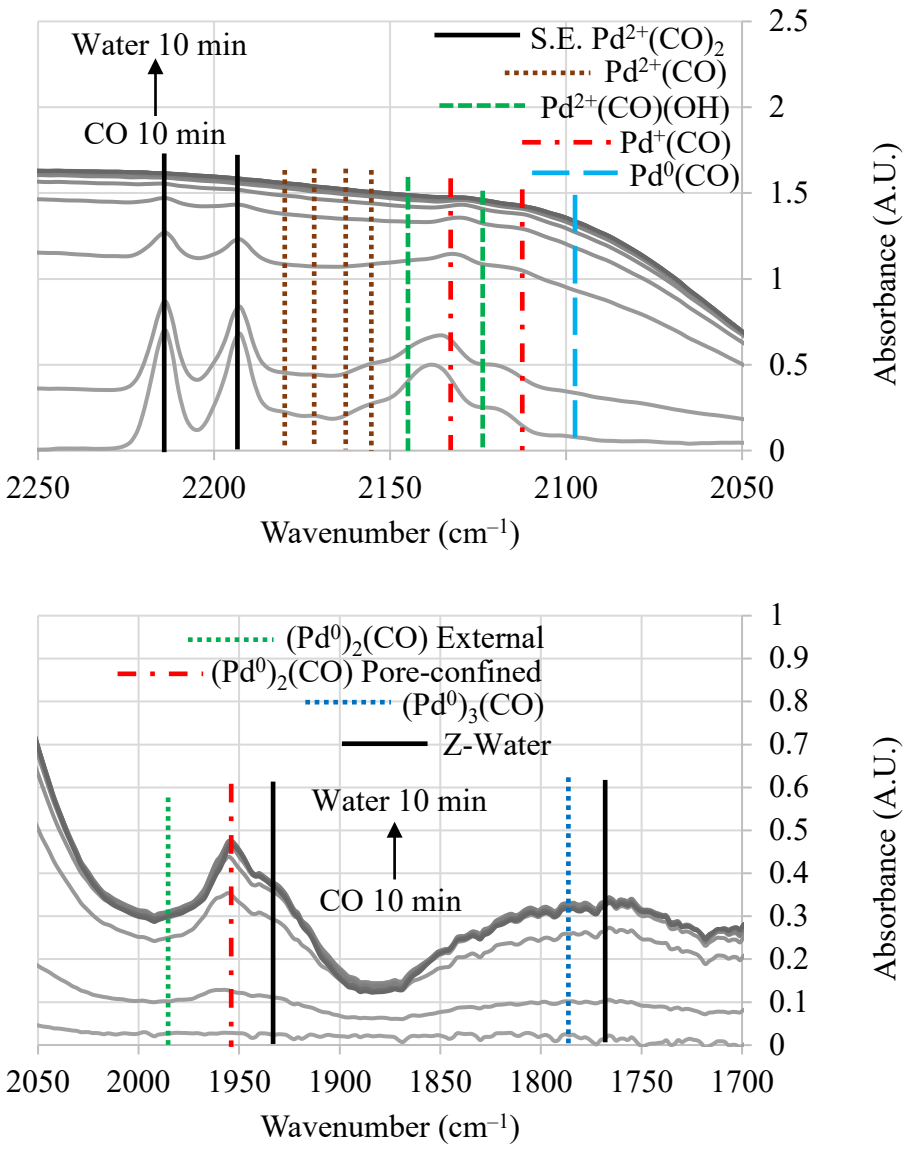

Figure 2.13 DRIFT spectra of 1.4% Pd-BEA pretreated at 500 °C for 1 h in Ar then cooled in dried Ar to 25 °C prior to adsorption. 1000 ppm CO in Ar was adsorbed for 10 min followed by adsorption of 1-2% water in Ar wetted by bubbler. Top: Ionic Pd range. Bottom: metallic Pd range.

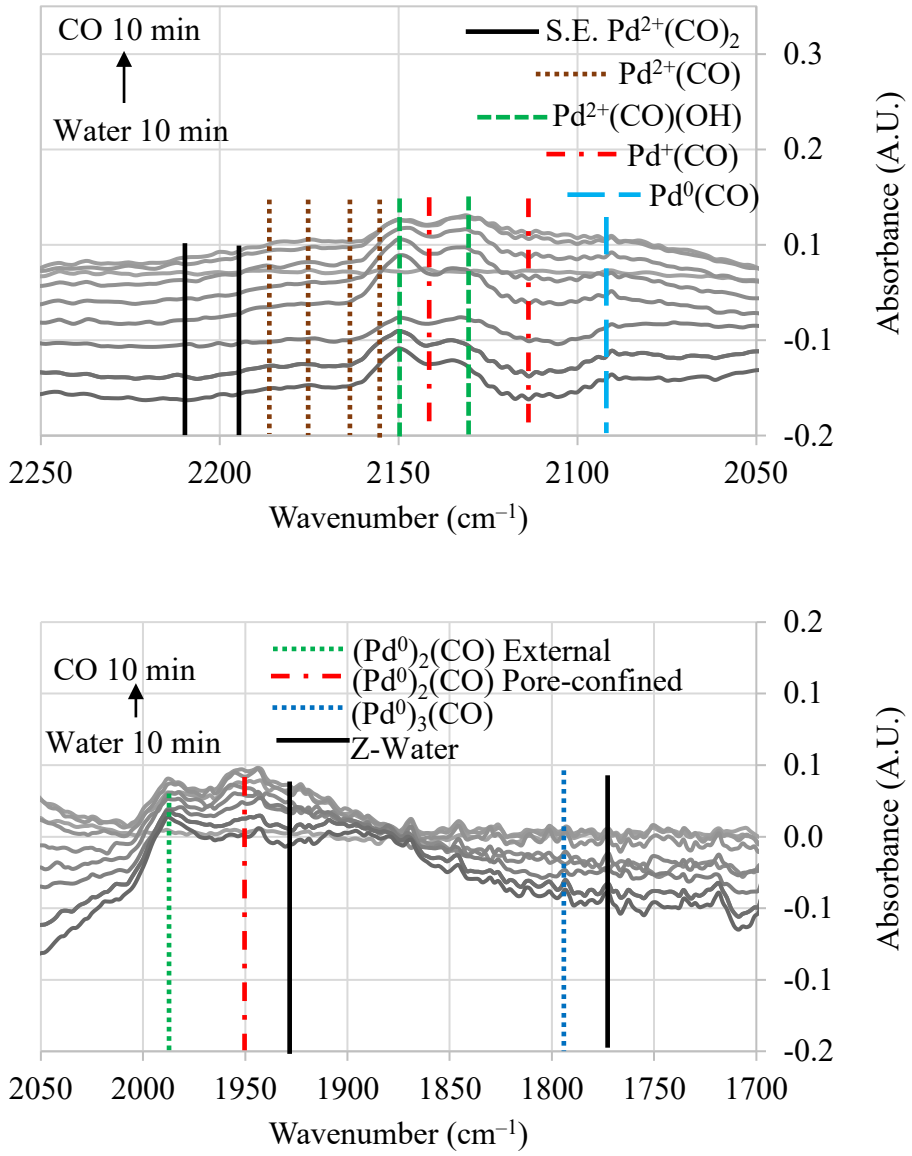

Figure 2.14 DRIFT spectra of CO adsorption onto 1.4% Pd-BEA for 10 min after water adsorption for 10 min. The material was pretreated at 500 °C for 1 h in Ar then cooled in dried Ar to 25 °C prior to adsorption. 1-2% water in Ar wetted by bubbler was adsorbed for 10 min followed by 1000 ppm CO in Ar. Top: Ionic Pd range. Bottom: metallic Pd range.

2.6 Conclusions

This chapter has focused on the development of a robust, evidence-based set of Pd(CO) band assignments for both Pd-BEA and Pd-CHA that serves to reconcile many of the disparate behaviors observed on Pd-loaded zeolites in other studies. The effect of Pd loading on BEA was examined, low Pd loadings and pretreatment in Ar being shown to favor Pd distribution as Pd^{+} while higher loadings and pretreatment in air leads to formation of greater quantities of Pd^{2+}, including a super-electrophilic Pd^{2+} species with CO band frequencies of ~2200 cm^{-1}. The presence of $[Pd^{2+}(OH)]^{+}$ was ascertained through the observation of Pd(OH) bands under various conditions, these species being behaviorally associated with CO bands that indicate formation of a Pd^{2+}-(OH)(CO) complex. This species is reduced to Pd^{+}(CO) at elevated temperatures, while Pd metal particles are also formed. The reducing effect of water on Pd speciation has been examined, 0.7% Pd-CHA shown to be more resilient than 1.4% Pd-BEA to reduction by water at high temperature. The observed sensitivity of Pd speciation to water concentration emphasizes the need to perform DRIFTS measurements under rigorously water-free conditions, these observations explaining some of the discrepancies observed in literature results. This reductive process appears to operate with Pd acting as an electrophile, as the extent of reduction by water is sensitive to the electrophilicity of the Pd being reduced, the most electrophilic Pd species present on Pd-BEA being reducible even at room temperature. The reduction of PdO_x particles by water was also proposed to occur, these re-distributing to ion-exchanged Pd or as particles that grew large enough to be trapped by the zeolite pore. These results are nonetheless promising, as the formation of small Pd metal particles has been found to be relatively benign to the long-term performance of these materials as such particles are readily re-dispersed.[59, 107] In fact, greater ion exchange can be achieved after such treatment when a large population of PdO_x particles is present, these species also being reduced and re-dispersed to ion-exchanged Pd, Pd^{0}, and PdO_x particles.

CHAPTER 3. EFFECT OF CO AND H_2 ON Pd SPECIATION

Given the sensitivity of the Pd speciation of these materials to water, the impact of more strongly reducing species present in the automotive exhaust stream presents a substantial impediment to the successful real-world implementation of PNA materials, especially under stoichiometric operation. H_2 and CO have already been demonstrated by Ryou et al. to have differing effects on Pd-loaded zeolites; H_2 preferentially forms small Pd particles due to diffusional limitations within the zeolite pore,[108] while CO is proposed to facilitate the mobility of Pd species through the formation of more mobile Pd-carbonyl species that are then deposited as large particles outside the framework, these external Pd particles being more susceptible to sintering.[108] The irreversible nature of this degradation pathway was further confirmed by Gu et al., reduction in CO leading to loss of NO_x storage capacity that could not be regenerated even by extended exposure to NO_2.[107] These studies support their conclusions with STEM analysis, this technique being able to resolve pore-confined Pd particles. However, no thorough analysis of this behavior by DRIFTS is present in the literature, though this method presents a convenient probe of Pd metal particle size by CO adsorption. Below, the reduction and re-oxidation behavior of both Pd-loaded zeolite materials is characterized by CO-DRIFTS, reduction in H_2 and CO being considered separately.

3.1 Effect of Reduction in CO Followed by Re-oxidation in Air

3.1.1 1.4 % Pd-BEA

1.4% Pd-BEA was treated in 1000 ppm CO in Ar for 1 h at 500 °C, followed by re-oxidation in air at 500 °C. The original state of the material was assessed by pretreatment in air followed by CO adsorption at 25 °C, this spectrum provided as reference. Shown in Figure 3.1, treatment in CO leads to near-total loss of ionic Pd, though the fact that any remains is somewhat surprising. This result is consistent, however, with the results of Gu et al. who report some populations of ionic Pd are less susceptible to reduction by CO than others, though the identity of this species is not made

clear in that study.[107] The ionic Pd observed after reduction consists primarily of Pd^{+} (2119 and 2130 cm^{-1}) and the least electrophilic Pd^{2+} (2154 cm^{-1}) species, along with a population of Pd metal particles. Meanwhile the super-electrophilic Pd^{2+} species is almost totally absent, this again being especially sensitive to reduction. Re-oxidation leads to a recovery of some ion-exchanged Pd, primarily in the form of Pd^{+} and the least electrophilic of the Pd^{2+} species, while little evidence of $[Pd^{2+}(OH)]^{+}$ is observed. The super-electrophilic Pd^{2+} also recovers to some degree, though it is still much less abundant than on the as-prepared material. This also serves as a further confirmation of the identification of CO bands corresponding to $[Pd^{2+}(OH)]^{+}$ as these species are readily reduced by CO at elevated temperatures, producing a CO-DRIFT spectrum much like that of the Ar pretreated material upon re-oxidation. With this information it can be inferred that the irreversible degradation of NO_x adsorption behavior by CO on Pd-BEA can be at least partially explained by the reduction of $[Pd^{2+}(OH)]^{+}$, this species failing to regenerate upon re-oxidation in the absence of water. The low-frequency region is also informative, the as-prepared material showing a population of external Pd-metal particles identifiable by CO bands at 1990 and 1790 cm^{-1}. These bands increase in intensity on the CO-reduced material, accompanied by the appearance of a band at 1950 cm^{-1} that corresponds to CO adsorbed onto pore-confined Pd particles. After re-oxidation, only water pseudo maxima are observed in this region, suggesting much of the metallic Pd either sintered, was re-distributed as ion-exchanged Pd, or formed PdO_x particles. Given the complex nature of the Pd speciation of these materials it is more likely that some or all these transformations are active under the conditions employed here.

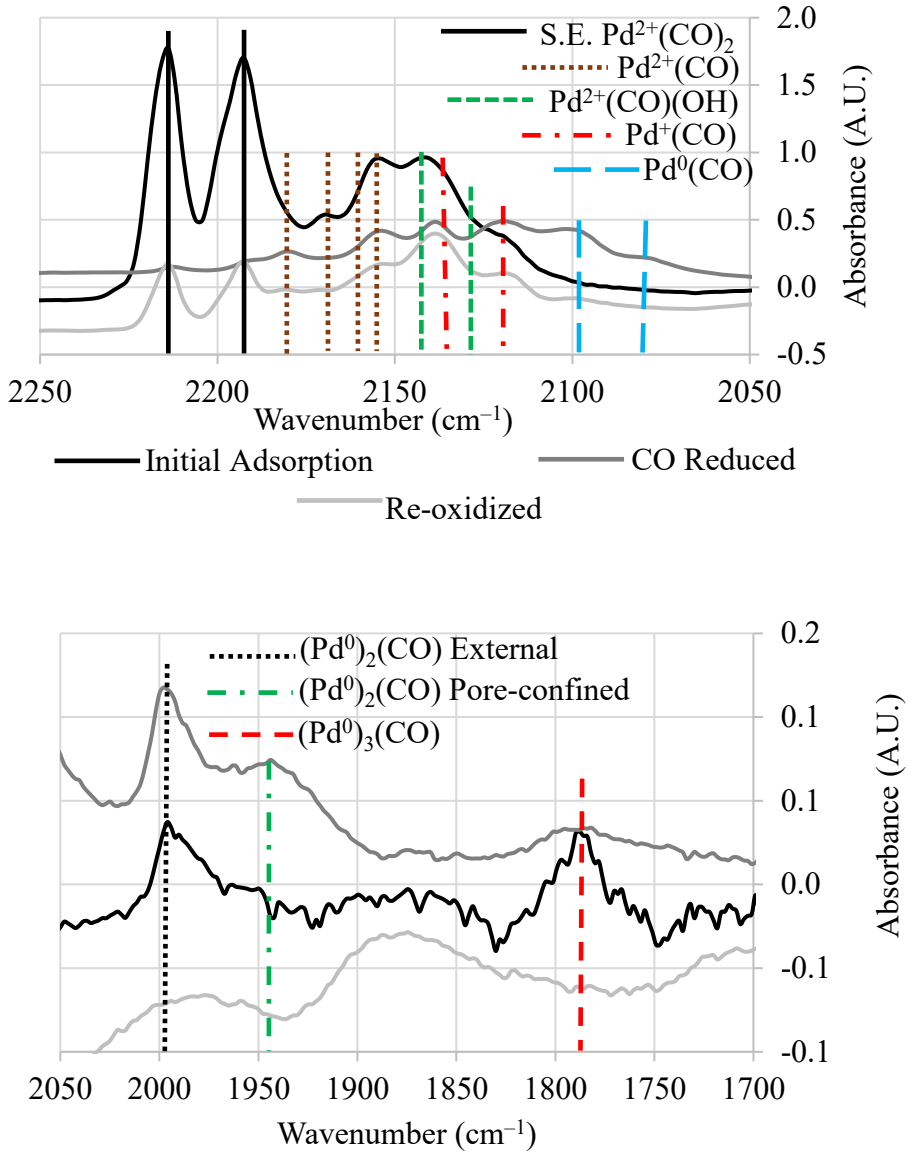

Figure 3.1 DRIFT spectra of CO adsorption onto 1.4% Pd-BEA after sequential pretreatment at 500 °C for 1 h with dried air, 1000 ppm CO in Ar, and finally dried air. The material was cooled in dried Ar to 25 °C prior to adsorption. 1000 ppm CO in Ar was adsorbed for 10 min at 25 °C between each pretreatment. Top: ionic Pd range. Bottom: metallic Pd range.

3.1.2 0.7 % Pd-CHA

Similar experiments performed on 0.7% Pd-CHA reveal a distinctly different behavior; reduction in CO still leads to the loss of most ion-exchanged Pd, though the species that remain differ as shown in Figure 3.2. In this case, $[Pd^{2+}(OH)]^{+}$ remains after CO reduction while Pd^{+} and un-ligated Pd^{2+} species are lost. This result indicates that the reactivity of the various Pd species to CO is different on CHA, favoring the reduction of Pd^{+} and Pd^{2+} to Pd metal particles, while $[Pd^{2+}(OH)]^{+}$ seems to be more resilient, the opposite of the behavior observed on BEA. The mechanisms through which these differing processes occur is not made clear by these data, since quantitation of IR bands is not possible and the full role of PdO_x particles cannot be established. Re-oxidation leads to almost complete regeneration of the super-electrophilic Pd^{2+} species, while all the other ionic Pd species are recovered somewhat, though they fail to approach their original intensity.

The low-frequency IR region shows the presence of primarily bulk Pd metal particles outside the framework after CO reduction, corresponding CO bands observed at 1990 and 1790 cm^{-1} for $(Pd^0)_2(CO)$ and $(Pd^0)_3(CO)$, respectively. This result agrees with the results from Pd-BEA and the work of Gu et al. and Ryou et al. in that CO leads to greater Pd mobility and thus enhances agglomeration of large particles outside the zeolite framework.[107, 108] It is notable that the pore-confined Pd particles already present on the material are also lost during CO reduction, suggesting these species can also be rendered mobile in the presence of CO. Further, the fact that Pd(CO) bands fail to recover to their original intensity also points to two potential fates for PdO_x particles during this process, one being that these particles fail to reduce, or that they reduce completely to large metallic Pd particles and sinter, either effect leading to a failure of these particles to re-distribute as observed for reduction by water.

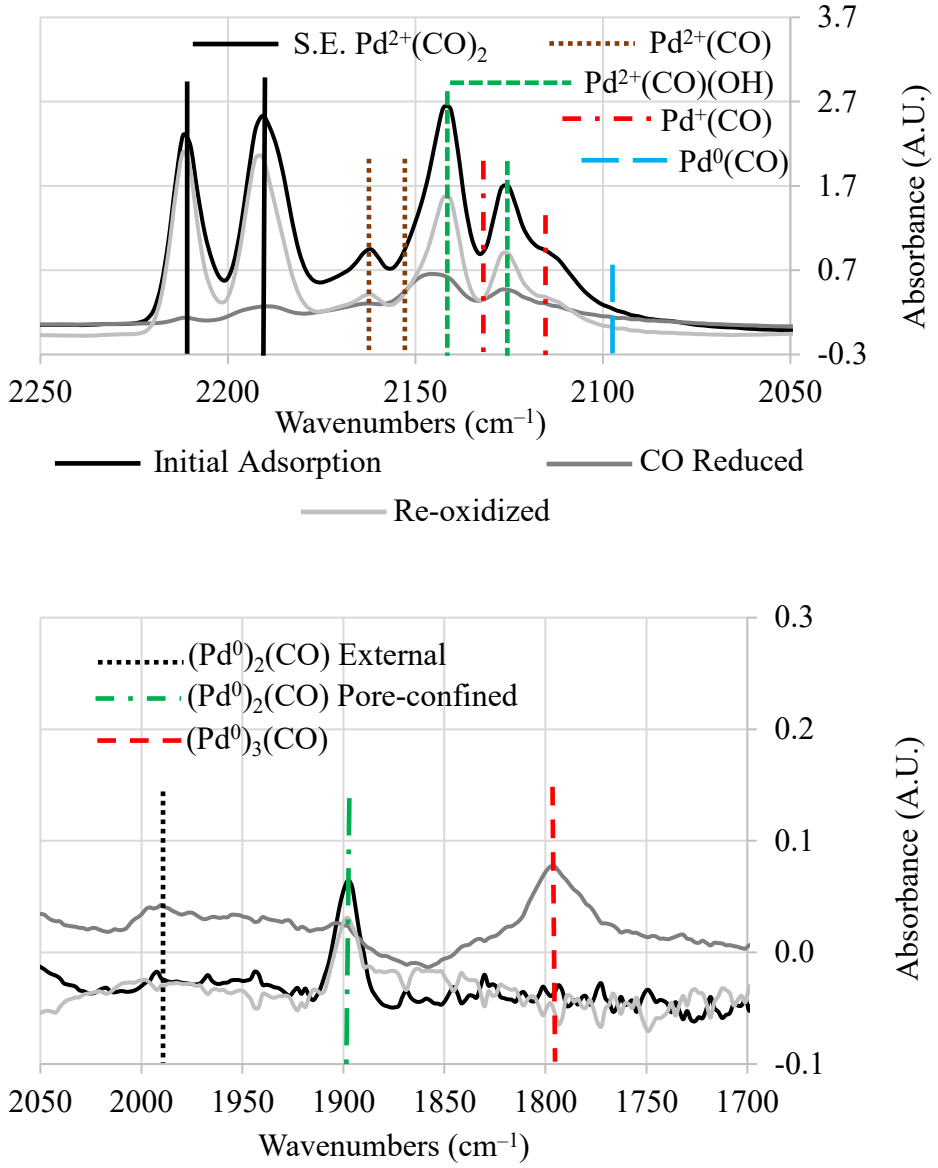

Figure 3.2 DRIFT spectra of CO adsorption onto 0.7% Pd-CHA after sequential pretreatment at 500 °C for 1 h with dried air, 1000 ppm CO in Ar, and finally dried air. The material was cooled in dried Ar to 25 °C prior to adsorption. 1000 ppm CO in Ar was adsorbed for 10 min at 25 °C between each pretreatment. Top: ionic Pd range. Bottom: metallic Pd range.

3.2 Effect of Reduction in H_2 followed by Re-oxidation in Air

3.2.1 1.4 % Pd-BEA

Results from a series of experiments analogous to those presented in the previous section using H_2 as reductant on 1.4% Pd-BEA are shown in Figure 3.3. The H_2-reduced material shows a more complete loss of ionic Pd than was observed for reduction in CO, though evidently some Pd^+ remains, possibly as Pd^+ on the surface of Pd metal particles as described by Hess et al.[93] The predominant feature in the ionic Pd frequency range falls at about 2100 cm^{-1} corresponding to $Pd^0(CO)$ species. A weak feature occurs at 2186 cm^{-1}, though this band corresponds to CO adsorbed at a zeolite Lewis acid site, this species being masked by Pd(CO) bands under other circumstances.

Re-oxidation leads to the restoration of Pd^+, while $[Pd^{2+}(OH)]^+$ and super-electrophilic Pd^{2+} are restored to a lesser extent. Overall, this treatment leads to better recovery of ion-exchanged Pd than is observed after CO reduction, though the lower abundance of PdO_x particles on BEA prevents improvement of dispersion on re-oxidation. The recovery of $[Pd^{2+}(OH)]^+$ after H_2 reduction further indicates that this species is responsible for some of the irreversible degradation of Pd dispersion observed during CO reduction as it fails to re-appear in that case. The low-frequency region is also revealing, bands appearing at 1990 and 1950 cm^{-1} being representative of bulk and pore-confined Pd metal particles, respectively. Especially notable is the total absence of a band at 1790 cm^{-1} on the H_2-reduced material. This band represents $(Pd^0)_3(CO)$ and appears at an especially low frequency for such a species, an indication that this CO is highly coordinated to Pd and may represent a site where a single Pd atom has been lost to an Ostwald ripening-type process.[82, 126]

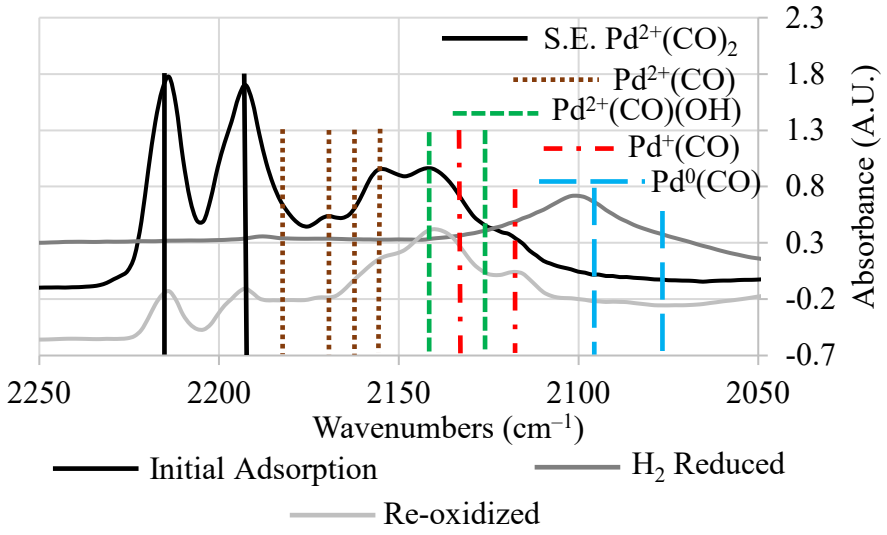

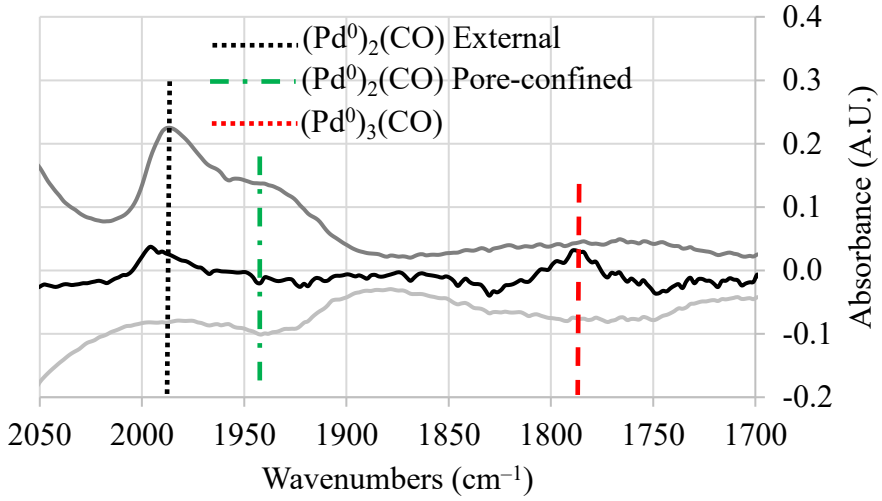

Figure 3.3 DRIFT spectra of CO adsorption onto 1.4% Pd-BEA after sequential pretreatment at 500 °C for 1 h with dried air, 10% H_2 in Ar, and finally dried air. The material was cooled in dried Ar to 25 °C prior to adsorption. 1000 ppm CO in Ar was adsorbed for 10 min at 25 °C between each pretreatment. Top: ionic Pd range. Bottom: metallic Pd range.

3.2.2 0.7 % Pd-CHA

The reduction and re-oxidation of 0.7% Pd-CHA in H_2 is shown in Figure 3.4, again showing a differing behavior from the material reduced in CO. The H_2-reduced spectrum presents a more complete loss of ion-exchanged Pd relative to the CO-reduced material, only a broad feature centered around 2100 cm^{-1} being in evidence. Again, CO adsorption at a zeolite Lewis acid site is observed, this time at 2194 cm^{-1}. The results of re-oxidation are more remarkable; the super-electrophilic Pd^{2+} is restored to its original intensity while the other ion-exchanged Pd species show a significant increase in intensity over the as-prepared material. This result is similar to that observed upon re-oxidation from water treatment and provides evidence that H_2 successfully reduces PdO_x particles into a form that can be re-dispersed to ion-exchanged Pd upon re-oxidation, unlike CO.

The behavior observed in the low-frequency region corroborates these results, the H_2-reduced material revealing the presence of a distribution of particles at and above the size of the pore-confined Pd particles, though below the bulk Pd particle frequency. Only a weak band representing bulk $(Pd^0)_2(CO)$ occurs at 1990 cm^{-1}. This result indicates that pore-confined Pd particles are mobilized during H_2 reduction, though they are still largely prevented from attaining the size of external Pd particles large enough to exhibit bulk Pd^0 behavior. Again, the $(Pd^0)_3(CO)$ band at 1790 cm^{-1} fails to appear. The increased Pd dispersion observed on re-oxidation of this material is further evidence that the CO adsorption site responsible for the 1790 cm^{-1} band is indicative of the agglomeration of Pd to large, external, Pd particles. Accordingly, this band fails to appear when sintering is limited, or in the absence of the $(Pd^0)_2(CO)$ band at 1990 cm^{-1} that is also representative of the presence of such particles. Re-oxidation again reveals an increase in the abundance of pore-confined Pd metal particles over the as-prepared material, though this effect is much more substantial than that observed when water was employed as reductant. This indicates reduction of PdO_x particles to small Pd metal particles that are then accessible for re-dispersion. Upon re-oxidation these small particles presumably begin to shrink and migrate, producing a large population of still smaller Pd particles that can be readily trapped by the zeolite pores or return to ion-exchange sites as cationic species.

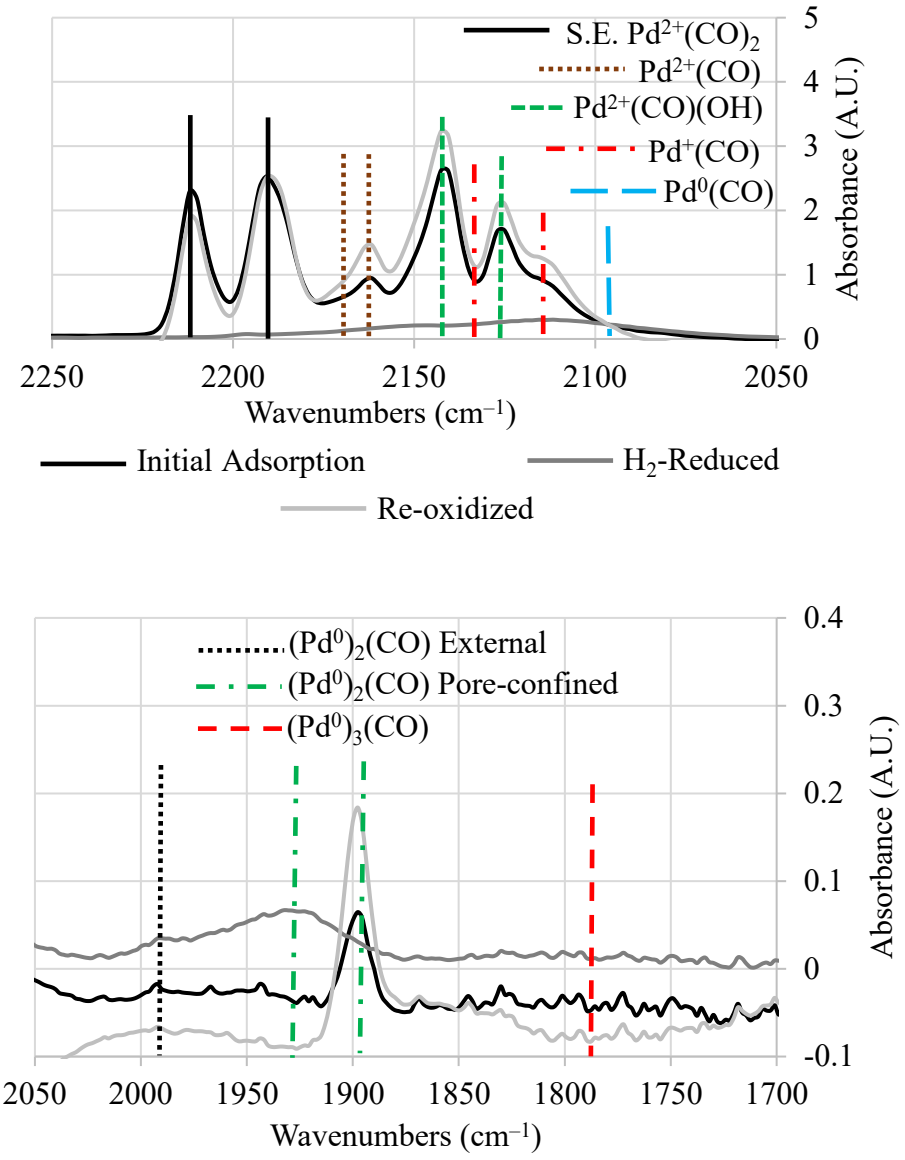

Figure 3.4 DRIFT spectra of CO adsorption onto 0.7% Pd-CHA after sequential pretreatment at 500 °C for 1 h with dried air, 10% H_2 in Ar, and finally dried air. The material was cooled in dried Ar to 25 °C prior to adsorption. 1000 ppm CO in Ar was adsorbed for 10 min at 25 °C between each pretreatment. Top: ionic Pd range. Bottom: metallic Pd range.

3.2.3 Other Experimental Methods

To corroborate the DRIFTS data presented above, XPS and microreactor-MS studies were employed to probe Pd speciation and NO_x adsorption/desorption behavior, respectively. Near-ambient pressure XPS was performed on 1.4% Pd-BEA after various pretreatments mirroring those performed in the DRIFTS studies. The atomic concentrations measured at the material surface are presented in Table 3.1, while the deconvoluted spectra are present in Figure S1 (supplementary data are included in Appendix 3). It is immediately apparent from the data that the amount of Pd observed is consistently less than 10 % of the total Pd present, while metallic Pd seems to be over-represented. For instance, only very weak metallic Pd(CO) bands were detected on air-pretreated 1.4% Pd-BEA and yet metallic Pd accounts for nearly one quarter of Pd observed by XPS under similar conditions. This indicates large, external Pd particles exert an outsized influence when this method is applied, ion-exchanged Pd being segregated into the zeolite crystallite and thus less visible to XPS. These data nonetheless serve to confirm that substantial differences exist between the material pretreated in Ar and air at 500 °C, these treatments showing 24.0 % and 77.5 % of Pd present in ionic form, respectively.

A Pd $3d_{5/2}$ band corresponding to super-electrophilic Pd^{2+} is also observed at 339.7 eV, this result being consistent with the reports of Khivantsev et al. who showed the presence of an identical band on a Pd-SSZ-13 material.[74] This band has been previously observed on Pd-BEA, though it was then attributed to Pd^{4+} ions due to the extremely high binding energy of this species.[76] This feature is absent from the BEA material pretreated at 750 °C, suggesting that super-electrophilic Pd^{2+} either decomposes, becomes more sensitive to trace water, or migrates away from the surface at this temperature. H_2 reduction leads to the formation of primarily metallic Pd, though a small amount of ionic Pd remains, corroborating the DRIFTS observation of Pd^{+} after H_2 reduction, again likely present on the surface of Pd metal particles.[93] This conclusion is supported by the observed maximum binding energy of the ionic Pd band shifting from 337.35 eV to 336.84 eV, suggesting the average oxidation state of this population of Pd has decreased.

Table 3.1 Atomic concentrations (%) as determined by XPS. Oxidized and metallic concentrations are derived from deconvolution of the Pd 3d spectra.

Pd-BEA	carbon	oxygen	aluminum	silicon	palladium	Oxidized Pd %	Metallic Pd %
As-Prepared	4.8	64.9	2.0	28.3	0.08	36.7	63.3
500 °C air	0.4	66.1	2.0	31.4	0.09	77.5	22.6
750 °C air	1.6	66.1	2.1	30.1	0.10	59.2	40.8
500 °C Ar	3.9	63.9	1.9	30.2	0.07	24.0	76.1
500 °C H_2	7.4	61.5	1.9	29.1	0.09	16.2	83.8

To examine the NO_x adsorption and desorption behavior in a semi-quantitative manner, microreactor-MS experiments were performed, these procedures mirroring those of the DRIFTS experiments except that the flow rate was maintained at 100 sccm due to system requirements. In each case, 1000 ppm NO in 10 % O_2 in He was adsorbed at 50 °C for 10 min followed by a purge for 1 h to remove weakly adsorbed species. This was followed by a temperature ramp at 10 °C per minute to 500 °C. The desorption of NO from both 1.4 % Pd-BEA and 0.7% Pd-CHA after H_2 reduction and subsequent re-oxidation is shown in Figure 3.5, the NO_x concentration in the gas phase being monitored by a calibrated MS signal. The 1.4 % Pd-BEA material shows a dramatic loss of NO_x capacity after reduction in H_2. Pd metal particles not only fail to adsorb NO_x, but also serve to block NO_x adsorption at zeolite sites, the same being true of 0.7 % Pd-CHA as NO_x desorption appears to be less intense from all adsorption sites when compared with the H-form materials (see section 4.4). For 1.4% Pd-BEA, re-oxidation leads to a slight enhancement of NO_x storage over the as-prepared material (~36%), a result that suggests the small quantity of PdO_x present on this material has been re-dispersed as species active for NO_x storage. These data also suggest that the super-electrophilic Pd^{2+} species and some of the other Pd^{2+} species observed on Pd-BEA do not participate in NO_x adsorption, as these are largely lost after re-oxidation as shown in Figure 3.3. As a result it can be inferred that Pd^{+} and $[Pd^{2+}(OH)]^{+}$ are the primary participants in NO_x storage on BEA, these species being regenerated preferentially, as observed by DRIFTS.

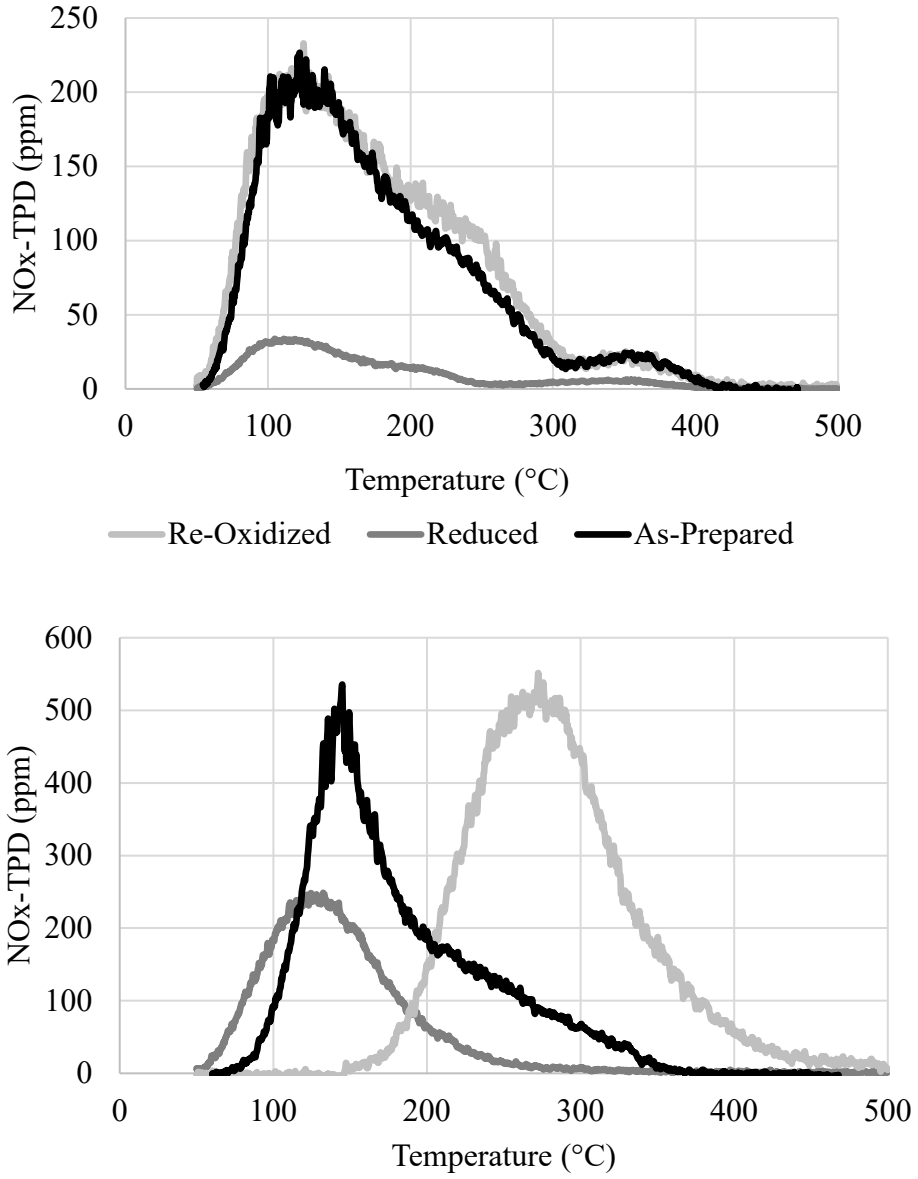

Figure 3.5 1.4% Pd-BEA (top), 0.7% Pd-CHA (bottom). NO_x TPD conducted in microreactor-MS with calibrated NO_x concentrations. Both materials were pretreated in 10% O_2 in He, 10% H_2 in He, and finally 10% O_2 in He. 1000 ppm NO in 10% O_2/He was adsorbed for 10 min at 50 °C followed by a 1 h purge in 10%O_2/He. TPD was carried out in 10% O_2/He at a ramp rate of 10 °C per min.

The 0.7% Pd-CHA material again presents a dramatically different result upon re-oxidation, a substantial improvement in the NO_x storage capacity being observed, along with a shift of desorption to higher temperatures that are more optimal for PNA behavior. This agrees with the DRIFTS observation that Pd-dispersion is improved upon reduction

and re-oxidation in H_2, though the reason for the disappearance of the low-temperature desorption event associated with zeolite sites is less clear. These data do suggest preferential formation of a site that desorbs NO_x at higher temperatures, comparison with DRIFTS results indicating that Pd^+ or $[Pd^{2+}(OH)]^+$ is likely responsible for this behavior due to the increased intensity of these bands upon re-oxidation. A potential explanation for the disappearance of the low-temperature desorption event could be a global change in the zeolite acid-base properties resulting from greater Pd dispersion, similar to that observed by Bisio et al. when Cs^+ was exchanged onto BEA zeolites, though an extensive computer modeling study would be required to confirm this supposition.[88]

3.3 Conclusions

To summarize the results of this chapter, the negative effects of CO on these materials has been demonstrated, CO particle agglomeration and sintering observed in previous studies being supported by in-situ DRIFTS. After re-oxidation from CO reduction, $Pd^{n+}(CO)$ bands fail to return to their original intensity, suggesting decreased abundance of these species relative to the as-prepared material. H_2 reduction is found to be more benign, producing primarily small, pore-confined metal particles that are readily re-distributed upon re-oxidation as ion-exchanged Pd, better recovery and even improvement of Pd dispersion on re-oxidation being observed. The role of PdO_x particles was indirectly explored, re-oxidation of 0.7% Pd-CHA showing more intense Pd(CO) bands than the as-prepared material, suggesting greater Pd-dispersion, this result being confirmed by microreactor-MS studies. It can therefore be concluded that PdO_x particles are also reduced to small Pd metal particles by H_2, a portion of these being converted to ion-exchanged Pd upon re-oxidation. This is also an indication that Pd reduction by water and H_2 have similar effects on Pd, as the water-pretreated material also exhibited this behavior.

Of crucial importance, H_2 reduction and re-oxidation leads to the formation of greater amounts of ion-exchanged Pd on CHA and incomplete recovery of ion-exchanged Pd on BEA. This suggests that not all ionic Pd species participate in NO_x adsorption on 1.4% Pd-BEA since its NO_x TPD behavior upon re-oxidation shows an enhancement of

NO_x storage over the as-prepared material, while ionic Pd(CO) DRIFTS band intensity is lost. The species primarily recovered on re-oxidation are Pd^+ and $[Pd^{2+}(OH)]^+$, an indication that these species are primarily responsible for NO_x adsorption at ion-exchanged Pd on BEA. The behavior of 0.7% Pd-CHA again differs substantially, preferential formation of a high desorption temperature NO_x storage site being observed. This leads to an increase in the lowest NO_x desorption temperature into a more favorable range while also increasing the overall NO_x storage capacity through improved Pd dispersion. Overall, 0.7% Pd-CHA shows greater resistance to Pd reduction than 1.4% Pd-BEA, a result that indicates the favorability of this material as a PNA candidate.

The focus of the next chapters will be on evaluating the effects of NO and NO_2 on 1.4 % Pd-BEA and 0.7% Pd-CHA, both as pretreatment gases and as adsorbates. Additionally, the role of zeolite sites in NO_x adsorption will be further explored, microreactor-MS studies again being used to corroborate DRIFTS results.

CHAPTER 4. ROLE OF PARTIALLY HYDROLYZED ZEOLITIC Al IN PASSIVE NO_X ADSORPTION

To gain further understanding of the sites available for Pd ion-exchange and their impact on NO_x adsorption, a more thorough examination of the zeolite OH band structure was carried out in addition to the examination of additional adsorbates, including CO_2, NO_2, NO, and NH_3.These adsorbates allow for analysis of the formation of carbonates, characterization of the NO_x adsorption sites, and characterization of the zeolite acid sites respectively. Emphasis will be placed on the comparison of the H-form materials and Pd-loaded materials to provide insight into the specific zeolite sites that Pd and other adsorbates occupy, while also exploring the behavior of P-HAl sites. The role of P-HAl in NO_x adsorption and desorption will be explored, the putative adsorbates and desorption events that correlate with the presence of P-HAl being identified. This work focuses on the BEA materials due to the near-absence of P-HAl species on CHA. DRIFTS data will be compared to the fundamental NO_x adsorption and desorption behaviors observed for both BEA and CHA, these data being collected by Dr. Yaying Ji in the initial phases of this work. Data provided by Dr. Ji are included in Figures 4.12-4.15, this work focusing primarily on the effects of NO_x adsorption temperature, as well as the rate of NO_x adsorption and quantity of NO_x adsorbed for the various materials.

4.1 Zeolite OH Bands and the Effect of Pd-loading

To identify the various zeolite OH species present on each of the materials prior to Pd exchange, DRIFT spectra of the OH regions of the H-form materials dehydrated at 500 °C for 1 h in flowing Ar were obtained (see Figure 4.1). A band appearing on H-BEA at 3785 cm^{-1} has been previously assigned to a P-HAl site of the type presented in Figure 4.2.[127] This species has been proposed to serve as an exchange site for the basic Cs^+ ion through the Lewis acidity of the under coordinated Al atom, rather than exchanging through a Brønsted acid mechanism.[88, 120, 128] This band is nearly absent from H-CHA, a result that again indicates CHA's greater resistance to dealumination, resulting from its smaller pore size. Other OH-stretching modes are observed as well, terminal and internal Si(OH) bands occurring at 3731 and 3745 cm^{-1} on both materials, EFAl(OH)

being evident at 3662 cm^{-1} and framework Al-O(H)-Si at 3606 cm^{-1}.[88, 120] Lastly, a band at 3577 cm^{-1} on H-CHA can be assigned to H-bonded OH groups, while this band is absent on H-BEA.[88, 127] Meanwhile, the P-HAl OH band is one of the most intense features, suggesting a substantial abundance of these sites on this BEA zeolite. The weakness of the Brønsted acid OH band of this material is also suggestive of the conversion of Brønsted acid sites to P-HAl Lewis acid sites as described by Bortnovsky et al., this process being greatly accelerated by steaming.[127] For reference, a complete listing of FT-IR bands discussed in this section is presented in Table 4.1.

Table 4.1 FT-IR band assignments for H-form BEA and CHA

Band (cm^{-1})	Assignment	Position	References
3577	H-Bonded OH	Framework OH	120, 128
3606	Al-O(H)-Si	Framework OH	120, 128
3662	EFAl	Non-framework OH	120, 127
3731	Si(OH)	Framework Defect OH	120
3745	Si(OH)	Framework Defect OH	120
3785	P-HAl	Partially Framework OH	88, 120
2125	CO	Pore Condensed	120
2171	CO	Brønsted acid sites	120
2194	CO	Lewis acid sites	120
2206	CO	P-HAl	120
890	P-HAl-O	Partially Framework Al-O	88, 120
940	Si-O	Framework	120

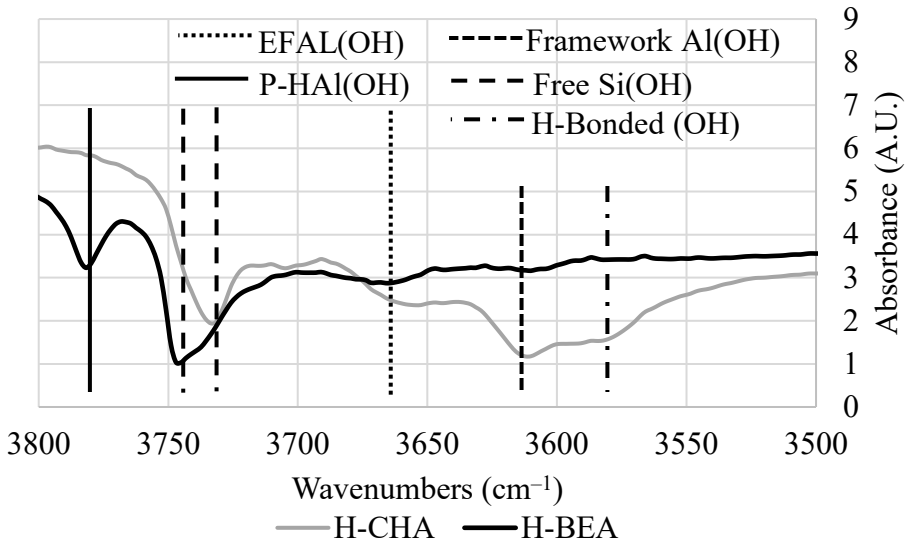

Figure 4.1 H-BEA, H-CHA: DRIFTS spectra of the OH region of the dehydrated materials after pretreatment at 500 °C for 1 h with Ar rigorously dried by cold trap. Materials were cooled in dried Ar to 25 °C prior to collection.

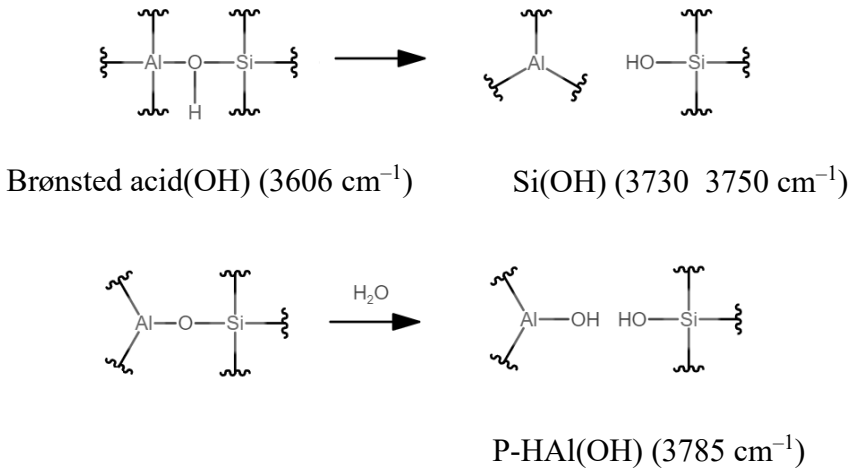

Figure 4.2 Mechanism of P-HAl formation proposed by Bortnovsky et al. along with the relevant OH band frequencies.[127]

The CHA materials show little change in the OH region upon Pd-loading (not shown), no readily discernable trends arising. The effect of Pd-loading on the OH region of the BEA zeolite IR spectrum was also examined; results being shown in Figure 4.3. The low intensity and overlapping development of Pd(OH) bands prevents effects on Brønsted sites from being observed, though the intensity of Si(OH) bands decreases with Pd-loading. This is likely due to Pd exchanging at adjacent Al-O(H)-Si sites, thus shifting

the Si(OH) stretch of nearby groups out of the usual frequency range. This behavior cannot be explained by Pd exchange at Si(OH) sites as these are not appreciably Brønsted acidic.[120] The spectrum of 1% Pd-Si-BEA is also included here, this material showing only weak Si(OH) bands.

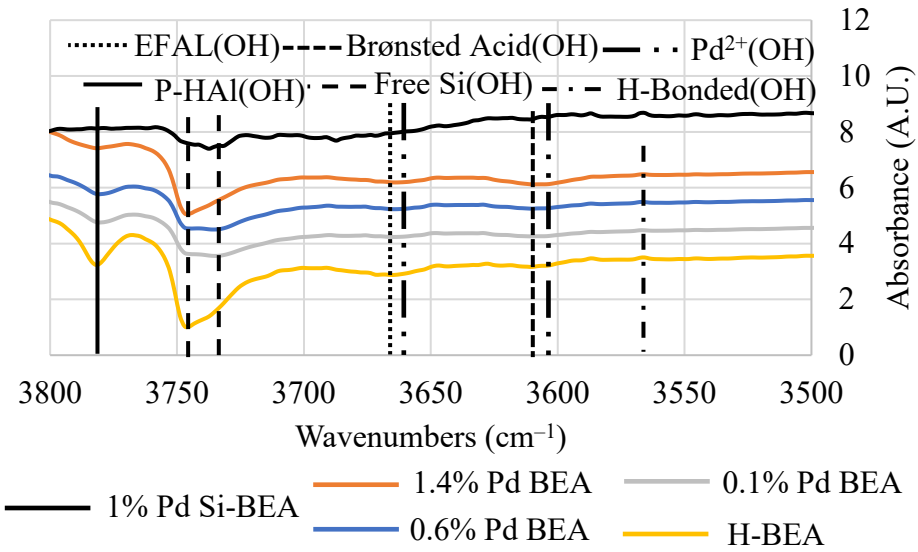

Figure 4.3 DRIFT spectra of the OH region of the dehydrated BEA materials after pretreatment at 500 °C for 1 h with Ar rigorously dried by cold trap. Materials were cooled in dried Ar to 25 °C prior to collection.

The P-HAl(OH) band is also reduced in intensity with Pd loading; however, the nature of this interaction is not well understood. Bisio et al. observed a similar phenomenon when Cs^+ was impregnated onto BEA zeolites, though it is unlikely that Pd will coordinate similarly given the Lewis acidity of Pd cations, exchange in the former case being proposed to occur due to the basicity of the Cs^+ ion. Cation exchange is only one of the proposed explanations for this effect, the other being that this site is leached by acid during the impregnation and calcination process, though Bisio et al. also suggest this effect should be inhibited when incipient wetness impregnation is employed (as it was for the materials discussed here), this method also being shown to achieve full quenching of Brønsted acidity upon Cs exchange.[88] While the Lewis acidity of P-HAl is well documented, this site has also been demonstrated to act as a Brønsted acid, though its acid strength is proposed to be intermediate to the essentially non-acidic silanols and the strongly acidic Al-O(H)-Si species.[120] As a result, Pd-exchange at this site could occur

through a Brønsted interaction wherein Pd^{+} or Pd^{2+} exchanges at P-HAl(OH) alone or at P-HAl(OH) and an adjacent Al(OH) site, respectively.

An alternative explanation for the decreased P-HAl(OH) band intensity is that Pd exchanges at a sufficient number of sites adjacent to P-HAl to disrupt the electronic environment and shift this OH stretch outside its normal frequency range as proposed for the silanol OH bands. However, close examination of the changes in this band from material to material suggest this is not the case, the initial change from H-BEA to 0.1% Pd-BEA being the largest. As Pd-loading is increased after 0.1%, the P-HAl(OH) band only decreases slightly in intensity despite the Pd loading eventually being nearly 14 times greater. This observation argues against a long-range effect as observed for the Si(OH) bands, as these bands change substantially and continuously as Pd loading increases. Due to the persistence of the band at 3785 cm^{-1}, apparently only a limited population of P-HAl sites is available for exchange, possibly a consequence of the need for an adjacent Al-O(H)-Si site to achieve Pd exchange; if true, divalent Pd cations would participate in this, while monovalent Pd would not; therefore isolated P-HAl sites would presumably be unable to stabilize Pd cations.

To further probe the zeolite acid sites, CO was adsorbed onto both H-form zeolites, formation of weak CO bands and perturbation of zeolite OH bands being observed as shown in Figure 4.4. CO adsorption occurs at both framework Al-O(H)-Si and at EFAl as evidenced by disturbance of the bands at 3606 and 3662 cm^{-1}, respectively, though this effect is much weaker for BEA. CO does not perturb the P-HAl(OH) band appreciably at room temperature, though a weak CO band is observed at approximately 2206 cm^{-1} that has previously been assigned to CO adsorbed at these sites.[120]

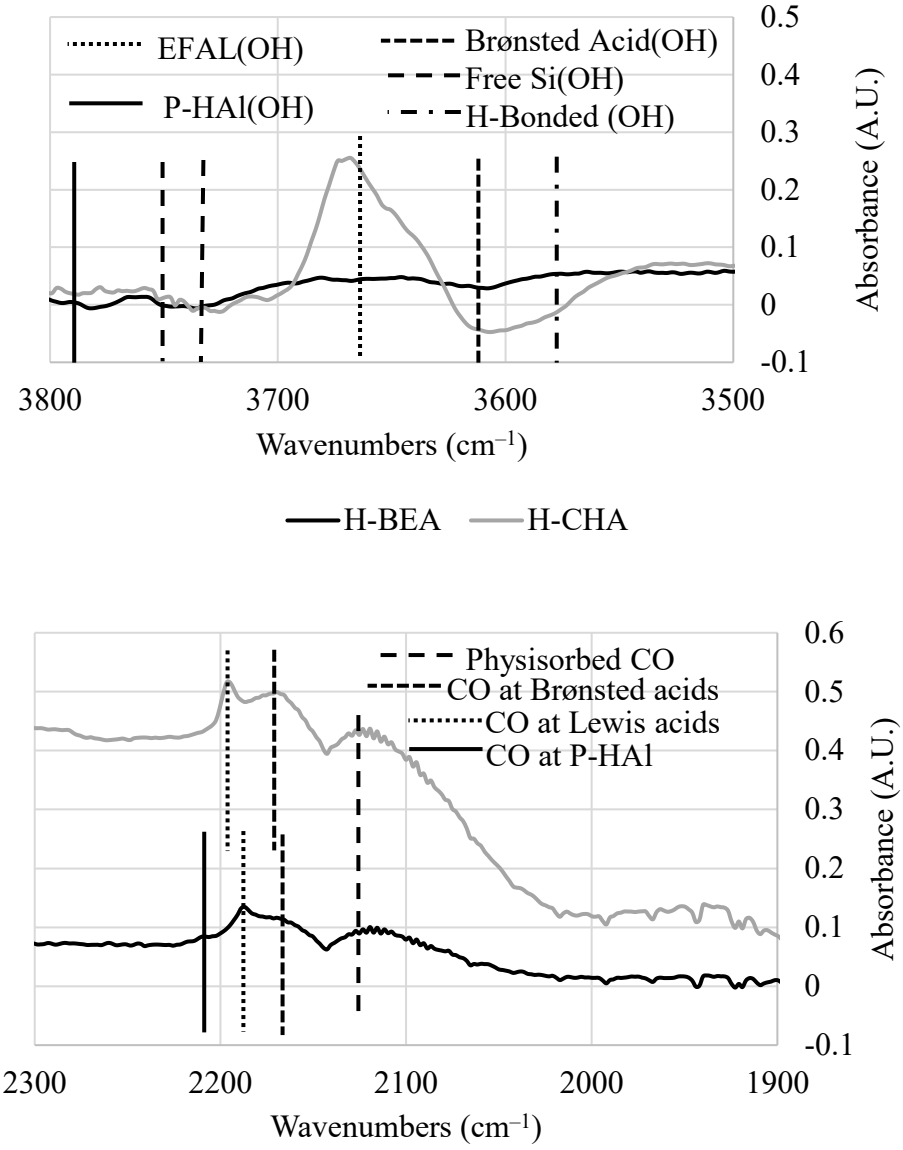

Figure 4.4 DRIFT spectra of the OH (top) and CO (bottom) regions of the H-BEA and H-CHA materials after pretreatment at 500 °C for 1 h with Ar rigorously dried by cold trap. Materials were cooled in dried Ar to 25 °C followed by adsorption of 1000 ppm CO in Ar for 10 minutes.

4.2 NH_3 and CO_2 Adsorption and Treatment on H-BEA

While CO provides examples of the zeolite's behavior in the presence of a weakly basic molecule, the impact of NH_3 is more significant. Pretreatment of H-BEA in NH_3 at 500 °C for 1 h revealed an increase in the intensity of the P-HAl(OH) band and an accompanying increase in the intensity of Si(OH) bands as shown in Figure 4.5. This

suggests that NH_3 is capable of converting Lewis acidic Al present in the framework to P-HAl as described by Bortnovsky et al.[127, 128] To better understand the nature of the interaction of P-HAl with Pd, the behavior of the zeolite framework Al-O and Si-O bands was also examined, these bands representing the IR active bonds present in the zeolite framework. Upon NH_3 treatment, a slight increase in intensity at 890 cm^{-1} is observed, (see Figure 4.5 bottom) this band being previously correlated with the formation of P-HAl sites.[88] A band appearing at 940 cm^{-1} has been observed to increase in intensity upon dealumination (greater abundance of Si-O), while in this case it decreases in intensity, suggesting loss of Si-O(H)-Al in favor of P-HAl.[120] Furthermore, the band at 940 cm^{-1} diverges into two distinct features upon Pd loading (902 and 952 cm^{-1}), though no corresponding decrease in the band at 890 cm^{-1} is observed. The behavior of the band at 890 cm^{-1} is therefore consistent with the continued presence of a similar amount of P-HAl before and after exchange with Pd, indicating that the loss of intensity in the OH region is the result of a direct interaction with Pd, rather than the leaching of these sites by acid during Pd impregnation.

Adsorption of NH_3 on H-BEA is also revealing, both zeolite OH and framework stretches being quenched by NH_3 adsorption as evidenced by their decrease in intensity during adsorption as shown in Figure 4.6. The band at 940 cm^{-1} remains after adsorption, an expected result that shows many of the framework Si species are non-acidic. Both the framework and OH bands associated with P-HAl are eliminated during adsorption, suggesting that basic NH_3 interacts strongly with this site. This supposition is further confirmed by the fact that recovery of this band does not fully occur until 440 °C upon NH_3-TPD (not shown). Formation of NH_4^+ at Brønsted acid sites was observed, a band corresponding to these species appearing at 1490 cm^{-1} (Figure S2). [88, 129]

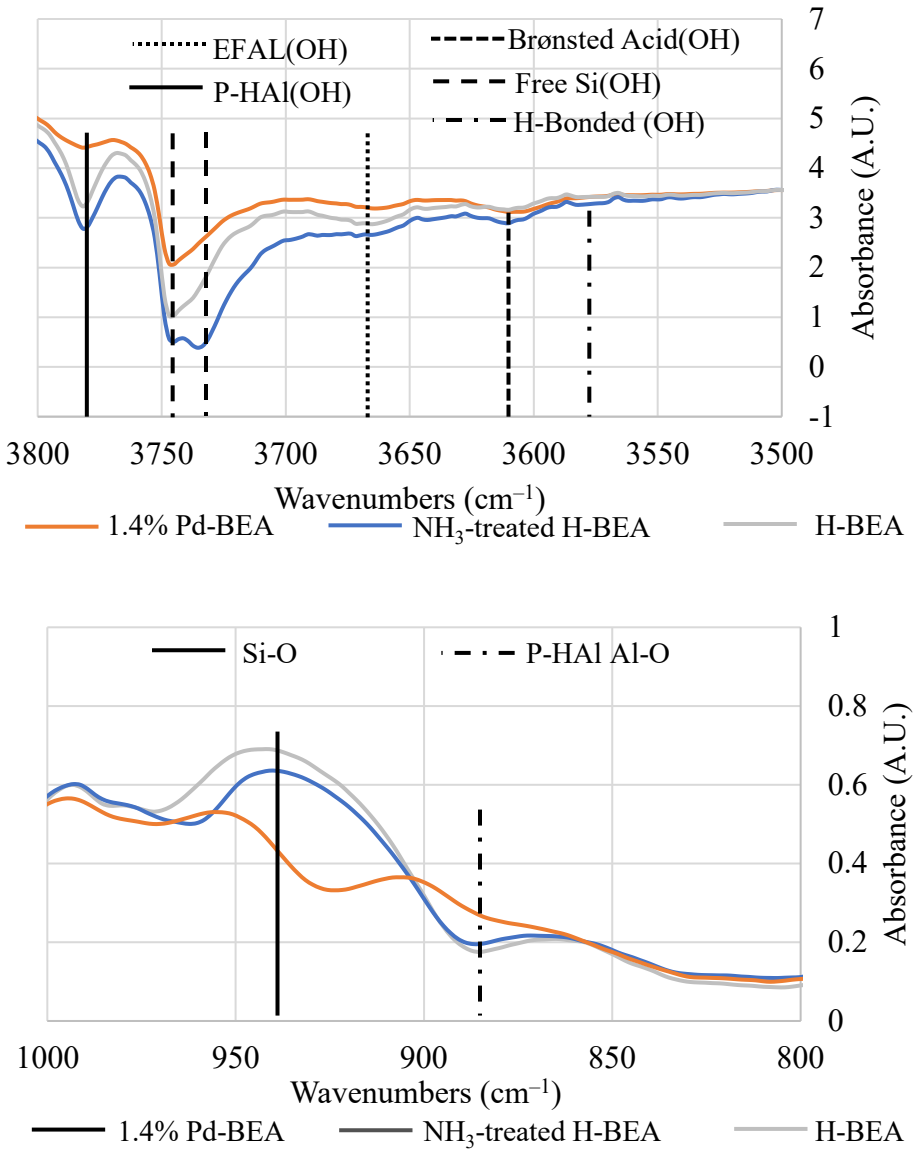

Figure 4.5 DRIFT spectra of the OH (top) and framework (bottom) regions of the BEA materials after pretreatment at 500 °C for 1 h with Ar rigorously dried by cold trap or 1% NH_3 in Ar. The materials were cooled to 25 °C prior to the collection of spectra.

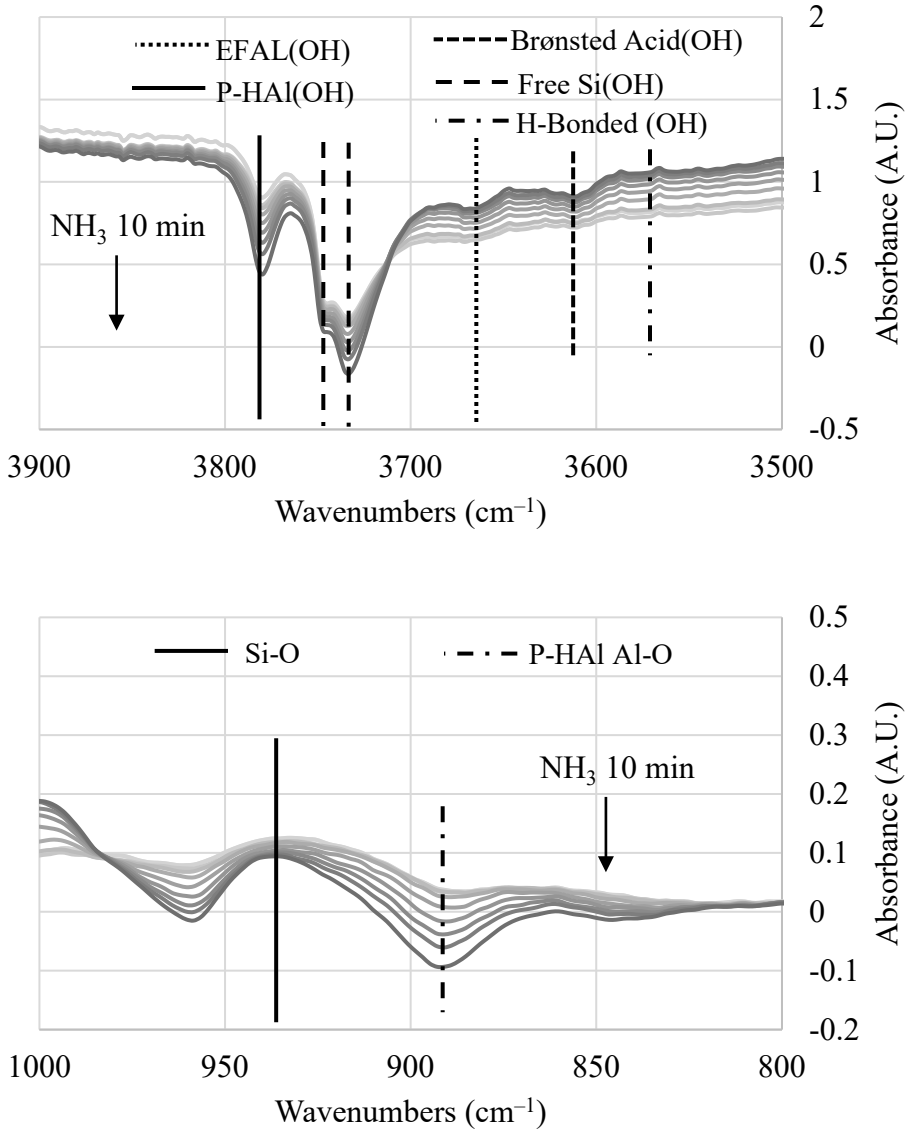

Figure 4.6 DRIFT spectra of the OH (top) and framework (bottom) regions of H-BEA after pretreatment at 500 °C for 1 h with Ar rigorously dried by cold trap. The materials were cooled to 25 °C prior to adsorption of 1% NH_3 in Ar for 10 min, spectra being collected every 1 min.

Interaction of H-BEA with a Lewis acidic molecule, namely CO_2, was also examined. Shown in Figure 4.7, treatment of H-BEA in 1% CO_2 in Ar at 500 °C for 1 h leads to a decrease in the intensity of the P-HAl(OH) band, suggesting a decrease in the abundance of these sites over the H-form material, an indication that this site is a strong enough Lewis acid that more weakly Lewis acidic species such as CO_2 can react as Lewis bases with this site. The results from the framework region are less easily interpreted; however, a shift in the relative intensities of Si(OH) bands is observed with a corresponding shift in the maximum of the framework Si-O band at 940 cm^{-1} to 935 cm^{-1}, this leading to a convoluting influence in the region of the 890 cm^{-1} band that produces an apparent increase in intensity of this species. CO_2 adsorption does show a limited interaction with the P-HAl sites as evidenced in Figure 4.8, EFAL and Brønsted acid OH bands increasing in intensity during adsorption (suggesting elimination of trace water), while the P-HAl(OH) band acts uniquely in becoming less intense with CO_2 adsorption, again indicating that CO_2 interacts with this site as it quenches the OH band.

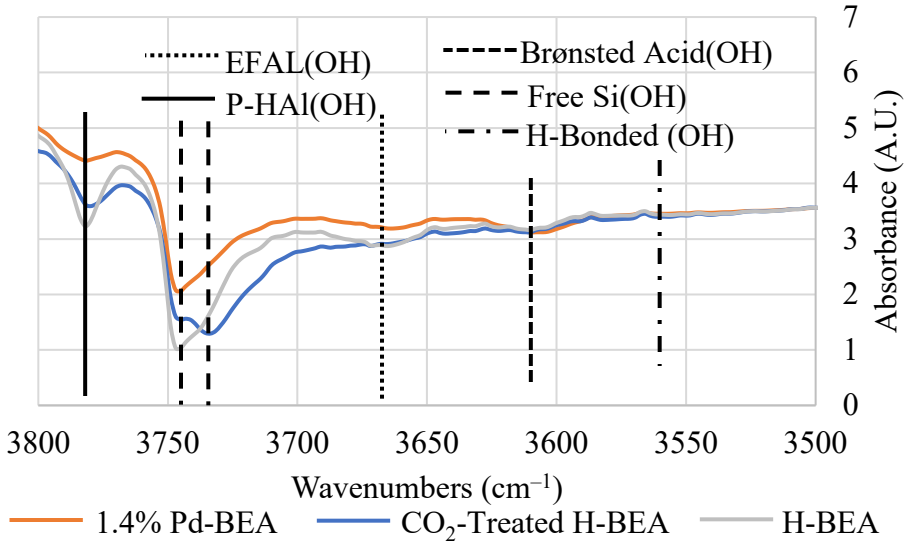

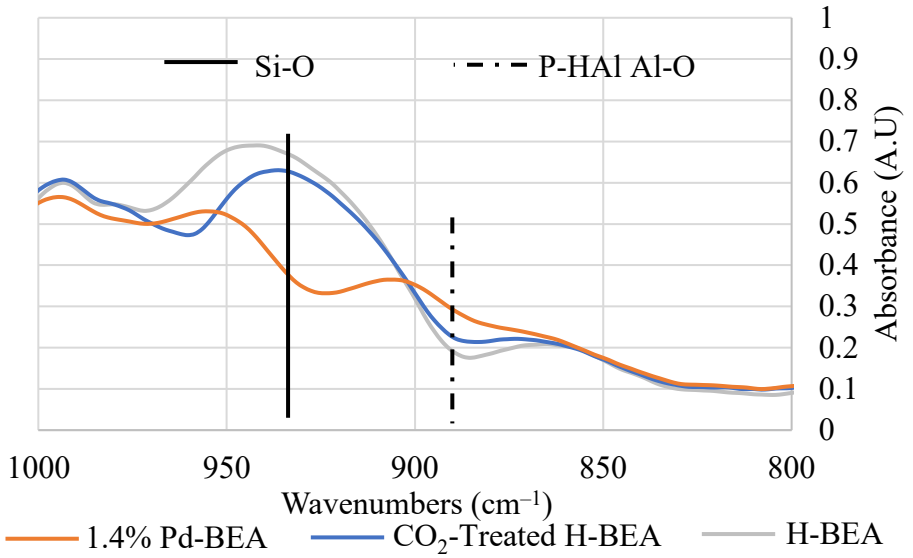

Figure 4.7 DRIFT spectra of the OH (top) and framework (bottom) regions of H-BEA after pretreatment at 500 °C for 1 h with Ar rigorously dried by cold trap or 1% CO_2 in Ar. The materials were cooled to 25 °C prior to the collection of spectra.

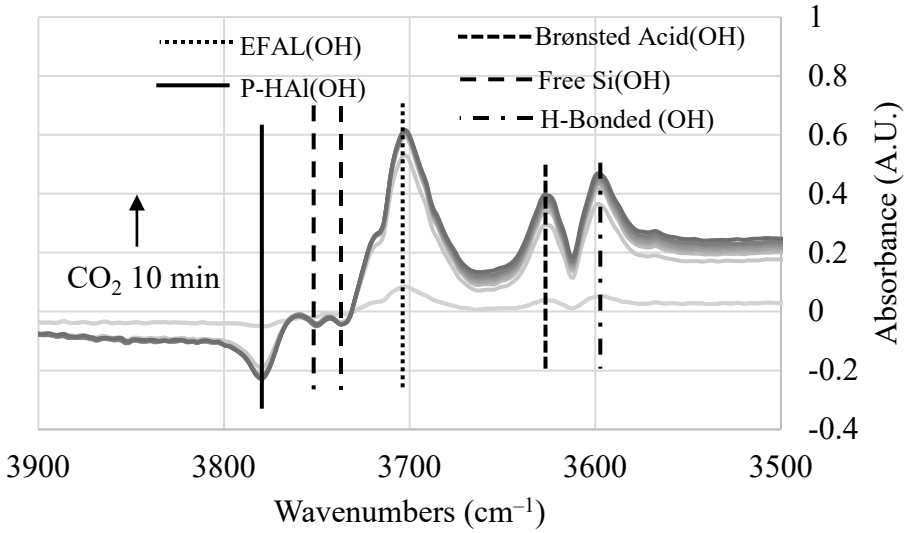

Figure 4.8 DRIFT spectra of the OH region of H-BEA after pretreatment at 500 °C for 1 h with Ar rigorously dried by cold trap. The material was cooled to 25 °C prior to adsorption of 1% CO_2 in Ar for 10 min, spectra being collected every 1 min.

Figure S3 shows the formation of a weak bicarbonate feature at 1665 cm^{-1} during CO_2 adsorption, additional evidence that the interaction of these species is the result of a Lewis acid-base reaction with CO_2 acting as the base.[130] Therefore, it can be suggested in this case that P-HAl sites are removed by acidic treatment both in solution and in the gas phase at 500 °C, however, as Bisio et al. suggest, this effect is limited when incipient wetness impregnation is employed to deposit Pd. Thus, the effect of acidic species during Pd-loading cannot adequately explain the loss of intensity of this feature, the minimum intensity of the P-HAl(OH) band still being observed on 1.4% Pd-BEA. Given the broad reactivity of P-HAl, its role in NO_x adsorption must be more thoroughly explored, especially considering its abundance on BEA.

To summarize the results presented in this section, a more complete examination of the behavior of the zeolite OH-bands with Pd loading was performed, most prominently showing a possible interaction of Pd with P-HAl. Several explanations have been proposed for this behavior, including acid leaching during Pd impregnation, in addition to being a possible result of global changes in the zeolite acidity.[88, 131] To gain

better understanding of the behavior of P-HAl in the presence of acids and bases, CO_2 and NH_3 were employed, respectively. The P-HAl site itself has been shown to be both Brønsted and Lewis acidic, while NH_3 reacts with zeolitic Lewis acid Al sites to form additional P-HAl at high temperatures. This result is supported by the behavior of the framework Si-O and P-HAl-O stretches, the latter showing no loss of intensity upon Pd impregnation, thus suggesting the P-HAl(OH) is indeed interacting with Pd directly rather than being lost to acid leaching. NH_3 adsorption further supports these results, a strong interaction with P-HAl at 25 °C being observed, with concurrent quenching of P-HAl-O and P-HAl(OH) bands. The formation of bicarbonates and NH_4^+ species at these sites is possibly a result of CO_2 and NH_3 acting as Lewis bases at the strongly Lewis acidic P-HAl site.

4.3 NO/NO_2-DRIFTS

The adsorption behavior of NO and NO_2 on zeolites is more consistently described in the literature than that of CO, though some debate remains about the identity of the Pd^{n+}(NO) bands.[59, 90] Assignment of observed species is therefore an easier task than for the CO spectra, though the precise zeolite sites at which the adsorbates reside is still somewhat ambiguous. To further the understanding of the NO_x adsorption behavior of these materials, adsorption of NO and NO_2 onto both the H-form materials was conducted. To deconvolute the behaviors of NO and NO_2, the NO feed gas was passed through a cold trap, serving to condense both water and NO_2. Unfortunately, trace water and NO cannot be removed from the NO_2 feed gas, though association of bands with their respective adsorption sites is still possible.

Figure 4.9 shows adsorption of NO and NO_2 onto both H-form materials at 50 °C, OH and NO stretching regions being displayed. Several NO stretches are observed, specifically NO^+ bands in the range 2100 to 2200 cm^{-1}, while a NO associated feature is observed at ~1870 cm^{-1} on both materials and under adsorption of both gases. Only the H-BEA material under exposure to NO_2 reveals the presence of abundant nitrate-like species, these bands occurring in the range 1580-1650 cm^{-1}, though an extremely weak feature does appear on H-CHA at 1625 cm^{-1} corresponding to molecularly adsorbed NO_2.

The OH region can aid in identifying the zeolite sites that these species occupy through the perturbation of OH species. NO adsorption is shown to result in perturbation of EFAl(OH) bands on both materials, in addition to the Brønsted acid OH bands, indicating that molecularly adsorbed NO and NO^+ can be attributed to adsorption of these species at EFAl and Brønsted acid sites, respectively, though some NO^+ may also reside at EFAl sites.[59] Finally, adsorption of NO_2 on the H-BEA material results in a sharp decrease in the P-HAl(OH) band, indicating this is the primary adsorption site for NO_2 and is also likely responsible for the formation of nitrates. Time-resolved correlation of nitrate formation and P-HAl(OH) disappearance is observed, this being discussed in section 5.4. Interaction of EFAl with NO_2 is also indicated, though trace NO present in the NO_2 feed makes deconvolution of the effects of these two species impossible in this instance. Conversely, NO adsorption leads to no such decrease in intensity of the P-HAl(OH) band, suggesting that NO does not interact with this site to any great extent. Further evidence that P-HAl is the primary adsorption site of NO_2 is the near-absence of both P-HAl(OH) bands and nitrate bands on the H-CHA material, suggesting that the interaction of NO_x with EFAL can be explained by NO adsorption rather than NO_2 adsorption.

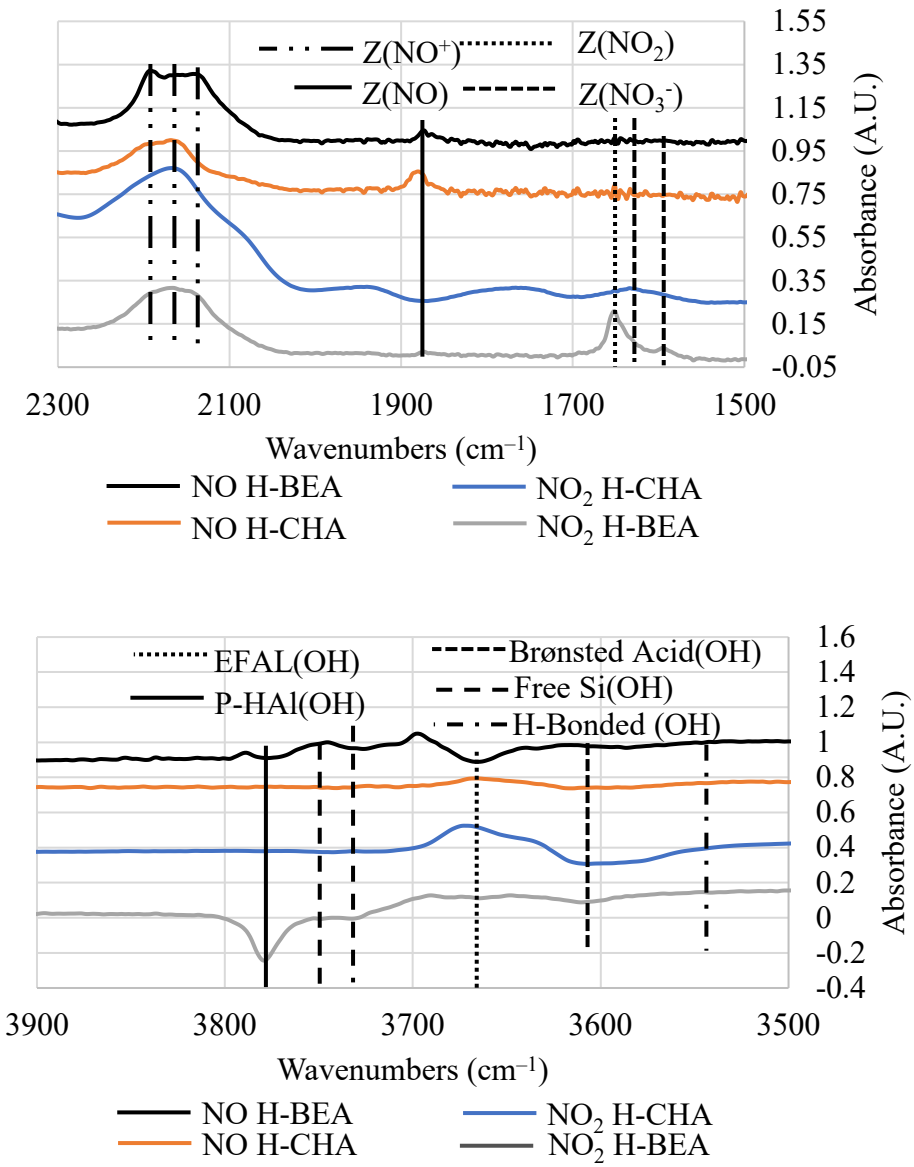

Figure 4.9 DRIFT spectra of the NO (top) and OH (bottom) regions of the H-BEA and H-CHA materials after pretreatment at 500 °C for 1 h with Ar rigorously dried by cold trap. Materials were cooled in dried Ar to 50 °C followed by adsorption of 1000 ppm NO or NO_2 in Ar for 10 minutes.

The role of P-HAl in NO_x storage can be further explored by examining the effect of Pd loading on NO_2 adsorption, these results being presented in Figure 4.10. NO^+ formation is greatly enhanced on the Pd-BEA materials, as evidenced by an increase in the intensity of these bands relative to the nitrate features, this previously being tied to enhancement of low-temperature NO_x desorption in TPD studies.[59, 91] Pd-nitrosyl bands

also appear, nearly equal abundances of Pd^{+} and Pd^{2+} being observed for the BEA material (presuming these species have similar extinction coefficients) though there is a slight preference for Pd^{+} at low loadings.[74, 91] Pd-CHA shows a more intense and broader Pd^{2+}(NO) band than observed on Pd-BEA, an indication that a greater variety of Pd^{2+} species participate in NO adsorption on CHA. Examination of the OH region reveals a similar trend in the intensity of the P-HAl(OH) band to that observed in the spectra of the dehydrated materials, the H-form again showing the greatest abundance of P-HAl. A complete listing of bands resulting from NO and NO_2 adsorption are shown in Table 4.2 for reference.

Table 4.2 NO and NO_2 FT-IR band assignments for BEA and CHA

Band (cm^{-1}) (BEA/CHA)	Assignment	Position	References
1589	Bidentate NO_3^-	P-HAl	[89, 92]
1625	Bridging NO_3^-	P-HAl	[89, 92]
1654	Z(NO_2)	P-HAl	[89, 92]
1832/1804	Pd^{+}(NO)	Isolated Al	[74, 91]
1872/1853	Pd^{2+}(NO)	Paired Al	[74, 91]
1870	Z(NO)	Brønsted Acid/EFAl	[89, 92]
2140/2165 2171/2190	$Z(NO)^{+}$	Brønsted Acid/EFAl	[89, 92]

To provide further support to these results, NH_3 and NO_2 were adsorbed sequentially at 50 °C on H-BEA, the interaction between NH_3 and P-HAl presumably being stronger than NO_2 due to the more favorable acid-base properties of that interaction. These results are presented in Figure 4.11 and show that after NH_3 adsorption the formation of nitrates on H-BEA is prevented. Formation of NO^{+} is apparently also inhibited, while the molecularly adsorbed NO feature at ~1870 cm^{-1} does appear. Concurrently, little perturbation of the P-HAl(OH) band is observed, while interaction of

NO_2 with EFAl and Brønsted acid sites is observed to a greater degree after NH_3 adsorption than when NO_2 is adsorbed alone.

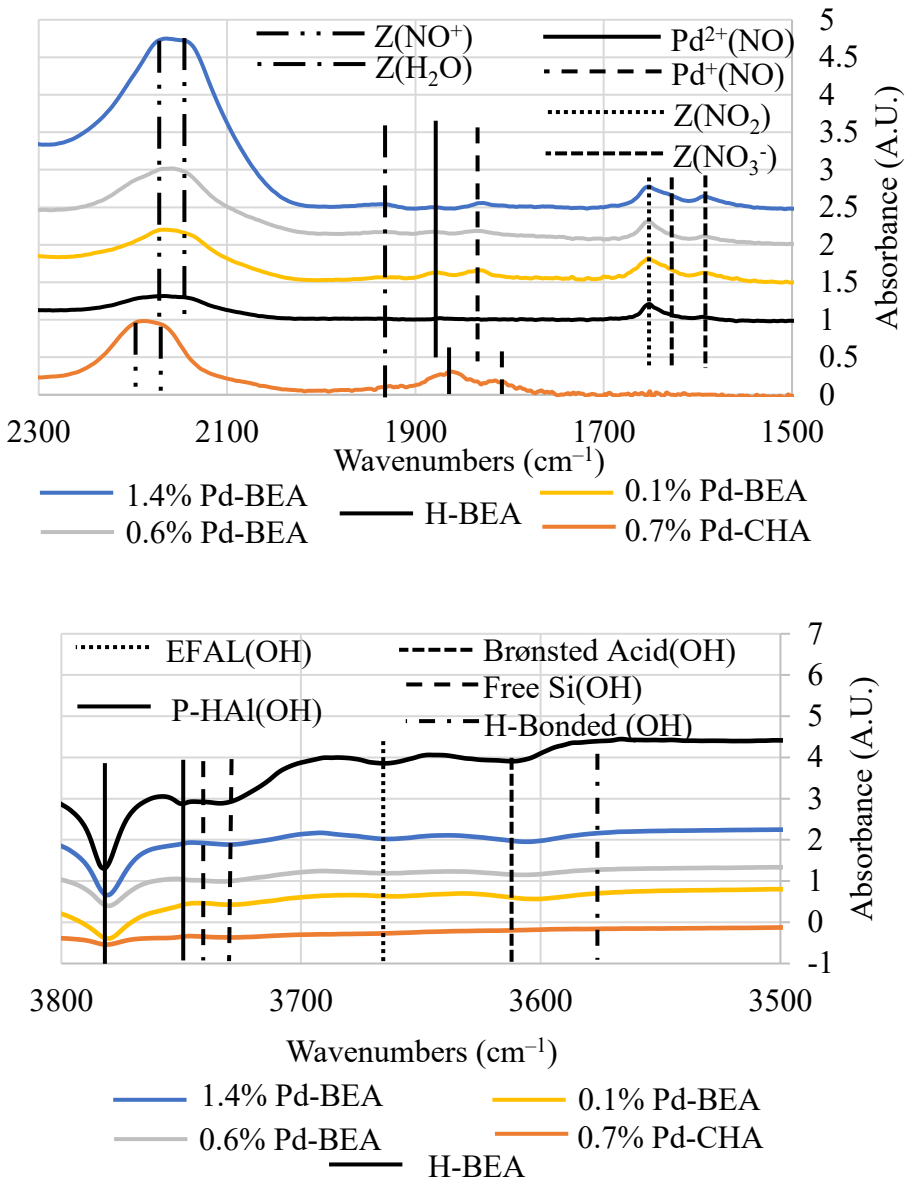

Figure 4.10 DRIFT spectra of the NO stretching regions of the 0.7 % Pd-CHA, 0.1, 0.6, and 1.4% Pd-BEA materials after pretreatment at 500 °C for 1 h with Ar rigorously dried by cold trap. Materials were cooled in dried Ar to 50 °C followed by adsorption of 1000 ppm NO_2 in Ar for 10 minutes.

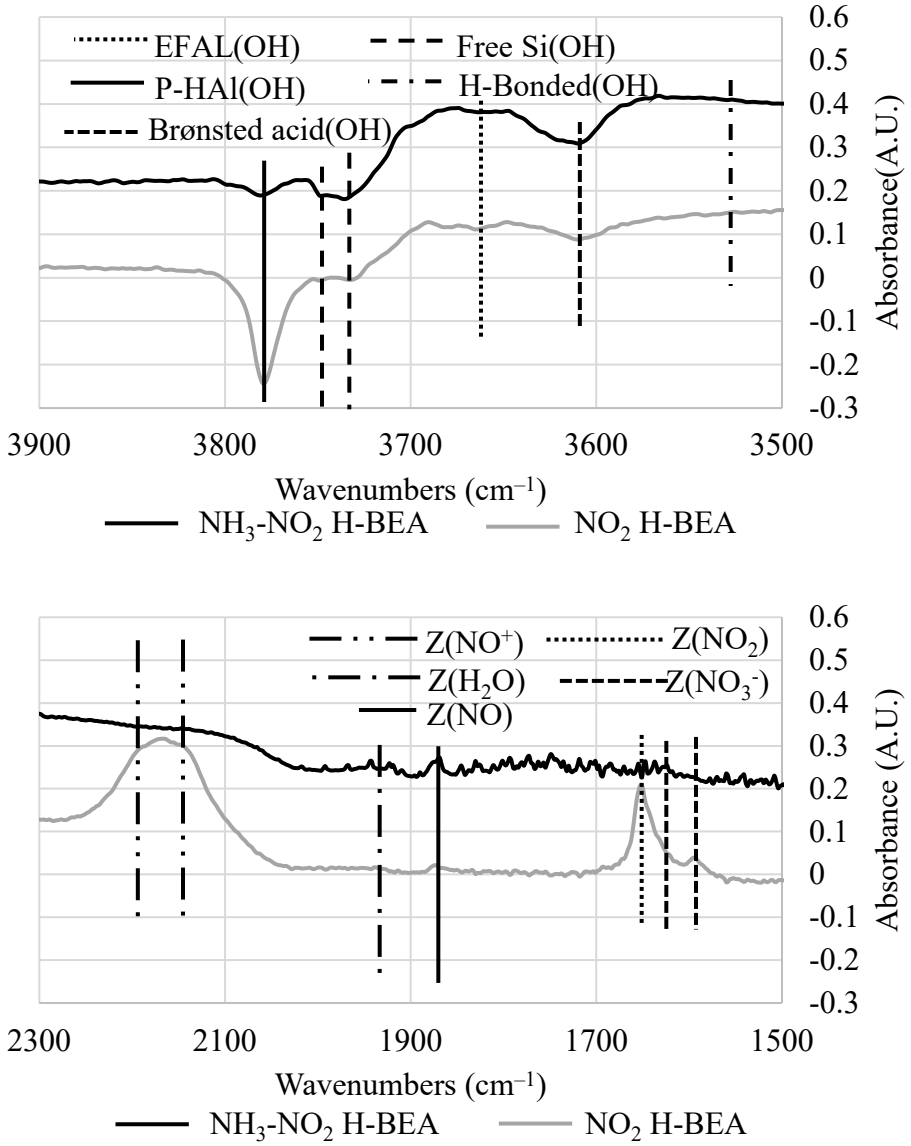

Figure 4.11 DRIFT spectra of the NO stretching regions of the H-BEA material after pretreatment at 500 °C for 1 h with Ar rigorously dried by cold trap. Materials were cooled in dried Ar to 50 °C followed by adsorption of 1000 ppm NO_2 in Ar for 10 minutes, or sequential adsorption of NH_3 for 10 min followed by NO_2 adsorption for 10 min.

To summarize the conclusions of this section, NO and NO_2 adsorption serves to corroborate the results obtained from CO adsorption regarding Pd speciation on BEA at low Pd-loadings, while the interaction of NO_x with P-HAl was examined. P-HAl is found to be associated with the formation of nitrate-like species on both the H- and Pd-form BEA materials, while these species are nearly absent from the CHA materials. NO_2 is

also found to be necessary for the formation of nitrates, while NO is found to form NO^+, $Pd^{n+}(NO)$, and a molecularly adsorbed NO species adsorbed at Brønsted acid, ion-exchanged Pd, and EFAl respectively, the behavior of these bands being corroborated by the behavior of the respective OH features. However, the behavior of NO^+ and the molecularly adsorbed NO cannot be fully deconvoluted and as such these species may reside at EFAl or Brønsted acid sites. Furthermore, NO_2 is found to interact strongly with the P-HAl(OH) band while NO does not behave similarly. Finally, sequential adsorption of NH_3 and NO_2 inhibits the formation of nitrates by blocking P-HAl sites prior to NO_2 adsorption. In the next section, these results will be compared with DRIFTS and microreactor-MS NO_x TPD studies to provide insight into which of the observed NO_x species desorb within the range most suitable for PNA behavior.

4.4 Microreactor NO_x TPD Studies

The basic NO_x adsorption properties of the materials were established by Dr. Yaying Ji, the effect of atmosphere on NO_x adsorption and desorption being shown in Figure 4.12 for 1.4% Pd-BEA, H-BEA, 0.7% Pd-CHA and finally H-CHA. The presence of O_2 during adsorption and desorption is found to enhance NO_x adsorption on both the CHA and BEA materials, while H_2O serves to suppress it. The BEA materials present a complex NO_x desorption profile regardless of adsorption environment. 1.4 % Pd-BEA has three readily discernable desorption events, a low-temperature feature with a maximum at ~135 °C, an intermediate feature with a maximum at ~210 °C and finally a high-temperature feature that has an inconsistent maximum temperature in the range 300–400 °C. H-BEA only possesses a low-temperature feature and an intermediate temperature feature at 100–150 °C and 300 °C respectively.

Overall, the CHA materials are demonstrated to adsorb more NO_x except when water is added to the adsorption gas, BEA showing superior performance under those conditions. H-CHA exhibits only a low-temperature desorption event at 132 °C, while 0.7% Pd-CHA shows the appearance of a desorption feature centered around 220 °C in addition to the low-temperature feature when O_2 is present. However, no increase in desorption temperature is evident in the absence of O_2, only an increase in the intensity of

the low-temperature feature over the H-form material. A high-temperature feature centered at 400 °C also appears on 0.7% Pd-CHA, this species being analogous to that observed on 1.4% Pd-BEA with a maximum above 350 °C. The total quantities of desorbed NO_x from each of these experiments is shown in Figure 4.13, along with the NO/Pd ratio where applicable.

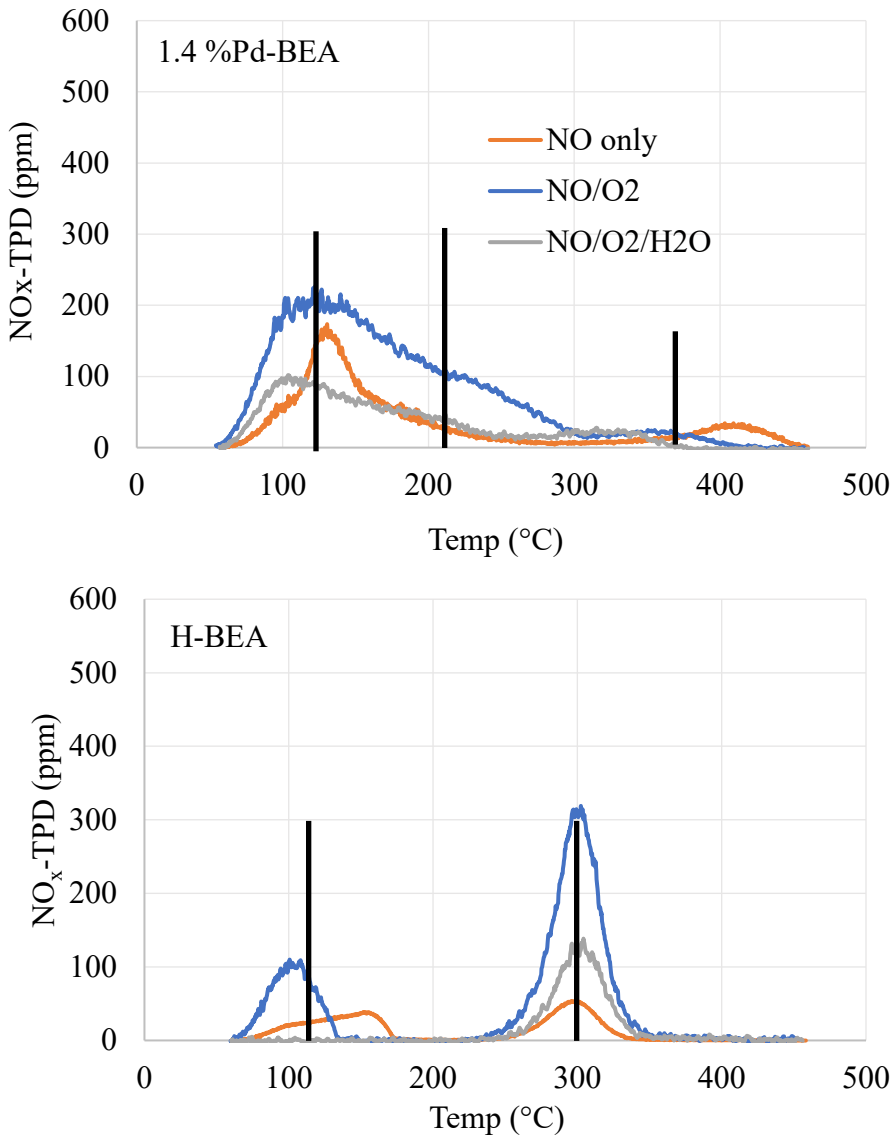

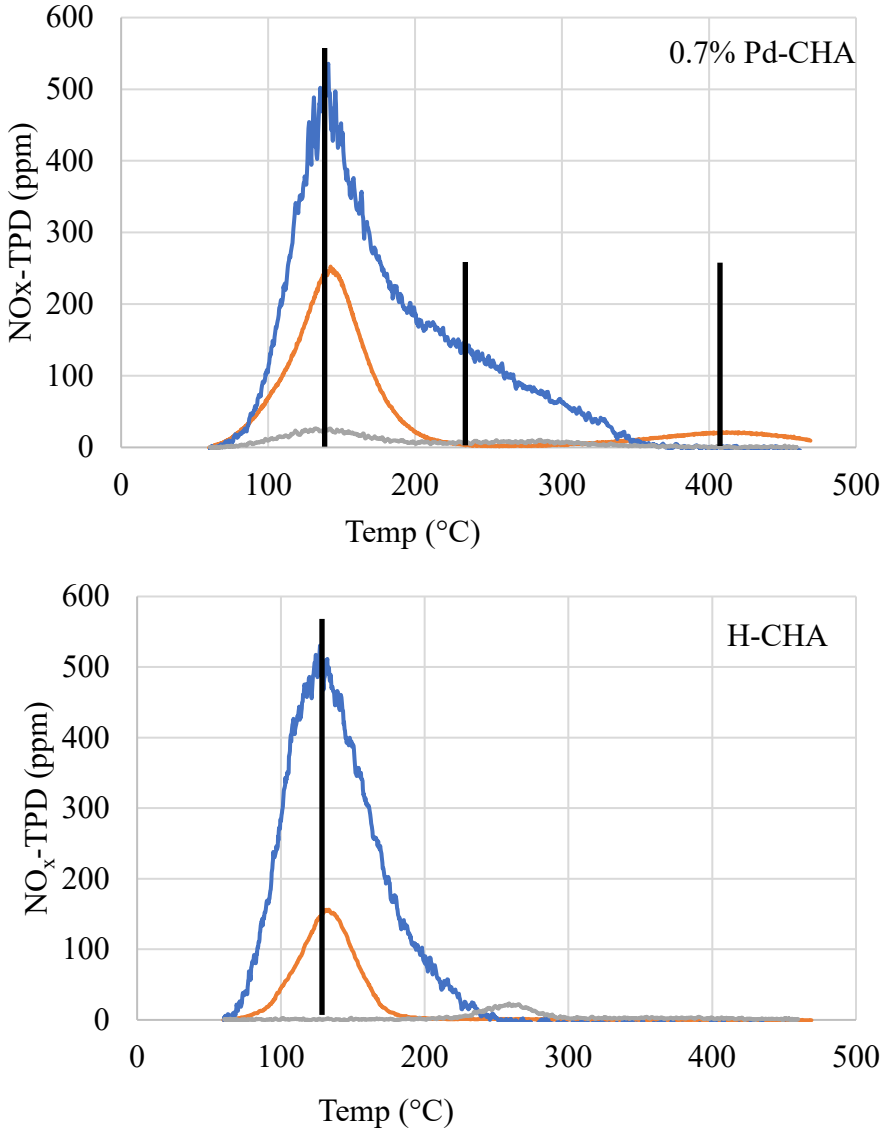

Figure 4.12 1.4% Pd-BEA (top), 0.7% Pd-CHA (bottom). NO_x TPD conducted in microreactor-MS with calibrated NO_x concentrations. Materials were pretreated in 10% O_2 in He for 1 h prior to adsorption. 1000 ppm NO in He, 10% O_2/He, or 1-2% water 10% O_2/He was adsorbed for 10 min at 50 °C followed by a 1 h purge in 10%O_2/He. TPD was carried out in 10% O_2/He at a ramp rate of 10 °C per min.

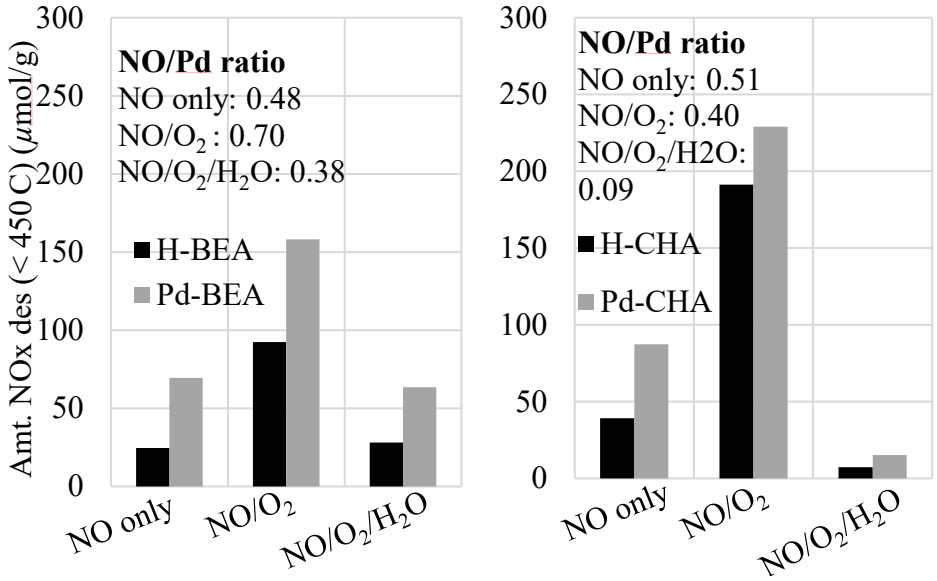

Figure 4.13 NO_x TPD conducted in microreactor-MS with calibrated NOx concentrations. Materials were pretreated in 10% O_2 in He for 1 h prior to adsorption. 1000 ppm NO in He, 10% O_2/He, or 1-2% water 10% O_2/He was adsorbed for 10 min at 50 °C followed by a 1 h purge in 10%O_2/He. TPD was carried out in 10% O_2/He at a ramp rate of 10 °C per min. Tabulated values were calculated from integrated NO_x MS signals.

According to the NO/Pd ratio, Pd utilization on CHA is observed to be lower than on BEA in agreement with the H_2-TPR results that indicate lower Pd dispersion on 0.7% Pd-CHA. Pd-CHA also shows a smaller improvement in NO_x storage capacity over the H-CHA material than the increase observed in comparing the H- and 1.4% Pd-BEA. This is a result of much of the Pd being present as PdO_x on CHA, though as shown above, NO_x storage can be improved after H_2 reduction and re-oxidation. These data also serve to provide a proof of concept for these materials, especially for 1.4 % Pd-BEA, this material trapping a significant amount of NO_x even in the presence of water and desorbing a large portion of this NO_x near or above 200 °C.

Correlation of NO_x desorption events with DRIFTS data will be explored further in the next chapter; meanwhile, additional adsorption parameters were evaluated in the presence of O_2, given the greater NO_x adsorption observed in this atmosphere. The effect of adsorption temperature on NO_x storage capacity of H-BEA and 1.4% Pd-BEA was evaluated, results being presented in Figure 4.14.

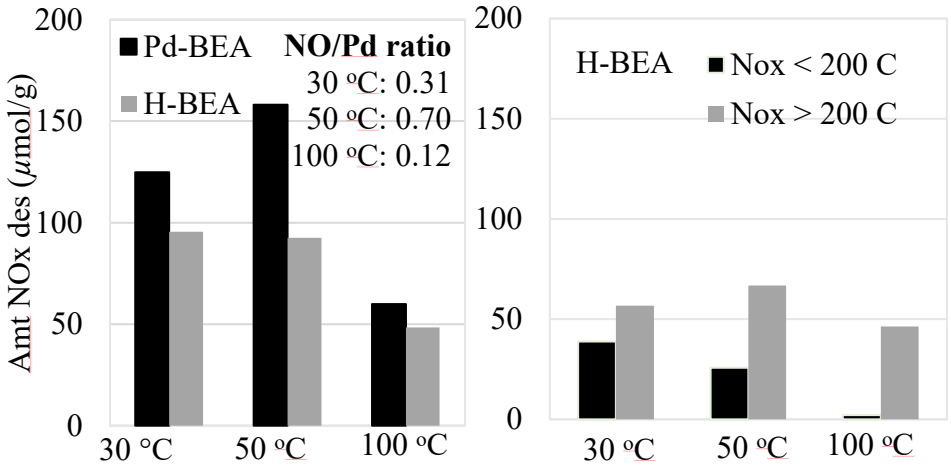

Figure 4.14 NOx TPD conducted in microreactor-MS with calibrated NO_x concentrations Right: total NO_x adsorbed on H and Pd-BEA, left: deconvolution of NO_x storage events on H-BEA. Materials were pretreated in 10% O_2 in He for 1 h prior to adsorption. 1000 ppm NO in 10% O_2/He was adsorbed for 10 min at 30, 50, or 100 °C followed by a 1 h purge in 10%O_2/He. TPD was carried out in 10% O_2/He at a ramp rate of 10 °C per min. Tabulated values were calculated from integrated NO_x MS signals.

NO_x adsorption was shown to be at a maximum near 50 °C, Pd utilization and NO_x storage both being greater than at the other two temperatures tested. Examining the easily separable desorption events of H-BEA shows that the high-temperature desorption event is maximized at 50 °C, while the desorption below 200 °C decreases in intensity as temperature increases. This is highly desirable: when adsorbed at 50 °C, most NO_x desorbs above 200 °C, the minimum temperature for the downstream catalyst to become active. The effect of Pd-loading on the NO_x storage capacity of BEA was also examined, the results being shown in Figure 4.15. Generally, as Pd-loading increases, the total quantity of NO_x adsorbed also increases, while 1% Pd-Si-BEA shows negligible NO_x adsorption under these conditions, indicating that PdO_x fails to store NO_x. Notably, the rate of NO_x adsorption was found to be relatively constant for the first two minutes of adsorption regardless of the material tested, a value of ~43 μmol/(g*min) being determined (not shown). Given the above data, a NO_x concentration of 1000 ppm and an adsorption temperature of 50 °C was chosen for all NO_x-DRIFTS experiments unless otherwise indicated.

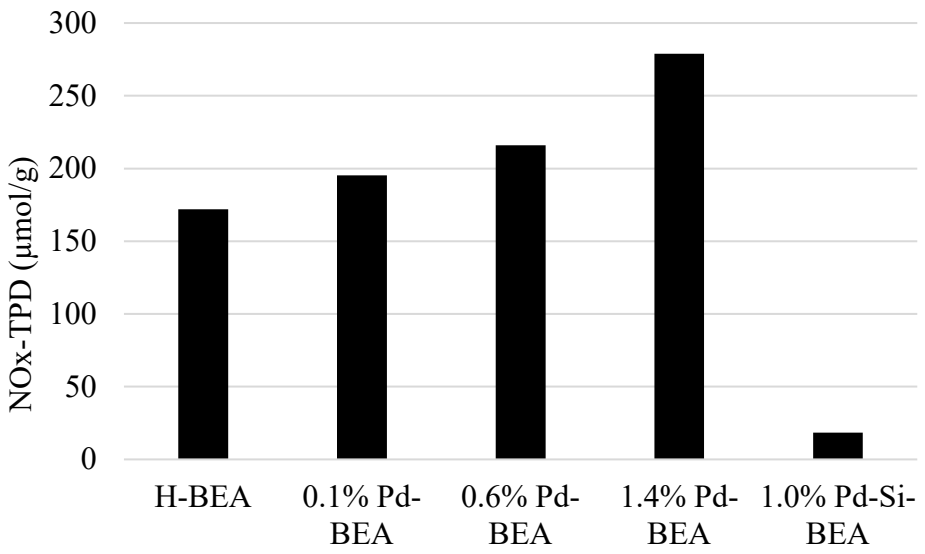

Figure 4.15 NO_x TPD conducted in microreactor-MS with calibrated NO_x concentrations. Materials were pretreated in 10% O_2 in He for 1 h prior to adsorption. 1000 ppm NO in 10% O_2/He was adsorbed for 10 min at 50 °C followed by a 1 h purge in 10%O_2/He. TPD was carried out in 10% O_2/He at a ramp rate of 10 °C per min. Tabulated values were calculated from integrated NO_x MS signals.

4.5 Conclusions

This chapter focused on the role of P-HAl in both Pd-siting and in NO_x adsorption, examination of these behaviors being evaluated by in-situ DRIFTS. Increased Pd-loading leads to a reduction in intensity of the P-HAl(OH) band, this behavior being proposed to be a result of interaction with Pd due to the absence of a corresponding decrease in the P-HAl-O vibration as observed upon acid leaching of this species. The behavior of the zeolite OH bands and their corresponding framework vibrations were explored under treatment in both acidic (CO_2) and basic (NH_3) gases. Treatment in NH_3 led to an increase in the intensities of the P-HAl(OH) and P-HAl-O bands, suggesting formation of additional P-HAl, while treatment in CO_2 led to a decrease in the intensity of the P-HAl(OH) band, suggesting a reduced abundance of these sites after treatment. Both species are shown to quench the P-HAl(OH) stretch upon adsorption at room temperature suggesting adsorption at this site, most probably with CO_2 and NH_3 acting as Lewis bases, a supposition supported by the formation of bicarbonate and NH_4^+.

NO and NO_2 adsorption were also performed on both zeolite materials, emphasis being placed on the differing behaviors of the H-form and Pd-loaded zeolites. Nitrate species are observed only when NO_2 is adsorbed on the BEA materials, quenching of the P-HAl(OH) band occurring simultaneously. The absence of P-HAl on the CHA materials is accompanied by an absence of nitrate features. Meanwhile, NO adsorption at EFAL is proposed to result in a stretch at ~1870 cm^{-1} on both materials, a corresponding OH perturbation again being observed. To further confirm the association of nitrates and P-HAl, NH_3-NO_2 sequential adsorption was performed on H-BEA, the results showing an absence of nitrate bands upon NO_2 adsorption when P-HAl sites have been previously saturated by NH_3. Finally, the basic NO_x desorption behaviors are described, 1.4 % Pd-BEA showing the highest NO_x adsorption capacity at 50 °C under realistic conditions where water is present. Conversely, the CHA materials show better NO_x storage capacity than BEA when water is absent, the presence of O_2 improving capacity in either case. These data serve as a proof of concept for these materials, as 1.4% Pd-BEA exhibits significant NO_x storage capacity at near-ambient temperatures in the presence of water, while also desorbing most of the adsorbed NO_x within the desired temperature range.

CHAPTER 5. ROLE OF Pd SPECIATION IN NO_X STORAGE

The final chapter of this work focuses on the correlation of DRIFTS and microreactor-MS data along with a further exploration of the formation of NO_2, and an examination of the reactivity of NO and NO_2 with Pd. This work will again primarily focus on the BEA materials due to their better performance during NO_x adsorption in the presence of water, and due to the weaker interaction of NO_2 with CHA, observed by the near-absence of nitrate formation on this material. Special consideration will again be paid to the deconvolution of the effects of NO and NO_2, this being a key area of investigation identified by Gu et al. in a recent review of PNA chemistry.[59] The correlation of microreactor NO_x desorption events with adsorbate species identified by in-situ DRIFTS and their respective adsorption sites will provide data invaluable to the rational design of PNA materials, as the most desirable adsorption sites and adsorbate species can be identified and selected for the development of future materials. Some microreactor experiments performed for this chapter were conducted by Dr. Yaying Ji as part of her work to define the NO_x adsorption and desorption behaviors of these materials in the early stages of this project, these data being included in Figures 5.1, 5.2 and 5.5.

5.1 Effect of Atmosphere and Pd-loading on NO_x Desorption

5.1.1 Microreactor-MS NO_x-TPD

NO_x-TPD of the Pd-BEA materials was conducted in both inert conditions and in the presence of O_2, these data being shown in Figure 5.1. The overall quantities of NO_x stored on each of the materials is similar whether O_2 is present or not, except in the case of H-BEA, which reveals a substantial increase in NO_x storage capacity in the presence of O_2. However, the desorption profiles of the materials are greatly dissimilar in the differing atmospheres. The effect of O_2 was also explored by CO-DRIFTS, results showing that when oxygen is present during pretreatment the majority of the Pd present can be inferred to be in the divalent state (Section 2.2.2), while some Pd^{2+} species present on BEA are shown to not participate in NO_x adsorption (Section 3.2.3), these results being especially relevant to the following discussion. During NO_x adsorption and

desorption in the presence of O_2, the materials present four differentiable NO_x desorption events at 100, 150, 300, and finally 400–500 °C. Given the gradual disappearance of the desorption feature at 300 °C as Pd-loading increases, and the presence of this feature on H-BEA, it can be inferred that this desorption event is associated with the decomposition of nitrates adsorbed at P-HAl. This desorption event is fully extinguished at 1.4% Pd-loading, further emphasizing the interaction of Pd with P-HAl, the presence of Pd apparently serving to reduce the desorption temperature of nitrate-like species into a more favorable range (~300 to ~200 °C), this behavior being correlated with the decreasing intensity of the P-HAl(OH) FT-IR band as Pd-loading increases. The features at ~150 °C and 350–450 °C can be associated with the addition of Pd, as neither of these features appears on the H-form material regardless of atmosphere.

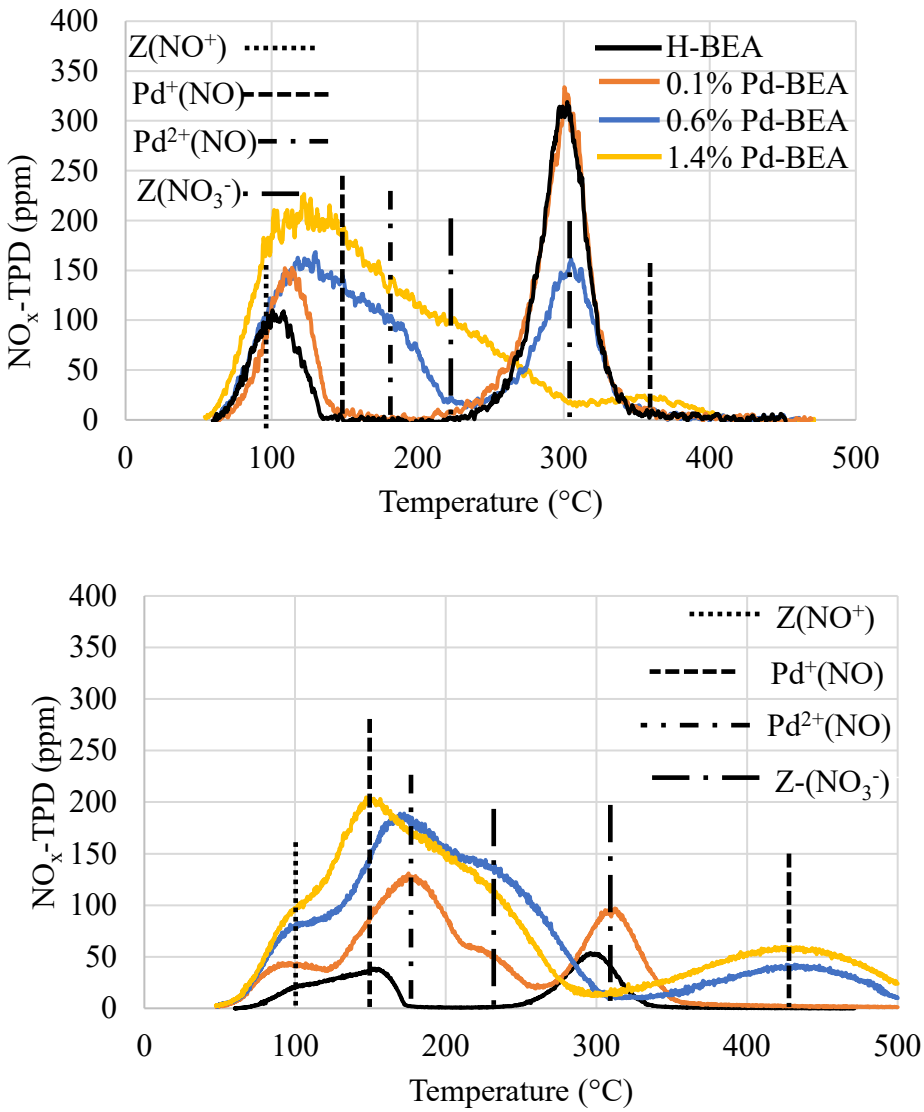

Figure 5.1 NOx TPD conducted in microreactor-MS with calibrated NO_x concentrations. Materials were pretreated in 10% O_2 in He or He for 1 h prior to adsorption. 1000 ppm NO in 10% O_2/He or He was adsorbed for 10 min at 50 °C followed by a 1 h purge in 10% O_2/He or He. TPD was carried out in 10% O_2/He or He at a ramp rate of 10 °C per min. O_2 was either included (top) or excluded (bottom) during all steps.

NO_x-TPD performed after NO storage in the absence of O_2 is also informative. The desorption event at 300 °C increases in intensity from H-BEA to 0.1% Pd-BEA under these conditions, an indication that additional NO_2 (then stored as nitrates) is formed under inert conditions either as a result of the reduction of Pd^{2+}(OH) to Pd^{+} by NO as described by Descorme et al., or by reaction of NO with PdO_x to form Pd^0.[90] This feature

is extinguished at a loading of 0.6% under these conditions, suggesting nitrate desorption is influenced by Pd at lower loadings under inert conditions as this desorption event isn't fully extinguished until 1.4% Pd when O_2 is present. This also explains the lack of effect on this desorption event at 0.1% Pd in the presence of O_2, formation of additional NO_2 upon addition of Pd outweighing the shift of nitrates that interact with Pd to lower desorption temperatures. The low-and intermediate- temperature desorption features are more complex under inert conditions, a new desorption maximum appearing at ~150–170 °C. This feature, as well as the desorption events at 100 and 200 °C, all increase in intensity with Pd-loading. The highest temperature desorption event (450 °C) appears at a Pd-loading of 0.6% and is still more intense at a loading of 1.4%. In either atmosphere, this feature appears simultaneously with the full disappearance of the event at 300 °C, with the 450 °C species evidently being strongly favored under inert conditions. That conclusion favors assignment of this desorption event as $Pd^+(NO)$, Pd^+ also being proposed to be more abundant on the Pd-BEA materials under inert treatment as described by CO-DRIFTS.

To further clarify the above results, it is necessary to deconvolute the effects of O_2 during NO_x adsorption and NO_x desorption, especially regarding the role of NO_2 during each step of the process. NO_x-TPD was therefore performed on 1.4% Pd-BEA with O_2 added at various stages of the experiment to assess the impact of O_2 during pretreatment, adsorption, and desorption separately. These results are presented in Figure 5.2, the experiments shown consisting of the full O_2 and full inert data shown above, as well as the material pretreated in O_2 with adsorption and desorption carried out under inert conditions, and an additional experiment where only the adsorption was carried out under inert conditions.

Remarkably, NO_x storage is lowest on the material for which NO was adsorbed in the absence of O_2, while the pretreatment and desorption were carried out in the presence of O_2, the combination of O_2 treatment and inert adsorption being particularly unfavorable due to higher abundance of Pd^{2+} and limited formation of NO_2 under those circumstances. These suppositions are supported by the effect of inert pretreatment, this leading to an increase in the abundance of the high-temperature desorption feature (450

°C) and a decrease in the abundance of the intermediate- temperature desorption features (150-300 °C) relative to the O_2-treated material under identical adsorption and desorption conditions. Further, the overall NO_x storage capacity is shown to be slightly greater on the BEA materials under inert conditions than under oxidizing conditions, the greater intensity of the high-temperature Pd^+(NO) desorption event accounting for much of this additional NO_x storage capacity. This is a further indication that not all the Pd^{2+} species observed in the CO-DRIFTS experiments participate in passive NO_x adsorption, as a substantially greater change in the intermediate temperature NO_x desorption events would be expected from the results of the CO-DRIFTS experiments under air and Ar pretreatment. The presence of O_2 during desorption generally decreases the temperature of all desorption events.

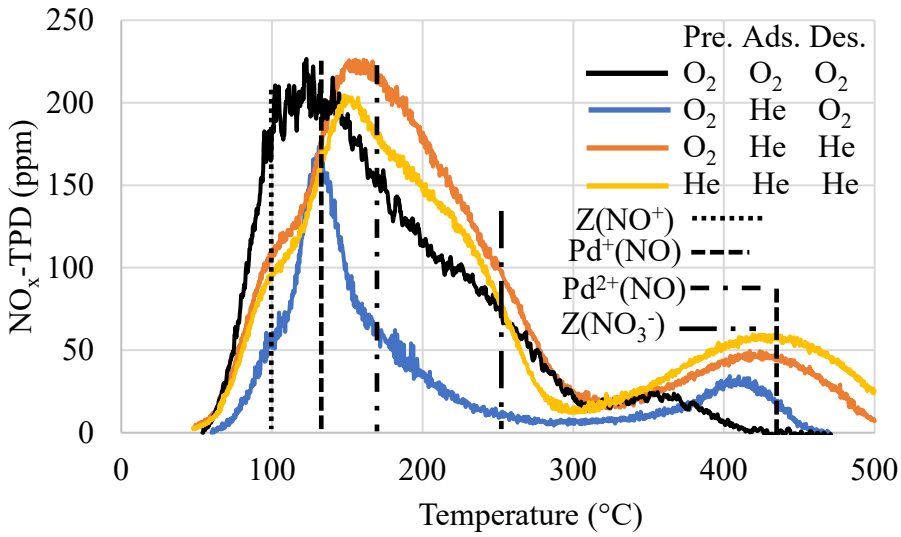

Figure 5.2 NO_x TPD of 1.4% Pd-BEA conducted in microreactor-MS with calibrated NO_x concentrations. Materials were pretreated in 10% O_2 in He or He for 1 h prior to adsorption. 1000 ppm NO in 10% O_2/He or He was adsorbed for 10 min at 50 °C followed by a 1 h purge in 10% O_2/He or He. TPD was carried out in 10% O_2/He or He at a ramp rate of 10 °C per min.

From these data and the corresponding DRIFTS data, presented below, a rough correlation of desorption events and adsorption sites can be made. The lowest-temperature feature observed at 100 °C can be assigned to NO^+ and molecularly adsorbed NO at Brønsted acid sites and EFAl, while the event at 300 °C can be assigned to NO_2

adsorbed at P-HAl sites, both of these desorption events being present on the H-form material and thus associated with zeolite sites. The desorption events at 150 and 250 °C can be assigned to NO adsorbed at Pd^{2+} and NO_2 adsorbed at Pd-influenced P-HAl sites respectively, while the highest-temperature feature can be assigned to NO adsorbed at Pd^{+}. Further, CO-DRIFTS data can be used to infer which Pd^{2+} species are involved, the most abundant Pd^{2+}(CO) bands being those related to $[Pd^{2+}(OH)]^{+}$, these species also observed to be easily reducible to Pd^{+}.

One inconsistency in these data has yet to be resolved, this being the increase in NO_x desorption in the range 150-300 °C during desorption under inert conditions as shown in Figure 5.2. The fact that desorption in this range under inert conditions is also enhanced by pretreatment in O_2 suggests that Pd^{2+} is responsible for this increase, though that cannot fully explain the increase observed for NO_x desorption in O_2, similar amounts of Pd^{2+} theoretically existing in both cases. A possible explanation for this result would therefore be that the presence of O_2 during adsorption helps to maintain Pd in the divalent state, or that an additional desorption feature associated with NO_x adsorbed at Pd^{+} occurs in the range of interest. The enhanced NO_x adsorption under inert conditions would then result from reduction of Pd^{2+} to Pd^{+} during NO_x adsorption, followed by adsorption of an additional NO as described by Descorme et al.[90] This observation also points to the difficulty in interpreting these data, as most of these desorption events overlap to at least some degree and the true number of species present cannot be easily determined.

To summarize the results of this section, the effects of O_2 on NO_x desorption were analyzed, these results being correlated with CO-DRIFTS data to make inferences about the identities of the various NO_x desorption events and also explore the chemistry that occurs during pretreatment, adsorption, and desorption. The presence of O_2 during pretreatment is found to decrease NO_x storage on this material, proposed to result from formation of Pd^{2+} species that do not store NO_x. The presence of O_2 during adsorption is proposed to enhance NO_2 formation, leading to additional storage of NO_x as nitrates while also inhibiting reduction of Pd^{2+}. Finally, the presence of O_2 during the desorption step leads to a general decrease in the desorption temperature of all NO_x species. NO_x desorption event assignments can be resolved from these data, NO^{+} and nitrate desorption

occurring at 100 and 300 °C respectively. Desorption events associated with NO_x adsorbed at Pd^{n+} sites are also proposed at 100-300 °C (Pd^{2+}(NO)), 100-300 °C (Pd^{+}(NO)), 200-300 °C (Pd-P-HAl) and finally 350-450 °C (Pd^{+}(NO)). The observed changes in desorption under various conditions can largely be explained by changes in the NO_2 concentration resulting from the presence of O_2 or through reduction of Pd^{2+} by NO.

5.1.2 In-situ DRIFTS NO_x-TPD

To corroborate the putative NO_x desorption assignments with spectroscopic data, NO_2-TPD experiments were performed on the variously loaded materials, desorption behavior being monitored by in-situ DRIFTS. These experiments were carried out in the absence of O_2 and with NO_2 as the adsorbate to ensure the appearance of nitrate species. Immediately upon increasing the temperature, all species begin to decrease in intensity, suggesting that the desorption events overlap to a great degree as observed in microreactor experiments. However, useful inferences can still be derived from the final temperature at which a given band is observed, these values being tabulated in Table 5.1. Due to the convoluting effects of water pseudo-maxima, the behavior of NO^{+} species is not evaluated here.

Table 5.1 NO_x desorption temperatures from in-situ DRIFTS NO_2-TPD

	Pd^{2+}(NO) (°C) 1876 cm^{-1}	Pd^{+}(NO) (°C) 1833 cm^{-1}	$Z(NO)_2$ (°C) 1650 cm^{-1}	$Z(NO)_3^-$ (°C) 1623 cm^{-1}	$Z(NO)_3^-$ (°C) 1589 cm^{-1}
H-BEA	N/A	N/A	440	160	420
0.1% Pd-BEA	N/A	140	420	160	340
0.6% Pd-BEA	180	220	380	160	300
1.4% Pd-BEA	220	260	380	160	320

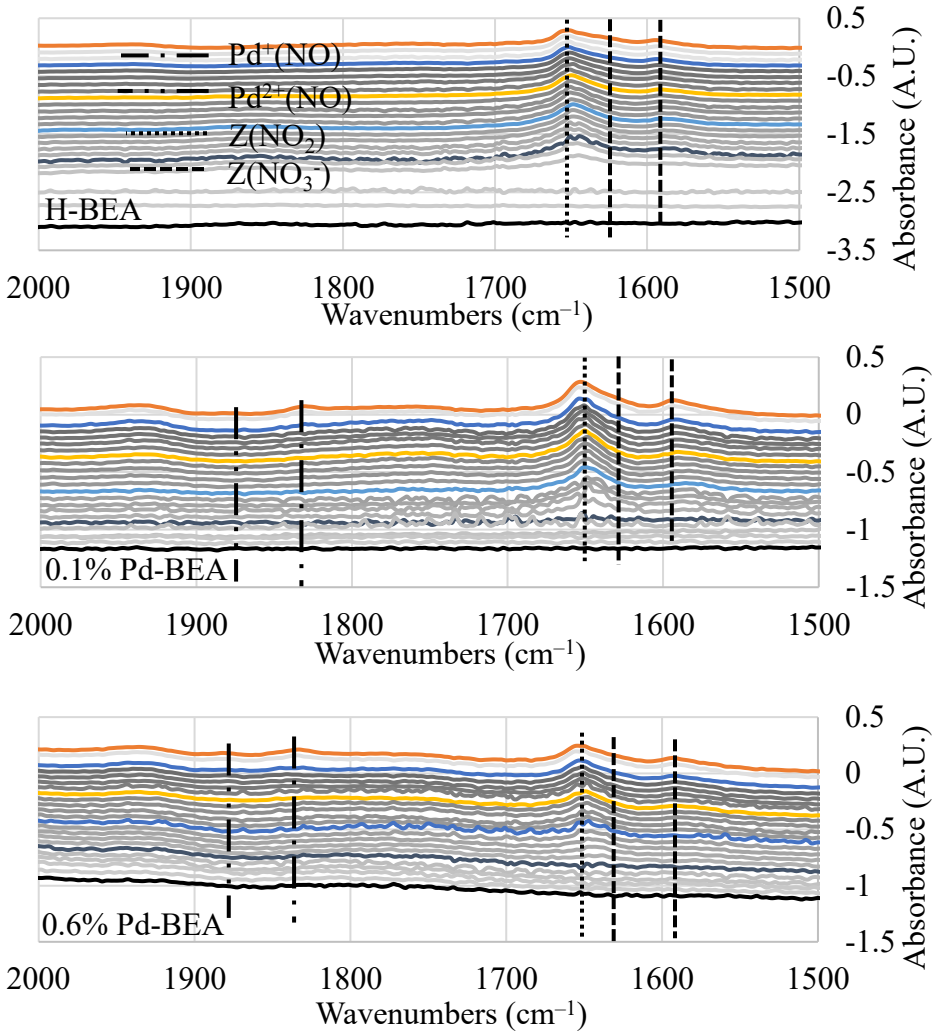
Pd+(NO)
Pd2+(NO)
Z(NO2)
Z(NO3-)
H-BEA
0.1% Pd-BEA
0.6% Pd-BEA
Absorbance (A.U.)
Wavenumbers (cm−1)
2000
1900
1800
1700
1600
1500
0.5
0
-0.5
-1
-1.5
-2.5
-3.5

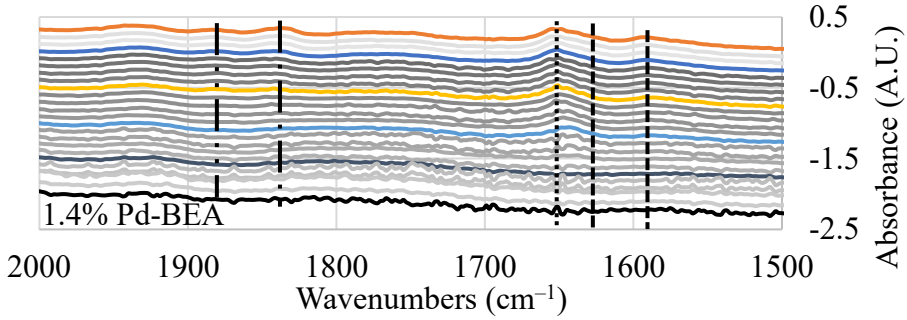

Figure 5.3 H-BEA (top) 0.1% Pd-BEA (second) 0.6% Pd-BEA (third) and 1.4% Pd-BEA (bottom): DRIFTS spectra of NO_2 desorption after pretreatment at 500 °C for 1 h with rigorously dried Ar. NO_2 was adsorbed for 10 minutes at 50 °C before the material was purged for 10 minutes in Ar prior to ramping to remove gas phase NO_2. Temperature was ramped at 10 °C/min to 500 °C with spectra being collected every 20 °C, highlighted spectra represent 50 °C (orange spectrum), and 100 °C (dark blue), 200 °C (yellow), 300 °C (light blue), 400 °C (navy), and 500 °C (black).

As expected, these final desorption temperatures differ significantly from the desorption maxima observed in microreactor experiments, though the general trends can still be established. Desorption of nitrates is shown to shift to lower temperatures as Pd-loading is increased, further suggesting the identities of the microreactor desorption events at 200-300 °C can be associated with decomposition of nitrates, their decreasing desorption temperature explained by their interaction with Pd. The Pd^{n+}(NO) bands also follow the same desorption trend as proposed in the microreactor experiments, Pd^{2+} desorbing NO at lower temperatures than Pd^{+}, though these species disappear at temperatures much lower than expected, this likely being a result of the convoluting influences of trace water, unavoidable when NO_2 is used as the adsorbate.

To better examine the desorption behavior of the Pd^{n+}(NO) bands, NO-TPD in Ar purified of water and NO_2 was performed, NO being adsorbed at 25 °C to achieve optimal band intensity. DRIFTS is especially sensitive to the presence of trace water, water adsorption occurring initially at the surface of the catalyst bed where the IR signal is reflected, leading to rapid interference with DRIFTS signals. As presented in Figure 5.4, these results demonstrate that the removal of trace water from the feed gas yields different desorption behavior, NO^{+} and Pd^{+}(NO) being still apparent even at 500 °C

during TPD. This result corroborates the assignment of the highest-temperature desorption feature to $Pd^{+}(NO)$, as this species is observed to remain adsorbed at temperatures higher than nitrates. Of further note is the appearance of nitrate features beginning at 100 °C, these species forming from NO_2 produced either by the reduction of $[Pd^{2+}(OH)]^{+}$ to Pd^{+}, reduction of PdO_x to Pd^{0}, or due to spontaneous oxidation resulting from zeolite pore-confinement effects.[132]. These data also support the presence of two Pd^{+} sites with differing desorption temperatures, as the frequency of the $Pd^{+}(NO)$ band shifts from 1828-1808 cm^{-1} with increasing temperature. As with the CO bands, this frequency shift represents a change in the relative abundances of overlapping Pd populations, the more strongly adsorbed NO species eventually becoming dominant as the other desorbs.

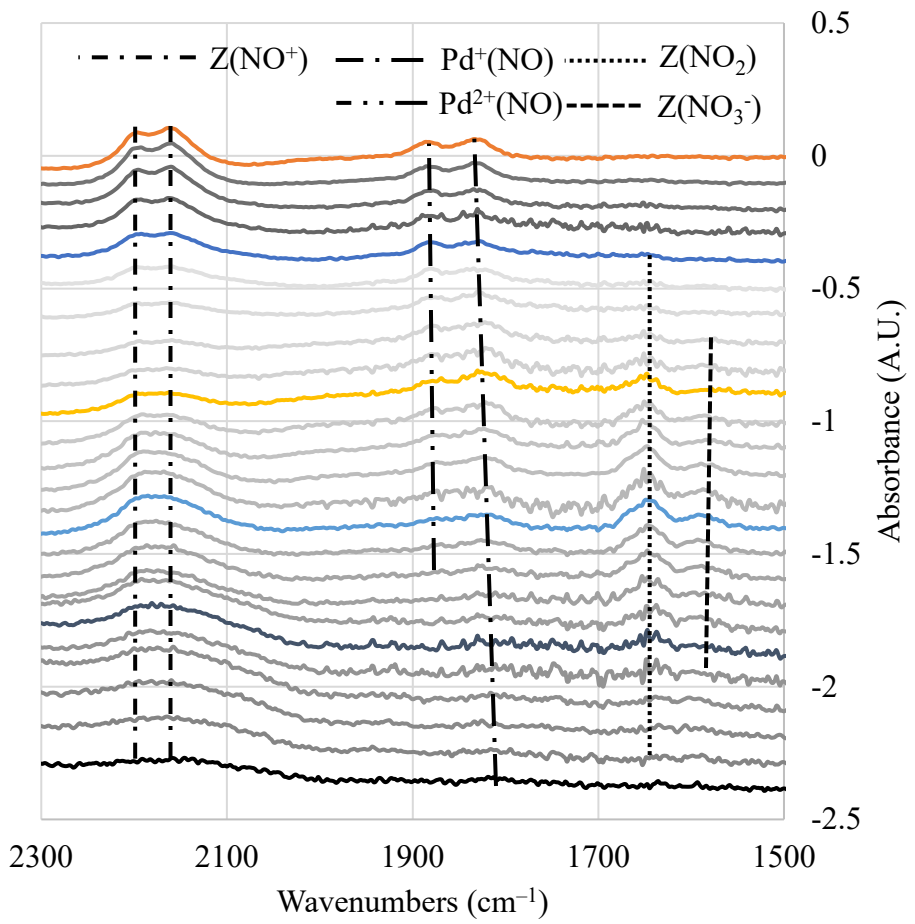

Figure 5.4 1.4% Pd-BEA: DRIFTS spectra of NO desorption after pretreatment at 500 °C for 1 h with rigorously dried Ar. NO was adsorbed for 10 minutes at 25 °C before the material was purged for 10 minutes in Ar prior to ramping to remove gas phase NO. Temperature was ramped at 10 °C/min to 500 °C with spectra being collected every 20 °C, highlighted spectra represent 25 °C (orange spectrum), and 100 °C (dark blue), 200 °C (yellow), 300 °C (light blue), 400 °C (navy), and 500 °C (black).

This section can be concluded with the putative microreactor-MS and DRIFTS-TPD assignments for the BEA materials under inert conditions as shown in Table 5.5, this table serving to reconcile nearly all the data presented at this point. However, this information still does not provide sufficient differentiation to deconvolute the NO_x desorption features to any degree of quantitative accuracy, as most desorption events overlap the desorption of one or more other species. The favorability of the various Pd species and adsorption sites for PNA applications can nevertheless be qualitatively

assessed based on their observed desorption behavior. These data suggest that the optimal sites for NO_x storage on Pd-BEA are Pd^+ sites, as these species exhibit desorption maxima between 200 and 500 °C, at which point NO_x will be converted on the downstream catalyst after desorption, while still achieving near complete NO_x desorption below 500 °C. The desorption temperatures of these species are further shifted down into the favorable range by the presence of O_2, greater quantities of NO_x being stored as NO_2 and nitrates at P-HAl sites in that case. O_2 is also proposed to limit reduction of $[Pd^{2+}(OH)]^+$ during treatment; in contrast, improved NO_x storage is observed under inert pretreatment conditions on Pd-BEA, possibly due to the additional NO_x adsorbed after $[Pd^{2+}(OH)]^+$ is reduced to Pd^+.

Table 5.2 NO_x adsorption sites with DRIFTS band frequencies and desorption endpoints correlated with microreactor desorption ranges and maxima

	In-situ DRIFTS						Microreactor-MS	
Adsorption Site	CO (cm^{-1})	NO (cm^{-1})	NO_2 (cm^{-1})	OH (cm^{-1})	CO End	NO_x End	NO_x Range	NO_x Max
Zeolite Brønsted Acid	2165	(NO^+) 2100-2250	N/A	3610	25 °C	500 °C	100-500°C	100 °C
EFAl	2185	1880	N/A	3665	25 °C	120 °C	50-120 °C	100 °C
P-HAl	2208	N/A	1589 1625 1650	3785	25 °C	300 °C 160 °C 380 °C	200-350 °C	250-300 °C
Pd^+	2119 2132	1824 1808	N/A	N/A	300 °C	500 °C	100-300 °C 350-550°C	200 °C 450 °C
$[Pd^{2+}(OH)]^+$	2125 2144	1876	N/A	3604 3656	200 °C	360 °C	100-360 °C	200 °C
Pd^{2+}	2154 2160 2169 2183	1876	N/A	N/A	200 °C			
Super-electrophilic Pd^{2+}	2189 2212	1876	N/A	N/A	200 °C			

5.2 Comparison with CHA

Similar experiments to those described in the previous section were performed on the CHA materials, the effects of atmosphere and Pd loading again being examined. Figure 5.5 shows the effects of O_2 on adsorption and desorption. The effects on the H_2-reduced and re-oxidized 0.7% Pd-CHA are also considered, given the improvement in NO_x storage capacity observed on that material. For the CHA materials, desorption events can be assigned as on BEA. The desorption behavior is easier to interpret here, O_2 appearing to improve NO_x storage in each case. This result suggests that all or nearly all the Pd^{2+} species participate in NO_x adsorption on Pd-CHA. Meanwhile, no desorption features associated with nitrates are observed in this case, as anticipated. Desorption of NO_x from Pd^{+} at high temperatures is also observed, this band shifting its maximum desorption temperature lower on the re-oxidized material. In the case of NO_x desorption when O_2 is present, elevation of NO_x desorption temperature is observed on the re-oxidized material, this likely being explained by the preferential formation of a particular Pd species.

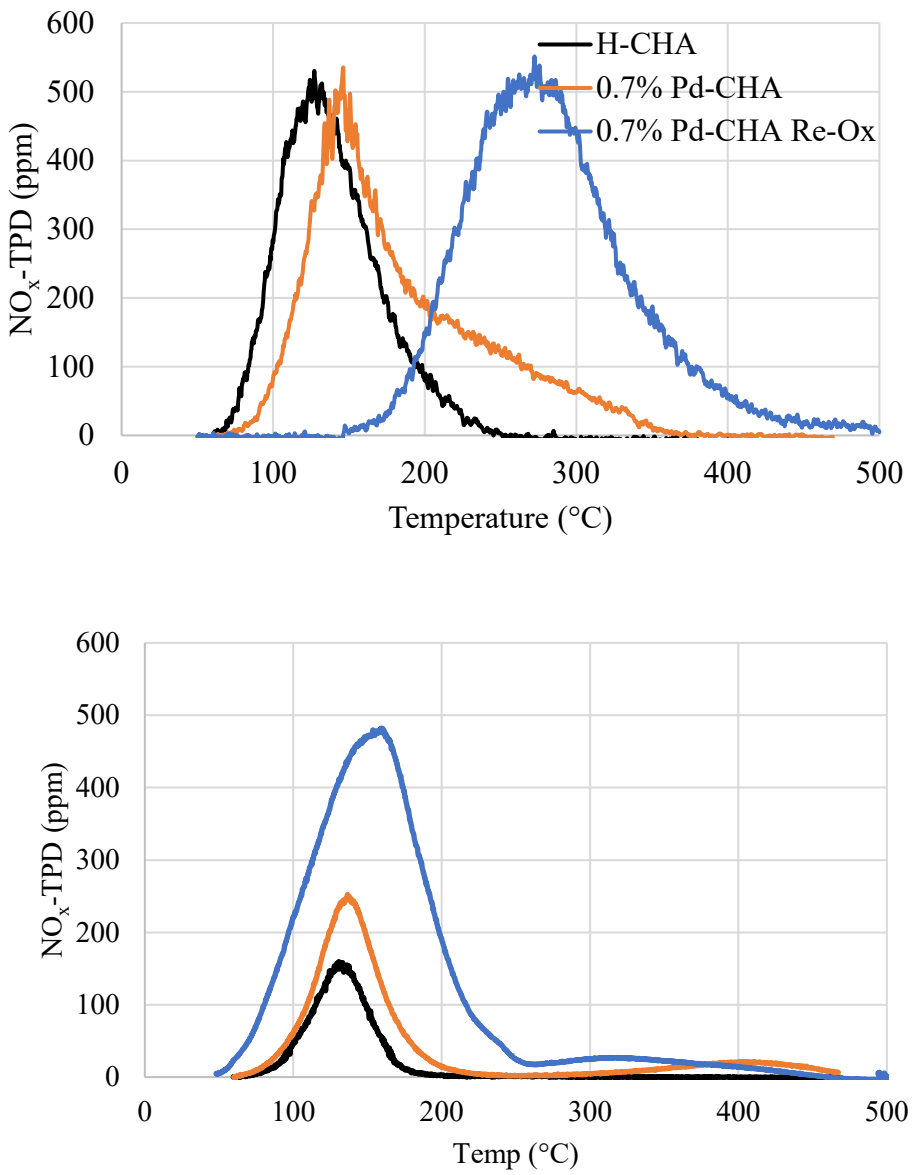

Figure 5.5 NO_x TPD on CHA materials conducted in microreactor-MS with calibrated NO_x concentrations. Materials were pretreated in 10% O_2 in He or He for 1 h prior to adsorption. 1000 ppm NO in 10% O_2/He or He was adsorbed for 10 min at 50 °C followed by a 1 h purge in 10% O_2/He or He. TPD was carried out in 10% O_2/He or He at a ramp rate of 10 °C per min. O_2 was either included (top) or excluded (bottom) during all steps.

The DRIFTS NO_x-TPD experiments were also replicated under dry conditions, these data being presented in Figure 5.6. Surprisingly, the Pd^{2+}(NO) band apparently persists at higher temperature than the Pd^{+}(NO) band, this result appearing to be at odds

with the behavior observed in microreactor experiments. Careful examination reveals a potential explanation, as the Pd^{+}(NO) band does not shift to lower frequencies on this material. This is an indication that the Pd^{+}(NO) band observed here consists primarily of the proposed low-desorption-temperature Pd^{+} species, while the high-desorbing Pd^{+}(NO) band fails to appear due to its lower abundance on CHA. This supposition is supported by comparison of CHA microreactor data with that for the BEA materials, showing that the species responsible for the highest temperature desorption event is less abundant on CHA. Using these data and microreactor experiments, a correlation chart analogous to that for BEA is shown in Table 5.3. These results again point to the greater stability of Pd^{2+} species on CHA, nearly all of the identified species likely participating in PNA behavior.

Table 5.3 NO_x adsorption sites on CHA with DRIFTS band frequencies and desorption endpoints correlated with microreactor desorption ranges and maxima

	In-situ DRIFTS						Microreactor-MS	
Adsorption Site	CO (cm^{-1})	NO (cm^{-1})	NO_2 (cm^{-1})	OH (cm^{-1})	CO End	NO_x End	NO_x Range	NO_x Max
Zeolite Brønsted Acid	2171	(NO^{+}) 2100-2250	N/A	3610	25 °C	500 °C	50-500 °C	100 °C
EFAl	2192	1872	N/A	3662	25 °C	100 °C	50-100 °C	100 °C
P-HAl	N/A	N/A	N/A	N/A	N/A	N/A	N/A	N/A
Pd^{+}	2113 2132	1803	N/A	N/A	280 °C	320 °C	100-350 °C 350-550 °C	150 °C 350-450 °C
$[Pd^{2+}(OH)]^{+}$	2125 2142	1855	N/A	N/A	280 °C	400 °C	150-400 °C	100-280 °C
Pd^{2+}	2154 2175	1855	N/A	N/A	240 °C 100 °C			
Super-electrophilic Pd^{2+}	2188 2212	1855	N/A	N/A	160 °C			

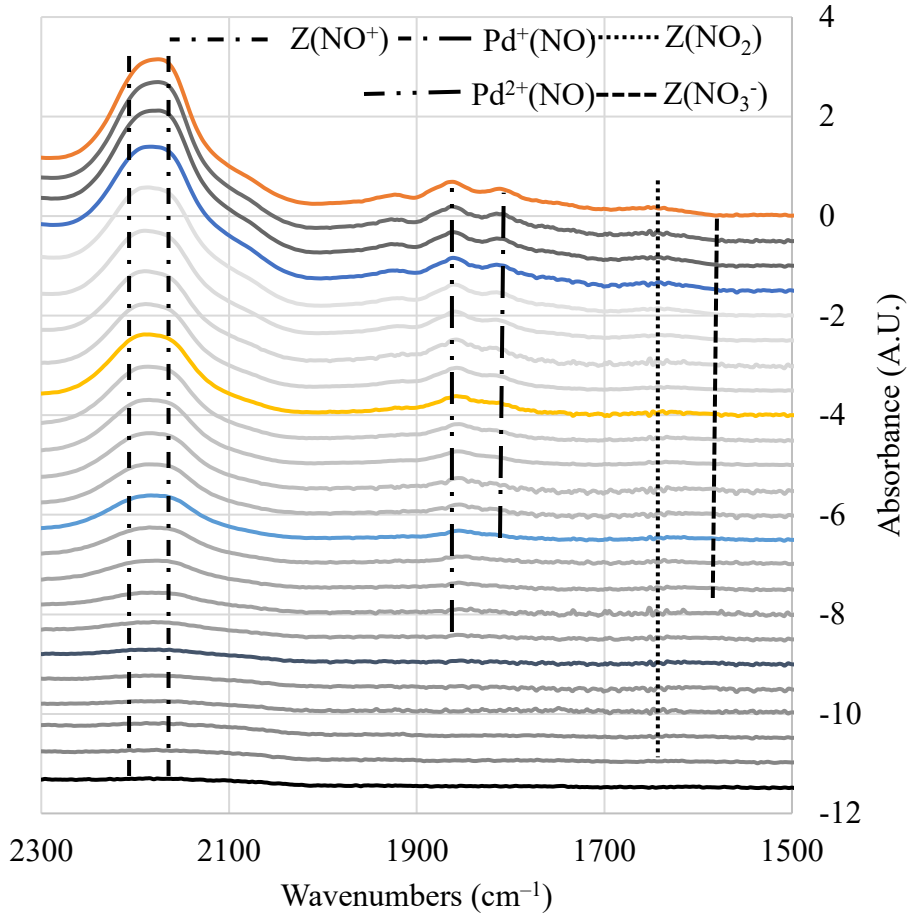

Figure 5.6 0.7% Pd-CHA: DRIFTS spectra of NO desorption after pretreatment at 500 °C for 1 h with rigorously dried Ar. NO was adsorbed for 10 minutes at 25 °C before the material was purged for 10 minutes in Ar prior to ramping to remove gas-phase NO. Temperature was ramped at 10 °C/min to 500 °C with spectra being collected every 20 °C; highlighted spectra represent 25 °C (orange spectrum), and 100 °C (dark blue), 200 °C (yellow), 300 °C (light blue), 400 °C (navy), and 500 °C (black).

5.3 Effect of NO and NO_2 on Pd Speciation of Pd-BEA

Of crucial importance to the implementation of PNA materials is their longevity under exposure to exhaust components, the impact of NO and NO_2 on Pd speciation at high temperatures still being unclear.[59] These effects were explored by pretreating 1.4% Pd-BEA zeolite under NO or NO_2 in Ar at 500 °C for 1 h, followed by CO or NO_2 adsorption to probe Pd speciation. These results are presented in Figure 5.7, compared with the material pretreated in Ar at 500 °C. These data serve to reinforce the conclusion

that NO generally reduces Pd^{n+} species at high temperatures. Of special note is the apparent reduction of $[Pd^{2+}(OH)]^+$ to Pd^+ at high temperatures, primarily Pd^+ and Pd^0 being evident after treatment. This reaction likely proceeds similarly to the manner described by Descorme et al. as shown in Equation 9.[90]

$$2(Z^-[Pd^{2+} - OH]^+) + NO \rightarrow 2(Pd^+) + NO_2 + H_2O \qquad (9)$$

Similar reduction occurs when NO_2 is employed as the treatment gas, this being explainable by the unavoidable inclusion of trace water and NO during this treatment. The greater presence of Pd^0 on the NO_2-treated material can be explained by reduction of Pd^{n+} by water, while NO_2 also serves to maintain some ionic Pd in its oxidized state. The species that benefit from NO_2 oxidation are primarily Pd^+ (2136, 2119 cm^{-1}) and the least electrophilic Pd^{2+} (2154 cm^{-1}), suggesting a process wherein Pd^{2+} is reduced to Pd^+ and Pd^0 by NO and water respectively, while NO_2 serves to re-oxidize Pd metal to Pd^+ and oxidation of Pd^+ to Pd^{2+} is less facile. This conclusion is also supported by the effect of inert pretreatment observed in microreactor and CO-DRIFTS experiments, the abundance of Pd^+ apparently being greater when O_2 is absent during pretreatment. A weak feature also appears at 1790 cm^{-1}, a concerning result suggesting that NO results in Pd particle agglomeration in a manner analogous to CO. This feature is not present when NO_2 is employed in the pretreatment, an indication that the presence of NO_2 may inhibit the agglomeration of large Pd particles.

The NO- and NO_2-treated 1.4% Pd-BEA were also examined with NO_2 as the adsorbate, these results being shown in Figure 5.8. The intensity of the $Pd^{2+}(NO)$ band remains relatively constant regardless of treatment, yet another piece of evidence that $[Pd^{2+}(OH)]^+$ and the least electrophilic Pd^{2+} sites are the primary $Pd^{2+}(NO)_x$ storage sites on the BEA materials, as the relevant CO bands are the least affected by treatment. However, the intensity of these bands is still low relative to the $Pd^+(CO)$ bands as evidenced by the position of the local band maxima at frequencies more aligned with $Pd^+(CO)$. Meanwhile, loss of the super-electrophilic Pd^{2+} is substantial, if this species were participating in NO adsorption it would be expected that the $Pd^{2+}(NO)$ band would also decrease in intensity from the as-prepared material, though this does not occur. The $Pd^+(NO)$ band is weakest on the Ar-treated material where Pd^+ quantities are relatively

low and Pd^{2+} is more abundant, then increases dramatically in intensity on the NO_2-treated material, this being consistent with the CO adsorption results that show an increase in Pd^{+}(CO) band intensity (2119 cm^{-1}) after NO_2 treatment over the as-prepared material. The behavior of the NO^{+} bands is also notable, these species increasing in abundance with the extent of Pd reduction in the order NO > NO_2 > Ar, loss of ion-exchanged Pd leading to greater availability of zeolite Brønsted acid sites that facilitate formation of these species. Additionally, enhanced nitrate adsorption is observed on the NO_2-treated material, evidence that NO_2 is formed during reduction of $[Pd^{2+}(OH)]^{+}$ upon NO adsorption at 50 °C (as per eqn. 9). This is supported by the behavior of the P-HAl(OH) band (Figure S4) under these conditions; this band remains relatively constant in intensity, thus indicating the additional nitrate formation is not a result of additional P-HAl formation.

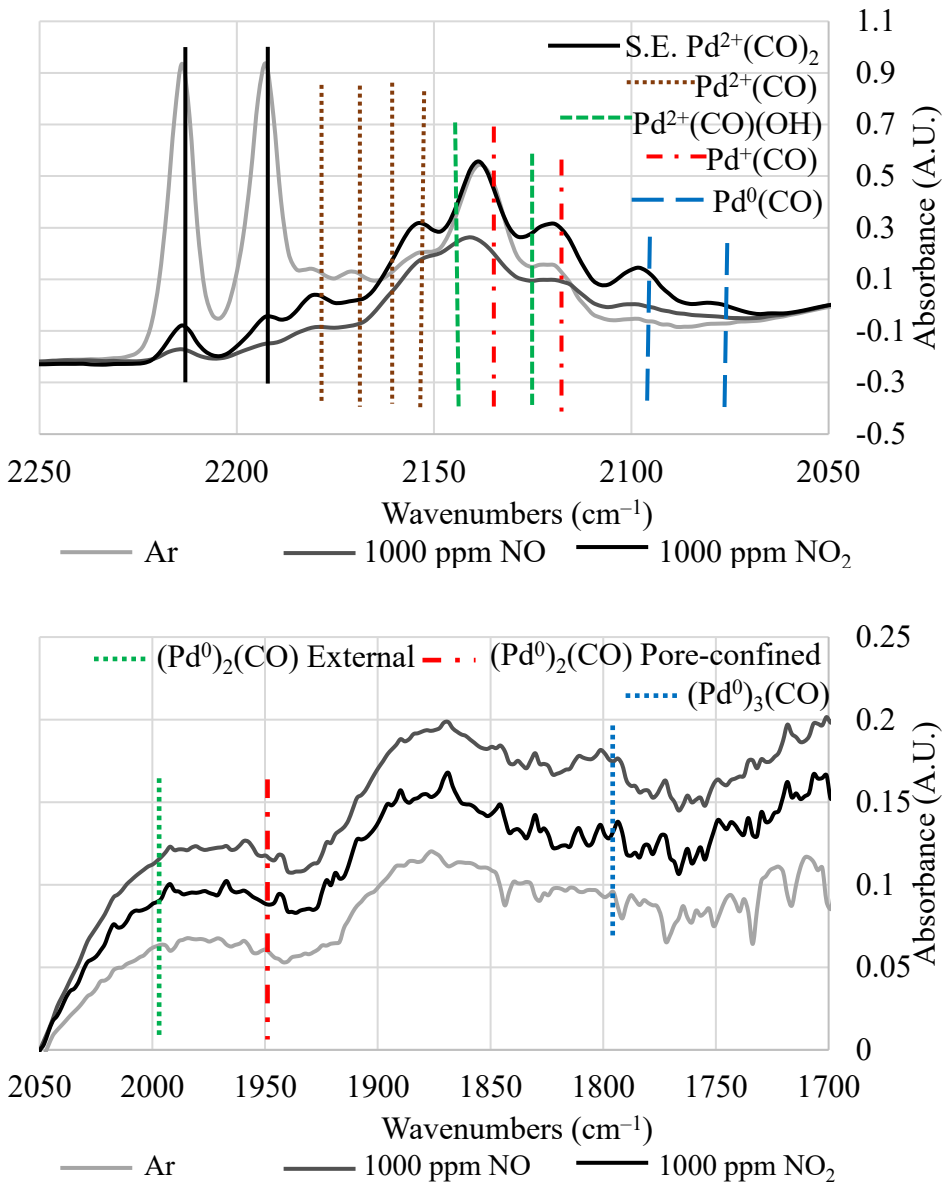

Figure 5.7 1.4% Pd-BEA: DRIFT spectra of CO adsorption after pretreatment at 500 °C for 1 h with rigorously dried Ar, 1000 ppm NO in Ar or 1000 ppm NO_2 in Ar. CO was adsorbed for 10 minutes at 25 °C. Top: ionic Pd range. Bottom: metallic Pd range.

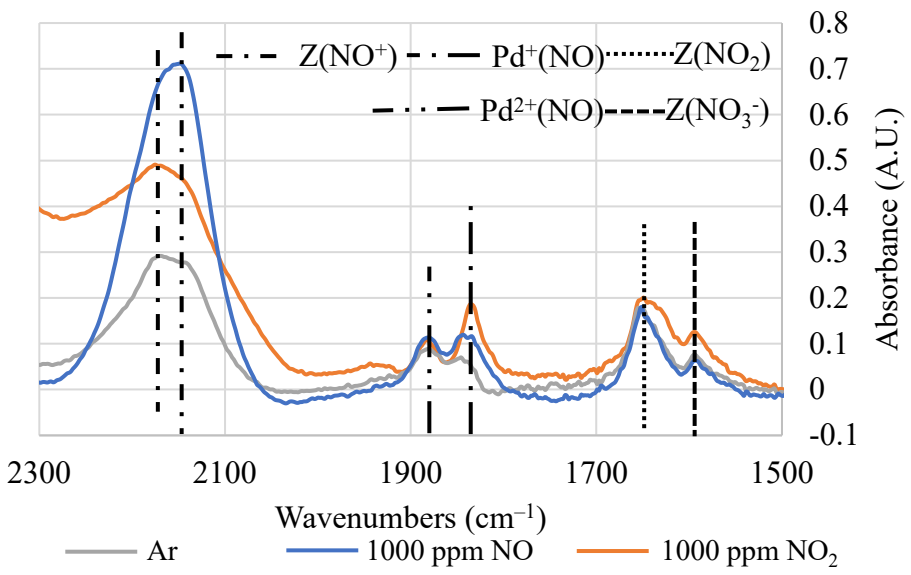

Figure 5.8 1.4% Pd-BEA: DRIFT spectra of NO_2 adsorption after pretreatment at 500 °C for 1 h with rigorously dried Ar, 1000 ppm NO in Ar or 1000 ppm NO_2 in Ar. NO_2 was adsorbed for 10 minutes at 50 °C.

To further explore the interaction between NO, NO_2, and Pd^+, 1.4% Pd-BEA was reduced in H_2 at 500 °C for 1 h and then exposed to NO for ten minutes, followed by NO_2 for ten minutes at 25, 50 and 100 °C (Figure 5.9). Regardless of temperature, only the band assigned to NO adsorbed at EFAl or Brønsted acid sites is apparent upon NO exposure, along with an extremely broad, weak feature in the Pd^+(NO) range, this possibly corresponding to a water pseudo-maximum. The formation of NO^+ is also inhibited under these conditions, only very weak features appearing, as Pd metal particles limit diffusion to Brønsted acid sites. NO_2 adsorption spectra are more revealing, however, Pd^{n+}(NO) bands failing to appear at 25 °C, while at 50 °C Pd^+(NO) is formed preferentially, and finally at 100 °C Pd^{2+} and Pd^+(NO) bands are present at nearly equal intensity. The intensity of the nitrate bands also decreases with increasing temperature, a result indicating that much of the NO_2 is consumed during Pd oxidation, nitrate bands not appearing until oxidation is nearly complete. The NO^+ bands also support this conclusion, these growing less intense as the extent of Pd reoxidation increases and more NO is stored as nitrosyl species.

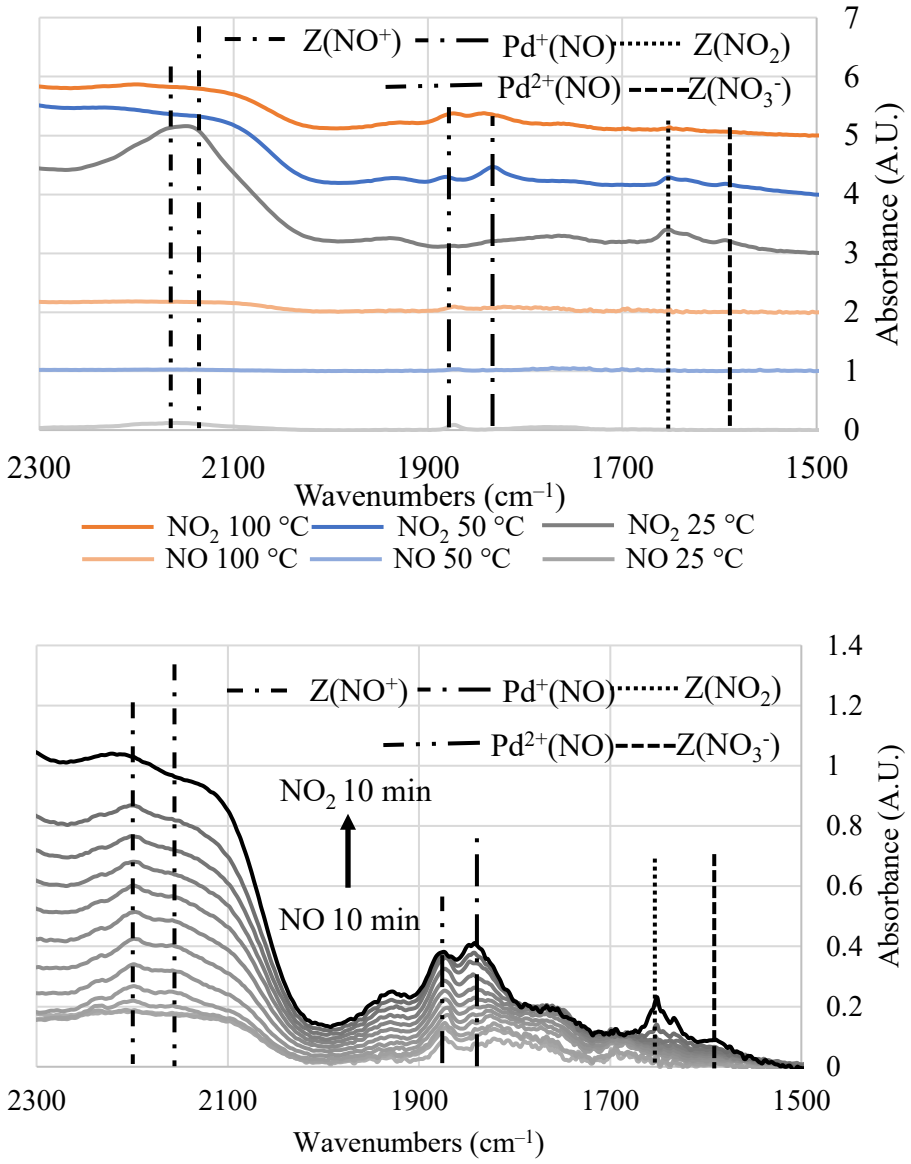

Figure 5.9 1.4% Pd-BEA: Top: DRIFT spectra of NO-NO_2 sequential adsorption after pretreatment at 500 °C for 1 h with 10% H_2. NO was adsorbed for 10 min at 25, 50 or 100 °C followed by NO_2 adsorption for 10 minutes. Bottom: Time-resolved spectra of NO_2 adsorption at 100 °C, the black spectrum being that collected after Ar purge for 10 min.

To provide further evidence for these inferences, the time-resolved spectrum of NO_2 adsorption at 100 °C shows that Pd^{2+} and Pd^{+} begin to appear simultaneously, the Pd^{2+}(NO) band achieving maximum intensity at 9 minutes, while Pd^{+}(NO) continues to form. Nitrate bands begin to appear at 10 minutes. The spectrum collected prior to

desorption is also included here, this being collected after a 10 min Ar purge to remove gas-phase species before desorption. This spectrum reveals that Pd^{+}(NO) continues to form, as do nitrate features, even as the concentration of NO_2 in the feed decreased as the adsorbate gas was cleared from the cell. Figure S5 shows the OH region during this experiment, these results showing no strong interaction with the P-HAl(OH) band until nitrates begin to form.

To conclude this section, the reactivity of NO and NO_2 with Pd species on BEA zeolite have been explored. NO apparently has a substantially reducing effect on ion-exchanged Pd at 500 °C. The consistent intensity of the Pd^{2+}(NO) IR band under differing treatment gases suggests that not all Pd^{2+} species participate in NO_x adsorption in the case of BEA, otherwise the loss of super-electrophilic Pd^{2+} would be evident as a decrease in the intensity of the Pd^{2+}(NO) band. Meanwhile, the intensity of the Pd^{+}(CO) and Pd^{+}(NO) IR bands increases after pretreatment in NO and NO_2, the NO_2-treated material showing a greater preference for Pd^{+} formation than even the material pretreated in Ar. This indicates that NO_2 serves to re-oxidize Pd metal to Pd^{+} at 50 °C, while reoxidation to Pd^{2+} is less extensive. The effect of NO and NO_2 on the H_2-reduced 1.4% Pd-BEA was examined at various temperatures, NO adsorption failing to re-oxidize Pd to form nitrosyl bands at any of the evaluated temperatures, indicating that NO does not have an oxidizing effect on Pd. NO_2 adsorption at 25 °C similarly fails to produce nitrosyl bands, while at 50 °C Pd^{+}(NO) species are formed preferentially and at 100 °C additional Pd^{2+}(NO) species form. Nitrate bands can be used to gauge the extent of re-oxidation as their appearance coincides with the endpoint of NO_2 consumption by Pd oxidation, these data also serving to establish temporal coordination between the appearance of nitrates and disappearance of the P-HAl(OH) band.

5.4 Effect of NO and NO_2 on Pd Speciation of Pd-CHA

Similar experiments to those presented in the previous section were performed on 0.7% Pd-CHA to assess the impact of NO and NO_2 on the Pd speciation of this material. Pd speciation after treatment was initially examined by CO adsorption, the results presented in Figure 5.10. In this case, the Pd species primarily affected by NO treatment

is the super-electrophilic Pd^{2+}, these CO bands being greatly reduced in intensity upon treatment at 500 °C in both NO and NO_2. Notably, the $[Pd^{2+}(OH)]^+$ bands are unaffected in either gas, while Pd^+ and the less electrophilic $Pd^{2+}(CO)$ bands increase in intensity after treatment. These observations suggest that $[Pd^{2+}(OH)]^+$ is more stable on Pd-CHA than on Pd-BEA. Examination of the metallic Pd(CO) region again reveals the presence of the band at 1790 cm^{-1} after NO treatment, corresponding to a site involved in the agglomeration of large Pd particles. Meanwhile this band is absent on the NO_2-treated material as observed on Pd-BEA. The increased presence of pore-confined Pd particles is also observed after treatment in either gas, further demonstrating the reducing effect of NO. Aside from the absence of the band at 1790 cm^{-1}, the NO- and NO_2-treated CHA material show remarkably similar CO adsorption spectra, indicating the oxidizing effect of NO_2 is less pronounced than observed on Pd-BEA.

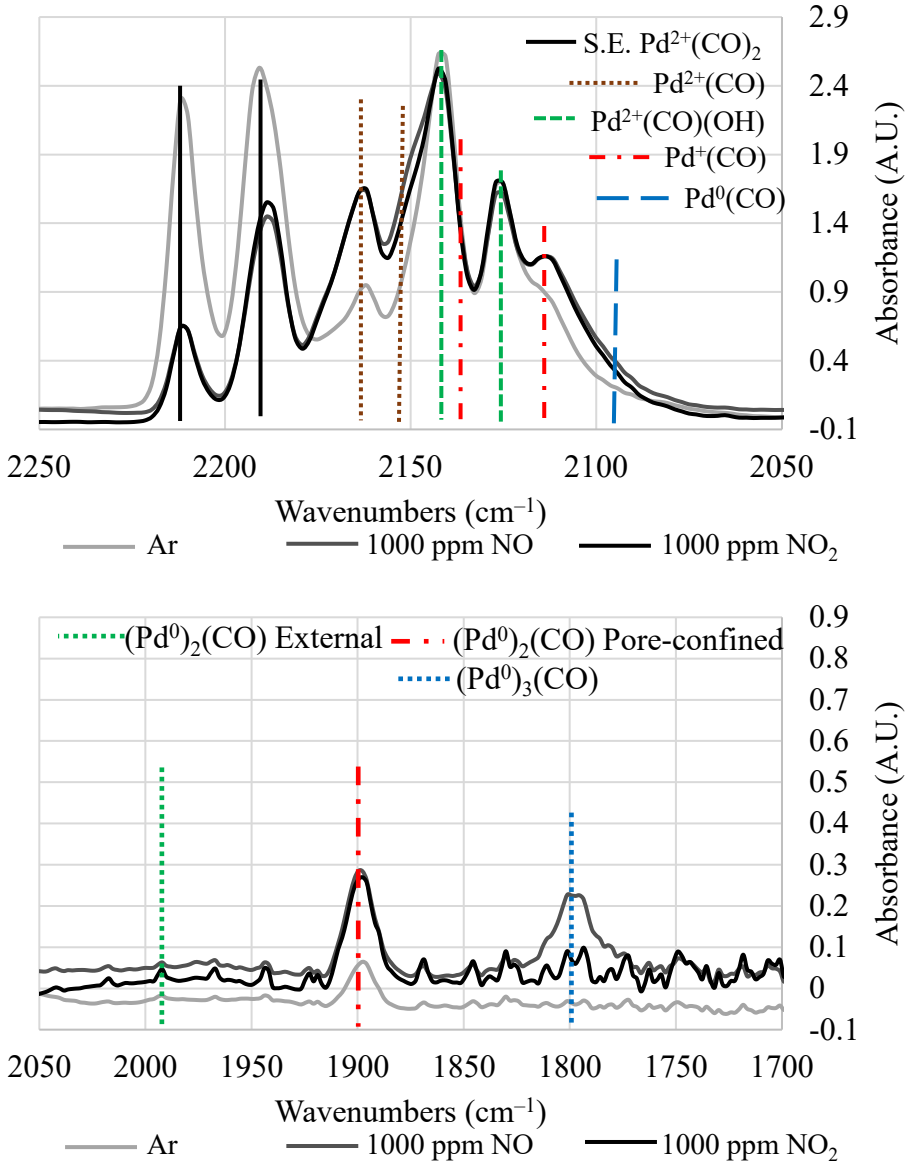

Figure 5.10 0.7% Pd-CHA: DRIFT spectra of CO adsorption after pretreatment at 500 °C for 1 h with rigorously dried Ar, 1000 ppm NO in Ar or 1000 ppm NO_2 in Ar. CO was adsorbed for 10 minutes at 25 °C. Top: ionic Pd range. Bottom: metallic Pd range.

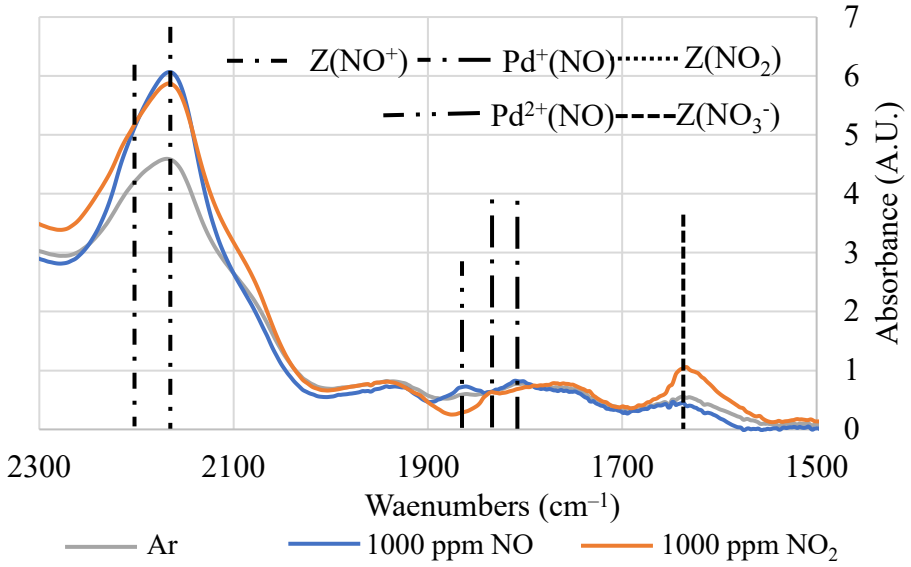

Figure 5.11 0.7% Pd-CHA: DRIFT spectra of NO_2 adsorption after pretreatment at 500 °C for 1 h with rigorously dried Ar, 1000 ppm NO in Ar or 1000 ppm NO_2 in Ar. NO_2 was adsorbed for 10 minutes at 50 °C.

Given the similarity of the CO adsorption spectra of the Pd-CHA material, it could also be expected to exhibit similar NO_2 adsorption spectra; however, this is not the case. Figure 5.11 shows NO_2 adsorption after pretreatment in NO or NO_2, these results again being compared to the Ar-pretreated material. Unlike the CO adsorption spectra, NO treatment leads to little change in the NO_2 adsorption spectrum, nitrosyl bands being of similar intensity to those observed after Ar treatment, a result that suggests much of the super-electrophilic Pd^{2+} (nearly eliminated in CO DRIFTS after NO treatment) is converted to less electrophilic Pd^{2+} and Pd^{+}, these species still participating in NO_x adsorption. Indications of Pd reduction can still be observed in the increased intensity of NO^{+} bands, again indicating greater availability of Brønsted acid sites after NO and NO_2 treatment at 500 °C. However, the NO_2-pretreated material shows a dramatically different spectrum, a new nitrosyl band appearing at 1825 cm^{-1} in conjunction with a nitrate band at 1627 cm^{-1}. This result is surprising given the similarity of the CO adsorption spectra and suggests that PdO_x may be involved in the observed changes, as PdO_x does not readily adsorb CO. A further indication of the involvement of PdO_x is the lack of a corresponding increase in the intensity of the P-HAl(OH) band in the presence of nitrates, suggesting that P-HAl is not the adsorption site playing host to nitrates under this

circumstance (Figure S6). Further analysis will be required to establish the true nature of this site, including examination of a CHA material with higher initial Pd dispersion. These data also suggest an alternative explanation for the observed changes in the CHA NO_x desorption behavior upon reoxidation from H_2 reduction, the formation of nitrate-supporting sites leading to the observed increase in NO_x desorption temperature, an inference supported by the similar desorption temperatures of this event and the desorption of nitrates from BEA. However, as with the absence of low-temperature NO_x desorption in that case, the absence of the typical Pd^{n+}(NO) bands in this case is not readily explained, formation of high abundances of Pd^{+} being yet another alternative explanation for these results.

5.5 Conclusions

To summarize the results of this chapter, microreactor-MS studies of NO_x desorption were carried out with and without oxygen to facilitate association of NO_x desorption events in both MS and DRIFTS studies. These experiments show that the presence of O_2 is important in determining the Pd speciation during treatment by maintaining Pd^{2+} in ionic form. Meanwhile, the adsorbate speciation during adsorption is also shown to be affected by the presence of O_2 while O_2 also serves to lower the desorption temperature of most species during the desorption step. The presence of O_2 during pretreatment of Pd-BEA is shown to decrease NO_x storage due to the formation of Pd^{2+} species that don't participate in NO_x adsorption, while Pd-CHA shows an increase in NO_x storage after air treatment due to the participation of additional types of Pd^{2+} on this material. The presence of O_2 during adsorption facilitates formation of NO_2, this being stored as nitrates at P-HAl sites, while the presence of O_2 during desorption generally decreases the desorption temperature of all species. By examining the effect of Pd-loading on NO_x desorption, inferences about the Pd-related NO_x desorption features can be derived. As Pd-loading increases, the desorption event at 300 °C gradually disappears, an indication that this feature is representative of nitrates adsorbed at P-HAl. The shift of this event to lower temperatures is also indicative of interaction of these sites with Pd. This supposition is further corroborated by DRIFTS NO_2-TPD, these spectra showing a decrease in the nitrate desorption endpoint temperature as Pd-loading increases.

Conversely, the Pd-CHA material shows no evidence of a desorption event at 300 °C, in agreement with its weak expression of the P-HAl(OH) band. DRIFTS NO-TPD under rigorously dried conditions was employed to assess the desorption of nitrosyl and NO^+ species, both NO^+ and Pd^+(NO) bands remaining to 500 °C. Previous studies have shown lower desorption temperatures for NO^+, though these species have also been shown to be highly sensitive to the presence of water. Therefore, the higher desorption temperature of these species can be inferred to be a result of the rigorous removal of trace water during these experiments.[95, 102] From these data, it can be inferred that most Pd^{2+}(NO) desorbs below 300 °C, the maximum desorption occurring at ~200 °C. NO is proposed to desorb from Pd^+ in two discreet events, one in a similar range to Pd^{2+}(NO) while the other desorbs at ~450 °C, this result supported by the changing frequency of the relevant Pd^+(NO) IR band as desorption proceeds. The CHA material exhibits similar behavior aside from the absence of nitrates and P-HAl, however desorption from the various Pd^{2+} species cannot be easily differentiated. In fact, most of these desorption events overlap to at least some degree, thus limiting these studies to qualitative assessment.

The effect of NO and NO_2 at high temperature on these materials was also examined, NO being demonstrated to generally reduce ion-exchanged Pd on BEA, while only super-electrophilic Pd^{2+} is reduced on Pd-CHA. NO_2 treatment leads to comparatively better retention of ionic Pd, especially Pd^+ and $[Pd^{2+}(OH)]^+$. A concerning result is the appearance of the $(Pd^0)_3$(CO) band at 1790 cm^{-1} after NO treatment on both materials, this species being associated with the agglomeration of large Pd particles. This band is absent after NO_2 treatment, suggesting that NO_2 may inhibit the formation of this CO adsorption site. Adsorption of NO_2 after NO or NO_2 pretreatment was also conducted, NO_2 pretreatment leading to an increase in the intensity of the Pd^+(NO) band on Pd-BEA, while NO_2 pretreatment on Pd-CHA leads to the appearance of a nitrate band and a single nitrosyl species, an unexpected result given the similarity of the CO adsorption spectra and an indication that the NO_x adsorption behavior is substantially altered by treatment in NO_2.

CHAPTER 6. CONCLUSIONS

In this dissertation, two Pd-loaded zeolite materials were assessed for their potential to serve as PNA's. Generally, the addition of Pd to these materials is shown to enhance the NO_x adsorption capacity while also leading to higher NO_x desorption temperatures. The effects of Pd-loading on the Pd speciation of BEA were also assessed, these results allowing for the development of a self-consistent set of FT-IR band assignments that could be correlated with microreactor MS-desorption events. The most consequential results of these comparisons are the identification of Pd and zeolite sites that actively participate in NO_x storage and desorb NO_x near or above 200 °C. For BEA, these NO_x adsorption sites consist of Pd^+, $[Pd^{2+}(OH)]^+$, P-HAl, and possibly other Pd^{2+} species, though the super-electrophilic Pd^{2+} formed on this material is unlikely to adsorb NO_x given its sensitivity to reduction by water that will be unavoidably present under realistic conditions. Further, increasing Pd loading is shown to decrease the desorption temperature of nitrate species, this result, along with an abundance of other evidence, indicating the interaction of Pd with P-HAl sites. Pd-CHA shows differing behavior, the absence of P-HAl and nitrates leading to a lower average NO_x desorption temperature from this material, while all or nearly all the Pd^{2+} species evidently participate in NO_x storage. The highest temperature desorption event on both CHA and BEA occurs between 400 and 550 °C and can be tied to $Pd^+(NO)$, the abundance of this species being favored when the materials are pretreated under inert conditions.

The stability of the Pd speciation of both materials was also examined, BEA being found to be more sensitive to Pd reduction in all respects due to its larger pore size. CO and NO are shown to be especially problematic for the retention of ion-exchanged Pd, exposure of both materials to these gases at high temperature leading to formation of large Pd particles outside the zeolite framework that are more susceptible to sintering. This result suggests these materials will not be able to achieve sufficient lifetime for real-world applications on stoichiometric automotive systems, whereas the positive effects of O_2 and NO_2 on Pd speciation and NO_x adsorption suggest these materials may be applicable to lean diesel systems. If a DOC were placed upstream of the PNA, this would

eliminate all the NO and CO in favor of NO_2 and CO_2, these gases being more benign in their effects on Pd speciation. Both materials have advantages and disadvantages: Pd-CHA exhibits greater NO_x storage in the absence of water, but BEA shows better performance than CHA when water is present. However, the BEA material will likely suffer more rapid deactivation and has lower hydrothermal stability than the CHA material; therefore, CHA is still more likely to be applicable under realistic conditions. The dramatically different behavior of these materials despite their similar Si/Al ratios serves to highlight the fact that framework structure and pore diameter are key parameters in the control of Pd-speciation and thus NO_x adsorption. This also indicates further improvement of the PNA behavior of Pd zeolites is likely possible through the control of zeolite Al-O(H)-Si site proximity, the preferential formation of particular Pd^{n+} species being possible under those circumstances. While this work serves to highlight many problematic aspects of long-term PNA stability, identifying these issues is the first step in resolving them and further developments may still reveal a viable PNA material. Even if such a system only achieves limited implementation it could still lead to the elimination of millions of tons of NO_x emissions each year, and thus the potential impact of this work cannot be understated.

APPENDICES

APPENDIX 1. EXPERIMENTAL PROCEDURES

A 1.1 In-Situ DRIFTS

In-situ DRIFTS studies were carried out in a Harrick Scientific Praying Mantis DRIFTS cell equipped with a high-temperature reaction chamber. In each case a gas flow rate of 50 sccm was employed, and approximately 50 mg of catalyst material was loaded into the sample cup of the DRIFTS cell such that gas must flow through the catalyst bed. This system was also equipped with a custom-built feed-bypass manifold to allow for simultaneous blending of up to eight gases, as well as the rapid switching between different gas feeds. Gas flow control is achieved with mass flow controllers operated with Brooks instrument control interfaces, the gas flow being calibrated periodically to achieve precise gas blend concentrations. To purify feed gases of trace species such as water and NO_2, a dry ice-acetone cold trap was employed. This device consisted of a long copper coil packed with glass beads and submerged in the dry ice-acetone mixture contained in a Dewar. A bypass of the trap was also added so that higher boiling adsorbates and treatment gases could be employed at will and each loop of the manifold was equipped with a backpressure valve to maintain a consistent positive pressure of 1 psi throughout the system. The IR spectrometer used for these experiments was a Nicolet 6700 FT-IR equipped with a liquid nitrogen-cooled MCT-A detector. The FT-IR collection parameters were kept constant across all experiments, 116 scans being collected for each spectrum at a resolution of 4 cm^{-1}. The collection time for each spectrum was approximately 1 minute, these parameters allowing sufficient temporal resolution to examine gas adsorption over time.

Each DRIFTS experiment consisted of three phases: pretreatment, adsorption, and desorption steps. In each case the pretreatment was carried out at 500 °C for 1 h to remove adsorbed water from the zeolite, this being necessary due to the inhibiting effects of water on the adsorption of other species. If a strongly adsorbing species such as NO_2 or NH_3 was employed during pretreatment, the treatment gas was switched off after 1h and the temperature was increased to 550 °C for 10 min to achieve desorption of these

species. The final part of the pretreatment is a period of cooling to the desired adsorption temperature, background FT-IR spectra being collected every 20 °C to compensate for thermal effects on the zeolite FT-IR spectrum during desorption. During cooling, the adsorption gas was prepared on the manifold bypass loop to achieve stable concentration of the adsorbate prior to the beginning of the adsorption step. Adsorption was then carried out by switching the bypass and reactor gas feeds, and the cold trap was bypassed if necessary. Adsorption was carried out at a constant temperature for 10 min followed by a switch back to the gas employed during cooling. This was followed by a 10 min purge to remove any remaining adsorption gas from the system prior to desorption. Desorption was achieved by ramping the temperature of the cell from the adsorption temperature to 500 °C at a rate of approximately 10 °C per min. Spectra were collected every 20 °C at the same temperatures as those collected during cooling.

A 1.2 Microreactor-MS

Microreactor-MS studies were carried out using a Micromeritics Autochem-II microreactor system equipped with a Thermo-QMS 200 MS to measure gas concentrations at the outlet. This system employs a U-shaped quartz tube as a microreactor, supported inside a furnace. Approximately 0.1 g of material was supported on quartz wool inside the reactor tube such that gas must flow through the material. This system requires a flow rate of 100 sccm. NO_x concentrations were calibrated by measuring the background response of m/z 30 (NO) and the response at a NO concentration of 1000 ppm. The steps of these experiments are like those employed in DRIFTS studies, the primary difference being the need to purge the material for 1 h after adsorption to remove weakly adsorbed species. Otherwise, these experiments were intentionally conducted in as similar a manner as possible to the DRIFTS experiments to facilitate comparison between the two.

A 1.3 Atomic Absorption Spectroscopy

A Perkin Elmer AAnalyst 300 AAS system was employed for this analysis, these experiments being conducted by Mr. Trevor Lardinois at Purdue University. Prior to analysis, 20-50 mg of the Pd-loaded zeolite materials were digested with 2.5 g of HF (48 wt%, Sigma Aldrich) followed by dilution with 50 g 18.2 MΩ de-ionized water.

Following analysis, the Si/Al ratio was estimated using a molar composition of $Si_{(1-x)}O_2Al_x$.

A 1.4 H_2-TPR

H_2-TPR was carried out using a Micromeritics 2920 chemisorption analyzer equipped with a Cryocooler II accessory for low-temperature analysis. Materials were pretreated in flowing air (30 sccm) to 200-550 °C for 1 h, then cooled in flowing Ar to –70 °C, then switched to a flow of 5.01% H_2 in Ar (10 sccm) A cold trap was used to remove water from the gas prior to detection with a thermal conductivity detector. After baseline stabilization (~ 30 min), the sample was heated to 300 °C followed by a 30 min isothermal hold at 300 °C. TCD signals were calibrated similarly to the MS signals.

A 1.5 In-situ near-ambient pressure XPS

These experiments were performed by Dr. Olivier Heintz at the University of Burgundy, France. A PHI 5000 Versaprobe XPS system was employed for this study, this system equipped with a monochromatic Al K_1 X-Ray source with an energy of 1486.6 eV, spot diameter of 200 µm, acceleration voltage of 15 kV and power of 50 W. High-resolution scans were collected in the Pd 3d region with a pass energy of 58.7 eV. The Al 2p signal at 74.4 eV was used for energy calibration, measurements being performed with a neutralization system. CasaXPS was used for data processing and Landau ionization cross-sections were employed to quantify the semi-empirical relative sensitivity factors. The pretreatment chamber and Steatite sample holders employed were constructed in-house. Pretreatment was carried out in Ar, air or 10% H_2, at either 500 or 750 °C for 1 h, pretreatment being conducted such that no exposure to atmosphere occurred prior to analysis.

APPENDIX 2. MATERIAL SYNTHESIS AND CHARACTERIZATION

Zeolite synthesis and preparation was performed by Mr. Trevor Lardinois at Purdue University. The NH_4-BEA zeolite was obtained from Zeolyst International (CP814E, Si/Al = 12.5). The CHA zeolite was hydrothermally synthesized according to previously published procedures (SSZ-13, Si/Al_{gel} = 15). In summary, the reagents used in these preparations were Ludox HS-40 (40 wt%, Sigma Aldrich), $Al(OH)_3$ (98 wt%, SPI Pharma), trimethyladamantylammonium hydroxide (TMAdaOH, 25 wt%, Sachem), NaOH pellets (98 wt%, Alfa Aesar), and deionized water (18.2 MΩ) added in the molar ratios 1 SiO_2/ 0.0667 Al/ 0.25 TMAdaOH/ 0.25 Na/ 44 H_2O to form the precursor gel. In a PFA container with a Teflon(CO)ated magnetic stir bar, TMAdaOH and water were mixed for 15 min prior to the addition of $Al(OH)_3$ and NaOH pellets. Upon dissolution of the solids, the Si precursor was added and the mixture was stirred for an additional 2 h. The synthesis gel was then transferred to sealed, Teflon-lined stainless-steel autoclaves (Parr Instrument Company) and placed in a convection oven at 160 °C with daily quenching and stirring (5 min).

The silicious zeolite BEA was synthesized according to literature procedures with molar gel ratios of 0.54 tetraethylammonium hydroxide (TEAOH, 40 wt%, Sigma Aldrich), 1.0 tetraethyl orthosilicate (TEOS, 98 wt%, Sigma Aldrich), 7.25 deionized water (18.2 MΩ), and 0.54 hydrofluoric acid (48 wt%, Sigma Aldrich). TEAOH and TEOS were combined in excess water contained in a PFA vessel with Teflon stir bar. The resulting mixture was stirred under flowing air to evaporate EtOH, additional water added as necessary to achieve the final molar ratio. HF was then added dropwise with intermittent stirring, and then loaded into Teflon-lined stainless-steel autoclaves and heated in an oven to 140 °C.

After 7 days, all the zeolite materials were recovered using a centrifuge and washed a total of seven times alternating between water and acetone (99.9 wt%, Sigma-Aldrich), water comprising the last wash. The resulting solids were dried in a static oven at 100 °C prior to treatment in flowing air (100 cm^3 min^{-1}, Air Zero, Indiana Oxygen) to 580 °C with a ramp rate of 1 °C per min for 10 h. At this point, powder XRD was performed with a Rigaku Smart-Lab X-ray diffractometer (XRD) using a Cu Kα (λ =

0.154 nm) radiation source, these results shown in Figure A2.1. The resulting diffraction patterns serve to confirm the framework structure of each batch of the various materials prior to combination. The CHA material was ion-exchanged into the NH_4-form through ion-exchange with 1 M NH_4NO_3 at a ratio of 150 g of solution per g of solid under ambient conditions for at least 24 h. The solutions were centrifuged and washed with water 4 times, followed by centrifugation to recover the solids. The recovered solids were then dried for at least 12 h at 100 °C. N_2 physisorption was performed with a Micromeritics ASAP 2020 Surface Area and Porosity Analyzer, the results being presented in Figure A2.2. The pore volumes were found to be consistent with those observed in literature reports.

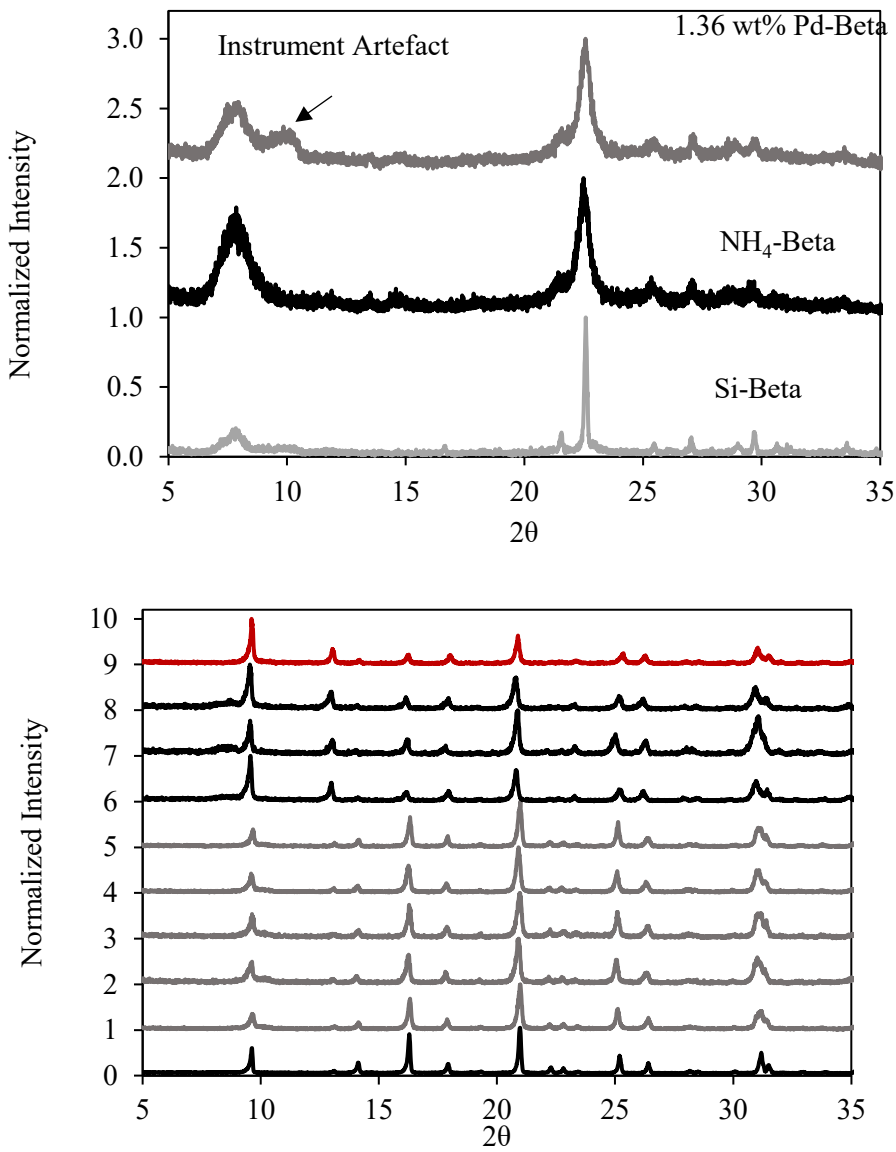

Figure A2.1. Ex-situ X-ray diffraction (XRD) patterns normalized to maximum intensity. (Left) XRD of Si-Beta (gray, bottom), NH_4-Beta (black, offset +1 a.u.), and 1.36 wt% Pd-Beta (gray, offset +2 a.u.). Instrument artifact (labeled) is from sample holder. (Right) XRD of a reference Si-CHA (black, bottom), 8 independent CHA syntheses (Si/Algel = 15) of similar zeolite gel composition before mixing into a larger batch (gray for synthesis aliquots, black for CHA samples that were washed and air-treated to 580 °C for 10 hours, offset range +1 to +8 a.u.), and a 0.7 wt% Pd-CHA sample (red, offset +9 a.u.).

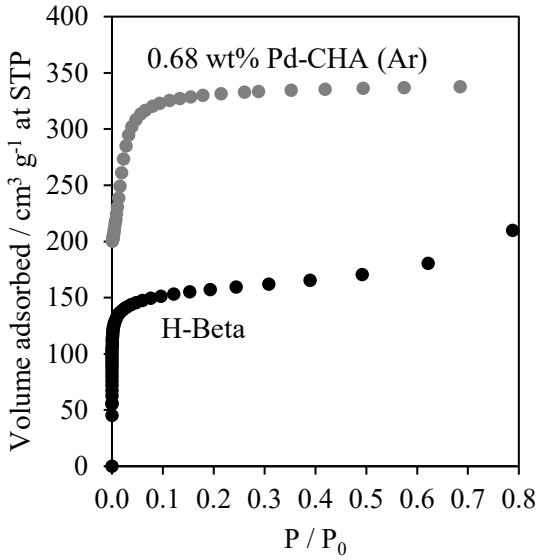

Figure A2.2 N_2 (-196 °C) adsorption isotherm for H-form Beta (black circles) and Ar (-186 °C) adsorption isotherm for 0.7 wt% Pd-CHA (gray circles, offset +200 cm^3 g^{-1} at STP).

Pd-loaded materials were prepared via incipient wetness impregnation. A dilute aqueous $Pd(NH_3)_4(NO_3)_2$ (10 wt% solution, Sigma Aldrich) solution was added drop-wise to the NH_4-form material while stirring, until adequate solution was added to completely fill the zeolite pore volume. The resulting solids were dried in static air at 120 °C for at least 12 h before treatment in flowing air at 100 sccm to 550 °C at a ramp rate of 2 °C per min. XRD was again used to confirm the framework topology of the Pd exchanged materials, indicating no significant structural changes occurred during impregnation, these results also being shown in Figure A2.1.

To establish the extent of Pd ion-exchange, H_2-TPR was employed as described above. Figure A2.3 shows the results of these experiments on both the Pd BEA and CHA materials, the integrated area of H_2 consumption events being used to calculate the Pd_{iso}/Pd_{tot} ratio. This is possible due to the differing reduction temperatures of PdO_x particles and ion-exchanged Pd, these species reducing at –10–35 °C and 35–200 °C, respectively. This calculation assumes a 1:1 H_2:Pd^{2+} stoichiometry to quantify the number of divalent Pd cations in each reduction event. Apparent H_2 consumption is also observed at –40 °C, though in reality this feature corresponds to desorption of Ar from the framework pores, this feature also being observed on the H-form materials.

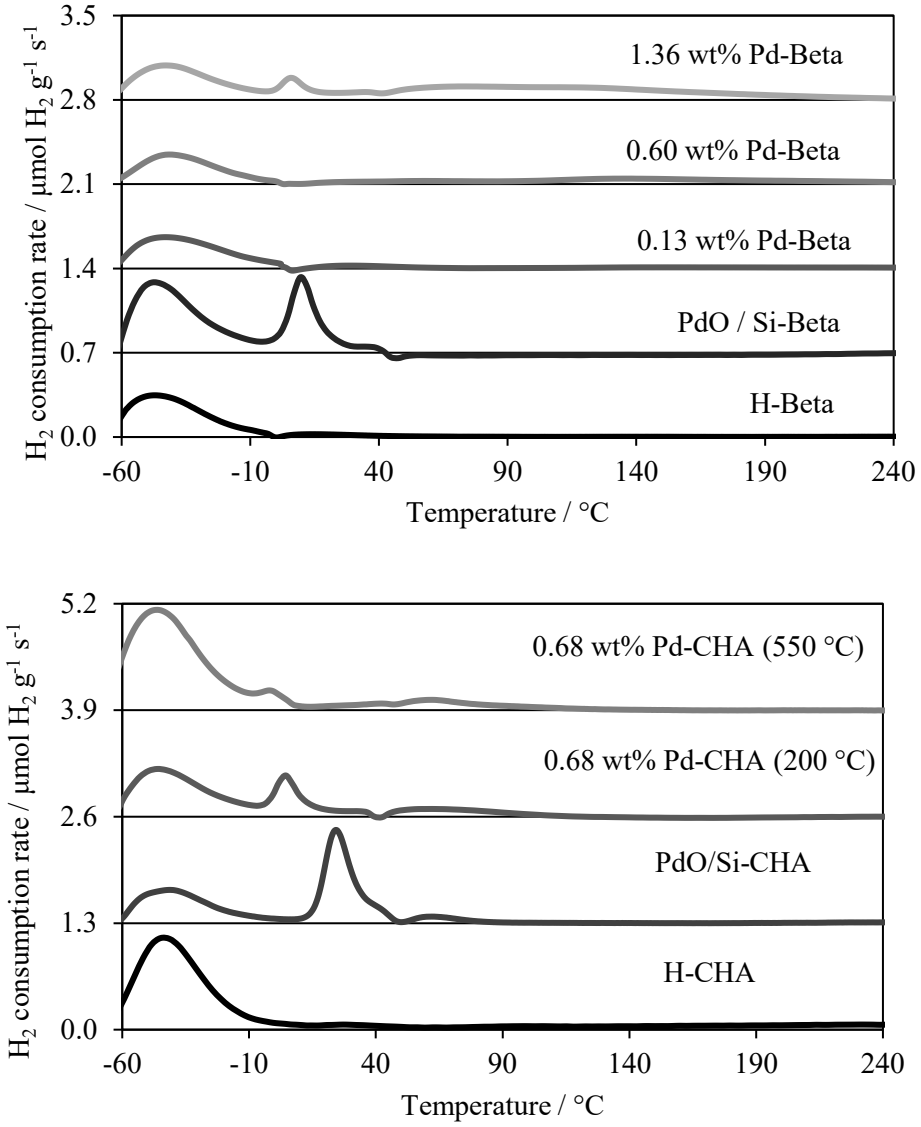

Figure A2.3. H_2 temperature-programmed reduction profiles of BEA (top) and CHA (bottom) zeolites pretreated in flowing air to 550 °C, unless otherwise indicated.

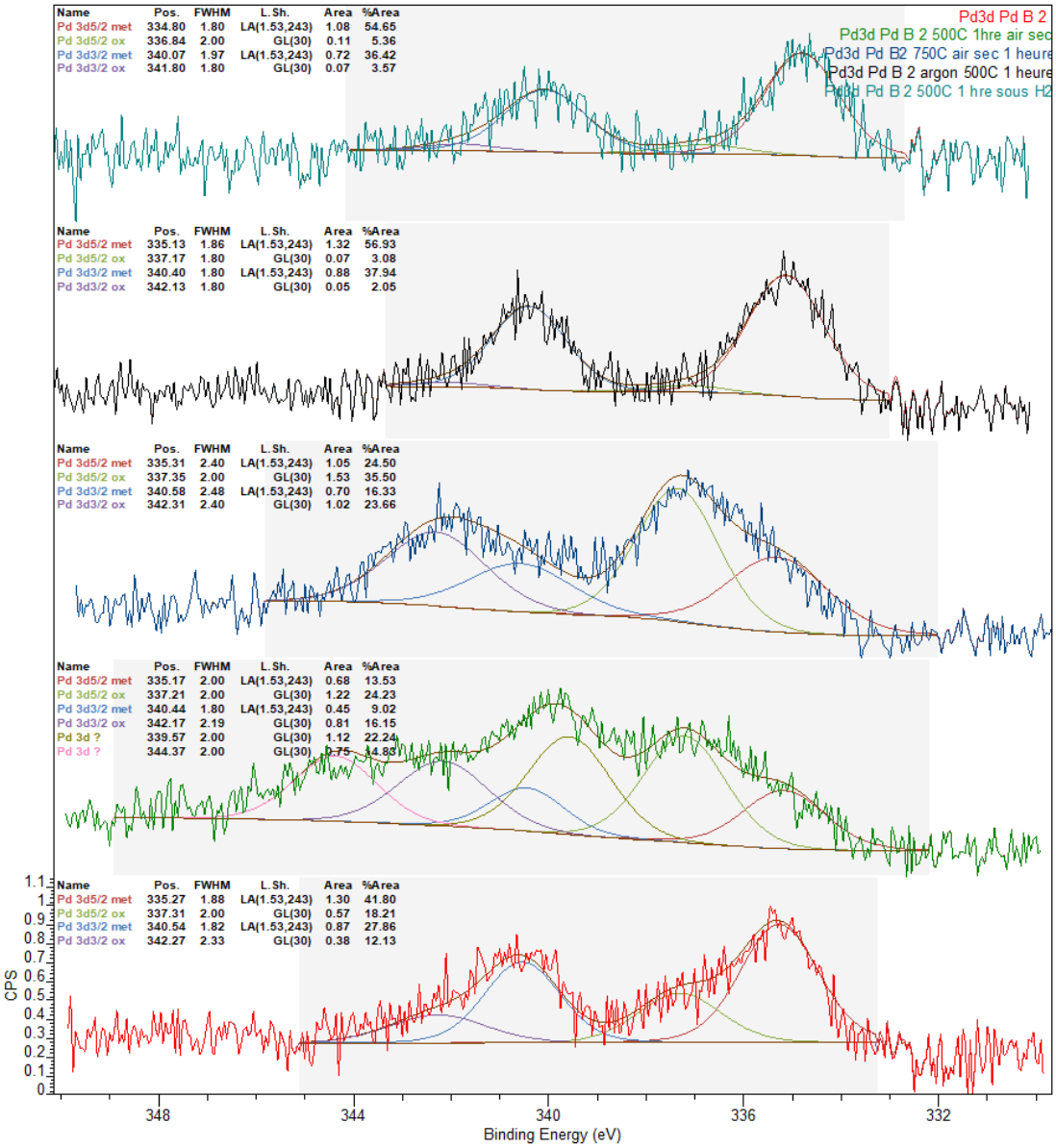

Figure S1. Deconvolution of in-situ XPS Pd 3d spectra for 1.4% Pd-BEA pretreated at 500 °C for 1 h in H_2 (top), pretreated at 500 °C in Ar for 1 h (2nd), pretreated at 750 °C in air for 1 h (3rd), pretreatment in air at 500 °C for 1 h (4th), material as-prepared (bottom).

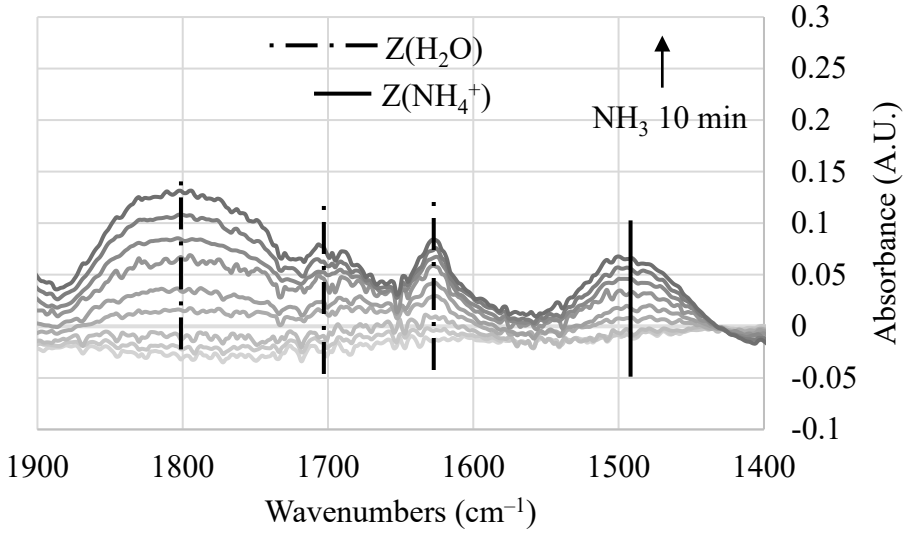

Figure S2. H-BEA: DRIFT spectra of the NH_4^+ region after pretreatment at 500 °C for 1 h with Ar rigorously dried by cold trap. The material was cooled to 25 °C prior to the adsorption of 1% NH_3 for ten minutes.

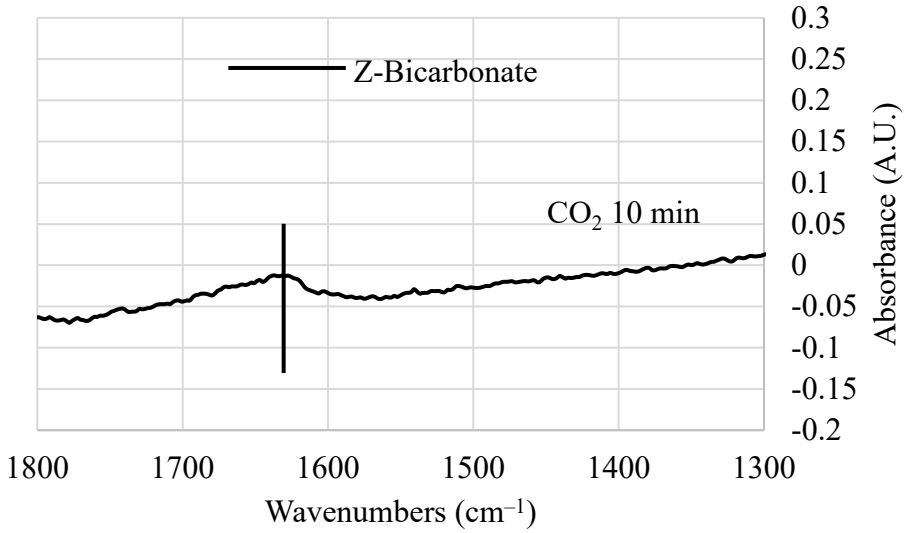

Figure S3. H-BEA: DRIFT spectrum of the carbonate region after pretreatment at 500 °C for 1 h with Ar rigorously dried by cold trap. The material was cooled to 25 °C prior to the adsorption of 1% CO_2 for ten minutes.

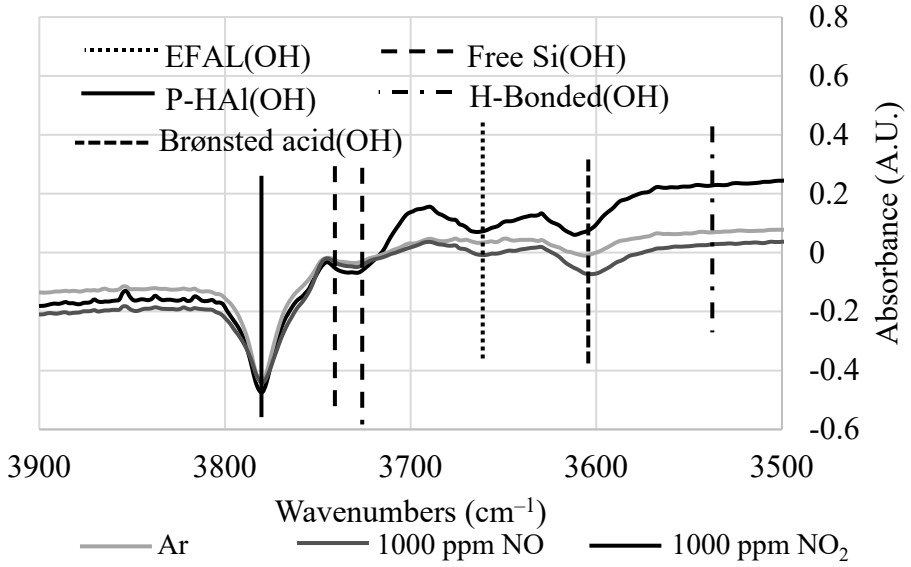

Figure S4 1.4% Pd-BEA: DRIFT spectra of NO_2 adsorption after pretreatment at 500 °C for 1 h with rigorously dried Ar, 1000 ppm NO in Ar or 1000 ppm NO_2 in Ar. NO_2 was adsorbed for 10 minutes at 50 °C.

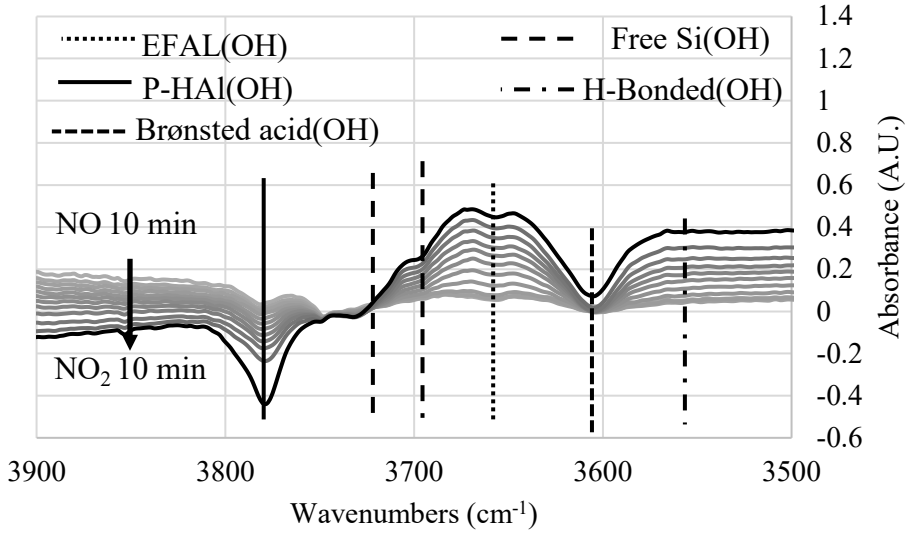

Figure S5. DRIFTS spectra of NO-NO_2 sequential adsorption after pretreatment at 500 °C for 1 h with 10% H_2. NO was adsorbed for 10 minutes at 100 °C followed by NO_2 adsorption for 10 minutes. Time-resolved spectra of NO_2 adsorption at 100 °C are shown, the black spectrum being that collected after Ar purge for 10 min.

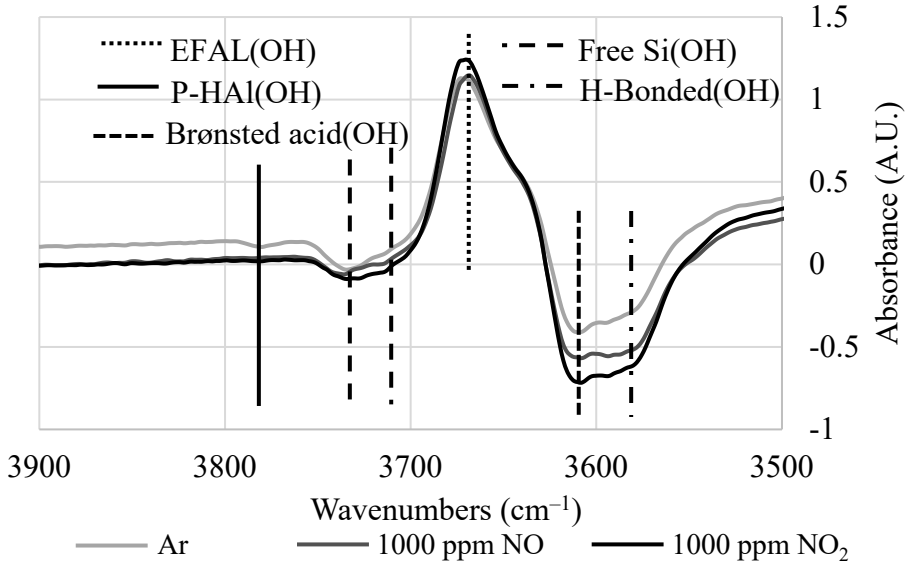

Figure S6. 0.7% Pd-CHA: DRIFT spectra of NO_2 adsorption after pretreatment at 500 °C for 1 h with rigorously dried Ar, 1000 ppm NO in Ar or 1000 ppm NO_2 in Ar. NO_2 was adsorbed for 10 minutes at 50 °C.

REFERENCES

1. EPA, U. S. Federal and California Light-Duty Vehicle Emissions Standards for Air Pollutants. https://19january2017snapshot.epa.gov/sites/production/files/2016-02/documents/420f16002.pdf (accessed 2-24-2019).
2. Johnson, T.; Joshi, A., Review of vehicle engine efficiency and emissions. *SAE Int. J. Engines* **2018,** *11* (2018-01-0329).
3. EPA, U. S. Nitrogen Oxides (NO_x), Why and How They Are Controlled. Nitrogen Oxides (NOx), Why and How They Are Controlled (accessed 2-24-2019).
4. Brandenberger, S.; Kröcher, O.; Tissler, A.; Althoff, R., The state of the art in selective catalytic reduction of NO_x by Ammonia using metal-exchanged zeolite catalysts. *Catal. Rev.* **2008,** *50* (4), 492-531.
5. Schmieg, S. J.; Oh, S. H.; Kim, C. H.; Brown, D. B.; Lee, J. H.; Peden, C. H.; Kim, D. H., Thermal durability of Cu-CHA NH_3-SCR catalysts for diesel NO_x reduction. *Catal. Today* **2012,** *184* (1), 252-261.
6. Russell, A.; Epling, W. S., Diesel oxidation catalysts. *Catal. Rev.* **2011,** *53* (4), 337-423.
7. Wang, J.; Crocker, M., N_2O Mitigation in a Coupled LNT–SCR System. *Catal. Lett.* **2012,** *142* (10), 1167-1174.
8. Koebel, M.; Elsener, M.; Kleemann, M., Urea-SCR: a promising technique to reduce NO_x emissions from automotive diesel engines. *Catal. Today* **2000,** *59* (3-4), 335-345.
9. Li, J.; Chang, H.; Ma, L.; Hao, J.; Yang, R. T., Low-temperature selective catalytic reduction of NO_x with NH_3 over metal oxide and zeolite catalysts—A review. *Catal. Today* **2011,** *175* (1), 147-156.
10. Long, R. Q.; Yang, R. T., Superior Fe-ZSM-5 catalyst for selective catalytic reduction of nitric oxide by ammonia. *J. Am. Chem. Soc.* **1999,** *121* (23), 5595-5596.
11. Tang, X.; Hao, J.; Xu, W.; Li, J., Low temperature selective catalytic reduction of NO_x with NH_3 over amorphous MnO_x catalysts prepared by three methods. *Catal. Commun.* **2007,** *8* (3), 329-334.
12. Tang, X.; Li, J.; Sun, L.; Hao, J., Origination of N_2O from NO reduction by NH_3 over β-MnO_2 and α-Mn_2O_3. *Appl. Catal., B* **2010,** *99* (1-2), 156-162.
13. Kang, M.; Park, E. D.; Kim, J. M.; Yie, J. E., Cu–Mn mixed oxides for low temperature NO reduction with NH_3. *Catal. Today* **2006,** *111* (3-4), 236-241.
14. Qi, G.; Yang, R. T.; Chang, R., MnO_x-CeO_2 mixed oxides prepared by co-precipitation for selective catalytic reduction of NO with NH_3 at low temperatures. *Appl. Catal., B* **2004,** *51* (2), 93-106.
15. Long, R. Q.; Yang, R. T., Fe-ZSM-5 for selective catalytic reduction of NO with NH_3: a comparative study of different preparation techniques. *Catal. Lett.* **2001,** *74* (3-4), 201-205.
16. Liu, Z.; Millington, P. J.; Bailie, J. E.; Rajaram, R. R.; Anderson, J. A., A comparative study of the role of the support on the behaviour of iron based ammonia SCR catalysts. *Microporous Mesoporous Materials* **2007,** *104* (1-3), 159-170.
17. Choi, E.-Y.; Nam, I.-S.; Kim, Y. G., TPD study of mordenite-type zeolites for selective catalytic reduction of NO by NH_3. *J. Catal.* **1996,** *161* (2), 597-604.

18. Ma, A.-Z.; Grünert, W., Selective catalytic reduction of NO by ammonia over Fe-ZSM-5 catalysts. *Chem. Commun.* **1999,** (1), 71-72.
19. Park, J.-H.; Park, H. J.; Baik, J. H.; Nam, I.-S.; Shin, C.-H.; Lee, J.-H.; Cho, B. K.; Oh, S. H., Hydrothermal stability of Cu-ZSM-5 catalyst in reducing NO by NH_3 for the urea selective catalytic reduction process. *J. Catal.* **2006,** *240* (1), 47-57.
20. Richter, M.; Trunschke, A.; Bentrup, U.; Brzezinka, K.-W.; Schreier, E.; Schneider, M.; Pohl, M.-M.; Fricke, R., Selective catalytic reduction of nitric oxide by ammonia over egg-shell MnO_x/NaY composite catalysts. *J. Catal.* **2002,** *206* (1), 98-113.
21. Iwasaki, M.; Yamazaki, K.; Banno, K.; Shinjoh, H., Characterization of Fe-ZSM-5 $DeNO_x$ catalysts prepared by different methods: Relationships between active Fe sites and NH_3-SCR performance. *J. Catal.* **2008,** *260* (2), 205-216.
22. Kumar, M. S.; Schwidder, M.; Grünert, W.; Bentrup, U.; Brückner, A., Selective reduction of NO with Fe-ZSM-5 catalysts of low Fe content: Part II. Assessing the function of different Fe sites by spectroscopic in situ studies. *J. Catal.* **2006,** *239* (1), 173-186.
23. Madia, G.; Koebel, M.; Elsener, M.; Wokaun, A., The effect of an oxidation precatalyst on the NO_x reduction by ammonia SCR. *Ind. Eng. Chem. Res.* **2002,** *41* (15), 3512-3517.
24. Forzatti, P.; Lietti, L., The reduction of NO_x stored on LNT and combined LNT–SCR systems. *Catal. Today* **2010,** *155* (1-2), 131-139.
25. Corbos, E.; Elbouazzaoui, S.; Courtois, X.; Bion, N.; Marecot, P.; Duprez, D., NO_x storage capacity, SO_2 resistance and regeneration of Pt/Ba/CeZr model catalysts for NO_x-trap system. *Top. Catal.* **2007,** *42* (1-4), 9-13.
26. Ohtsuka, H., The selective catalytic reduction of nitrogen oxides by methane on noble metal-loaded sulfated zirconia. *Appl. Catal., B* **2001,** *33* (4), 325-333.
27. Epling, W. S.; Campbell, L. E.; Yezerets, A.; Currier, N. W.; Parks, J. E., Overview of the fundamental reactions and degradation mechanisms of NO_x storage/reduction catalysts. *Catal. Rev.* **2004,** *46* (2), 163-245.
28. Ji, Y.; Toops, T. J.; Pihl, J. A.; Crocker, M., NO_x storage and reduction in model lean NO_x trap catalysts studied by in-situ DRIFTS. *Appl. Catal., B* **2009,** *91* (1-2), 329-338.
29. Olsson, L.; Fridell, E., The influence of Pt oxide formation and Pt dispersion on the reactions $NO_2 \Leftrightarrow NO + 1/2O_2$ over Pt/Al_2O_3 and $Pt/BaO/Al_2O_3$. *J. Catal.* **2002,** *210* (2), 340-353.
30. Olsson, L.; Fridell, E.; Skoglundh, M.; Andersson, B., Mean field modelling of NO_x storage on $Pt/BaO/Al_2O_3$. *Catal. Today* **2002,** *73* (3-4), 263-270.
31. Cant, N. W.; Patterson, M. J., The storage of nitrogen oxides on alumina-supported barium oxide. *Catal. Today* **2002,** *73* (3-4), 271-278.
32. Hodjati, S.; Vaezzadeh, K.; Petit, C.; Pitchon, V.; Kiennemann, A., NO_x sorption–desorption study: application to diesel and lean-burn exhaust gas (selective NO_x recirculation technique). *Catal. Today* **2000,** *59* (3-4), 323-334.
33. Mahzoul, H.; Brilhac, J.; Gilot, P., Experimental and mechanistic study of NO_x adsorption over NO_x trap catalysts. *Appl. Catal., B* **1999,** *20* (1), 47-55.
34. Fridell, E.; Skoglundh, M.; Westerberg, B.; Johansson, S.; Smedler, G., NO_x Storage in Barium-Containing Catalysts. *J. Catal.* **1999,** *183* (2), 196-209.

35. Lietti, L.; Forzatti, P.; Nova, I.; Tronconi, E., NO_x Storage Reduction over Pt/Ba/γ-Al2O3 Catalyst. *J. Catal.* **2001,** *204* (1), 175-191.
36. Erkfeldt, S.; Jobson, E.; Larsson, M., The effect of carbon monoxide and hydrocarbons on NO_x storage at low temperature. *Top. Catal.* **2001,** *16* (1-4), 127-131.
37. Wang, J.; Ji, Y.; Jacobs, G.; Jones, S.; Kim, D. J.; Crocker, M., Effect of aging on NO_x reduction in coupled LNT–SCR systems. *Appl. Catal., B* **2014,** *148*, 51-61.
38. Wang, J.; Ji, Y.; He, Z.; Crocker, M.; Dearth, M.; McCabe, R. W., A non-NH_3 pathway for NO_x conversion in coupled LNT-SCR systems. *Appl. Catal., B* **2012,** *111*, 562-570.
39. Xu, L.; Lupescu, J.; Ura, J.; Harwell, A.; Paxton, W. A.; Nunan, J.; Alltizer, C., Benefits of Pd Doped Zeolites for Cold Start HC/NO_x Emission Reductions for Gasoline and E-85 Fueled Vehicles. *SAE Int. J. Fuels* **2018,** *11* (2018-01-0948), 301-317.
40. Kašpar, J.; Fornasiero, P.; Hickey, N., Automotive catalytic converters: current status and some perspectives. *Catal. Today* **2003,** *77* (4), 419-449.
41. Koltsakis, G. C.; Stamatelos, A. M., Catalytic automotive exhaust aftertreatment. *Progress in Energy Combustion Science* **1997,** *23* (1), 1-39.
42. Kruse, N.; Frennet, A.; Bastin, J.-M., *Catalysis and Automotive Pollution Control IV*. Elsevier: 1998; Vol. 116.
43. Diwell, A.; Rajaram, R.; Shaw, H.; Truex, T., The role of ceria in three-way catalysts. In *Stud. Surf. Sci. Catal.*, Elsevier: 1991; Vol. 71, pp 139-152.
44. Engler, B.; Lox, E.; Ostgathe, K.; Ohata, T.; Tsuchitani, K.; Ichihara, S.; Onoda, H.; Garr, G.; Psaras, D. *Recent trends in the application of tri-metal emission control catalysts*; 0148-7191; SAE Technical Paper: 1994.
45. Taylor, K. C., Automobile catalytic converters. In *Catalysis*, Springer: 1984; pp 119-170.
46. Taylor, K. C., Nitric oxide catalysis in automotive exhaust systems. *Catal. Rev.* **1993,** *35* (4), 457-481.
47. Di Monte, R.; Fornasiero, P.; Kašpar, J.; Graziani, M.; Gatica, J.; Bernal, S.; Gómez-Herrero, A., Stabilisation of nanostructured Ce(0.2)Zr(0.8)O_2 solid solution by impregnation on Al_2O_3: a suitable method for the production of thermally stable oxygen storage/release promoters for three-way catalysts. *Chem. Commun.* **2000,** (21), 2167-2168.
48. Root, T.; Schmidt, L.; Fisher, G. B., Adsorption and reaction of nitric oxide and oxygen on Rh (111). *Surf. Sci.* **1983,** *134* (1), 30-45.
49. Campbell, C. T.; White, J., Chemisorption and reactions of nitric oxide on rhodium. *App. Surf. Sci.* **1978,** *1* (3), 347-359.
50. Baird, R.; Ku, R.; Wynblatt, P., The chemisorption of CO and NO on Rh (110). *Surf. Sci.* **1980,** *97* (2-3), 346-362.
51. Oh, S. H.; Fisher, G. B.; Carpenter, J. E.; Goodman, D. W., Comparative kinetic studies of CO* O_2 and CO* NO reactions over single crystal and supported rhodium catalysts. *J. Catal.* **1986,** *100* (2), 360-376.
52. Oh, S. H.; Carpenter, J. E., Platinum-rhodium synergism in three-way automotive catalysts. *J. Catal.* **1986,** *98* (1), 178-190.
53. Heck, R. M.; Farrauto, R. J.; Gulati, S. T., *Catalytic air pollution control: commercial technology*. John Wiley & Sons: 2009.

54. Argyle, M.; Bartholomew, C., Heterogeneous catalyst deactivation and regeneration: a review. *Catalysts* **2015,** *5* (1), 145-269.
55. Boaro, M.; de Leitenburg, C.; Dolcetti, G.; Trovarelli, A.; Graziani, M., Oxygen storage behavior of ceria–zirconia-based catalysts in the presence of SO_2. *Top. Catal.* **2001,** *16* (1-4), 299-306.
56. EPA, U. S. Report on the Environment https://cfpub.epa.gov/roe/indicator_pdf.cfm?i=15 (accessed 3-4-2019).
57. Cole, J. A., System for reducing NO_x from mobile source engine exhaust. Google Patents: 1997.
58. Lee, J.; Theis, J. R.; Kyriakidou, E. A., Vehicle emissions trapping materials: Successes, challenges, and the path forward. *Appl. Catal., B* **2018**.
59. Gu, Y.; Epling, W. S., Passive NO_x adsorber: An overview of catalyst performance and reaction chemistry. *Appl. Catal., A* **2019,** *570*, 1-14.
60. Jarvis, M.; Adams, K. M., Method for converting exhaust gases from a diesel engine using nitrogen oxide absorbent. Google Patents: 2001.
61. Melville, J. E.; Brisley, R. J.; Keane, O.; Phillips, P. R.; Mountstevens, E. H., Thermally regenerable nitric oxide adsorbent. Google Patents: 2012.
62. Jones, S.; Ji, Y.; Crocker, M., Ceria-based Catalysts for Low Temperature NO_x storage and Release. *Catal. Lett.* **2016,** *146* (5), 909-917.
63. Jones, S.; Ji, Y.; Bueno-Lopez, A.; Song, Y.; Crocker, M., CeO_2-M_2O_3 passive NO_x adsorbers for cold start applications. *Emiss. Control Sci. Technol.* **2017,** *3* (1), 59-72.
64. Ji, Y.; Bai, S.; Crocker, M., Al_2O_3-based passive NO_x adsorbers for low temperature applications. *Appl. Catal., B* **2015,** *170*, 283-292.
65. Ji, Y.; Bai, S.; Xu, D.; Qian, D.; Wu, Z.; Song, Y.; Pace, R.; Crocker, M.; Wilson, K.; Lee, A., Pd-promoted WO_3-ZrO_2 for low temperature NO_x storage. *Appl. Catal., B* **2020,** *264*, 118499.
66. Tamm, S.; Andonova, S.; Olsson, L., Silver as storage compound for NO_x at low temperatures. *Catal. Lett.* **2014,** *144* (4), 674-684.
67. Ji, Y.; Xu, D.; Crocker, M.; Theis, J. R.; Lambert, C.; Bueno-Lopez, A.; Harris, D.; Scapens, D., Mn-based mixed oxides for low temperature NO_x adsorber applications. *Appl. Catal., A* **2018,** *567*, 90-101.
68. Ji, Y.; Xu, D.; Bai, S.; Graham, U.; Crocker, M.; Chen, B.; Shi, C.; Harris, D.; Scapens, D.; Darab, J., Pt-and Pd-promoted CeO_2–ZrO_2 for passive NO_x adsorber applications. *Ind. Eng. Chem. Res.* **2017,** *56* (1), 111-125.
69. Theis, J. R., An assessment of Pt and Pd model catalysts for low temperature NO_x adsorption. *Catal. Today* **2016,** *267*, 93-109.
70. Ryou, Y.; Lee, J.; Lee, H.; Kim, C. H.; Kim, D. H., Low temperature NO adsorption over hydrothermally aged Pd/CeO_2 for cold start application. *Catal. Today* **2018,** *307*, 93-101.
71. Ryou, Y.; Lee, J.; Lee, H.; Kim, C. H.; Kim, D. H., Effect of sulfur aging and regeneration on low temperature NO adsorption over hydrothermally treated Pd/CeO_2 and Pd/Ce(0.58)Zr(0.42)O_2 catalysts. *Catal. Today* **2017,** *297*, 53-59.
72. Khivantsev, K.; Jaegers, N. R.; Kovarik, L.; Hanson, J. C.; Tao, F.; Tang, Y.; Zhang, X.; Koleva, I. Z.; Aleksandrov, H. A.; Vayssilov, G. N., Achieving Atomic Dispersion of Highly Loaded Transition Metals in Small-Pore Zeolite SSZ-13: High-

Capacity and High-Efficiency Low-Temperature CO and Passive NO_x Adsorbers. *Angew. Chem. Int. Ed.* **2018,** *57* (51), 16672-16677.
73. Song, J.; Wang, Y.; Walter, E. D.; Washton, N. M.; Mei, D.; Kovarik, L.; Engelhard, M. H.; Prodinger, S.; Wang, Y.; Peden, C. H., Toward rational design of Cu/SSZ-13 selective catalytic reduction catalysts: implications from atomic-level understanding of hydrothermal stability. *ACS Catal.* **2017,** *7* (12), 8214-8227.
74. Khivantsev, K.; Jaegers, N. R.; Koleva, I. Z.; Aleksandrov, H. A.; Kovarik, L.; Engelhard, M. H.; Gao, F.; Wang, Y.; Vayssilov, G. N.; Szanyi, J., Stabilization of super electrophilic Pd^{+2} cations in small-pore SSZ-13 zeolite. *J. Phys. Chem. C.* **2019,** *124* (1), 309-321.
75. Stokes, L. S.; Murphy, D. M.; Farley, R. D.; Rowlands, C. C.; Bailey, S., EPR investigation of Pd I species in palladium-exchanged ZSM-5 and beta zeolites. *Phys. Chem. Chem. Phys.* **1999,** *1* (4), 621-628.
76. Zheng, Y.; Kovarik, L.; Engelhard, M. H.; Wang, Y.; Wang, Y.; Gao, F.; Szanyi, J., Low-Temperature Pd/Zeolite Passive NO_x Adsorbers: Structure, Performance, and Adsorption Chemistry. *J. Phys. Chem. C.* **2017,** *121* (29), 15793-15803.
77. Baerlocher, C.; McCusker, L. Database of Zeolite Structures. http://www.iza-structure.org/databases.
78. Naccache, C.; Primet, M.; Mathieu, M., Study of hydrogen and carbon monoxide interactions with palladium-Y zeolite by ESR and IR Spectroscopy. ACS Publications: 1973.
79. Romotowski, T.; Komorek, J.; Paukshtis, Y. A.; Yurchenko, E., Al-Na-ZSM-5 zeolites. Part 2. A study with IR spectra of adsorbed CO. *Zeolites* **1991,** *11* (5), 497-501.
80. Willner, H.; Bodenbinder, M.; Bröchler, R.; Hwang, G.; Rettig, S. J.; Trotter, J.; von Ahsen, B.; Westphal, U.; Jonas, V.; Thiel, W., Superelectrophilic tetrakis (carbonyl) palladium (II)-and-platinum (II) undecafluorodiantimonate (V),$[Pd(CO)_4][Sb_2F_{11}]_2$ and $[Pt(CO)_4][Sb_2F_{11}]_2$: syntheses, physical and spectroscopic properties, their crystal, molecular, and extended structures, and density functional calculations: an experimental, computational, and comparative study. *J. Am. Chem. Soc.* **2001,** *123* (4), 588-602.
81. Taarit, Y. B.; Vedrine, J.; Dutel, J.; Naccache, C., EPR investigation of the structure and reactivity of Pd (I) species generated in synthetic mordenite-type zeolite. *J. Magn. reson.* **1978,** *31* (2), 251-257.
82. Aylor, A. W.; Lobree, L. J.; Reimer, J. A.; Bell, A. T., Investigations of the Dispersion of Pd in H-ZSM-5. *J. Catal.* **1997,** *172* (2), 453-462.
83. Khivantsev, K.; Gao, F.; Kovarik, L.; Wang, Y.; Szanyi, J., Molecular Level Understanding of How Oxygen and Carbon Monoxide Improve NO_x Storage in Palladium/SSZ-13 Passive NO_x Adsorbers: The Role of NO^+ and Pd-(II)(CO)(NO) Species. *J. Phys. Chem. C.* **2018,** *122* (20), 10820-10827.
84. Sheu, L.; Knözinger, H.; Sachtler, W., Ship-in-a-bottle formation of $Pd_{13}(CO)_x$ clusters in zeolite Na-Y. *Catal. Lett.* **1989,** *2* (3), 129-137.
85. Aleksandrov, H. A.; Neyman, K. M.; Vayssilov, G. N., The structure and stability of reduced and oxidized mononuclear platinum species on nanostructured ceria from density functional modeling. *Phys. Chem. Chem. Phys.* **2015,** *17* (22), 14551-14560.

86. Aleksandrov, H. A.; Neyman, K. M.; Hadjiivanov, K. I.; Vayssilov, G. N., Can the state of platinum species be unambiguously determined by the stretching frequency of an adsorbed CO probe molecule? *Phys. Chem. Chem. Phys.* **2016,** *18* (32), 22108-22121.
87. Rivallan, M.; Seguin, E.; Thomas, S.; Lepage, M.; Takagi, N.; Hirata, H.; Thibault-Starzyk, F., Platinum Sintering on H-ZSM-5 Followed by Chemometrics of CO Adsorption and 2D Pressure-Jump IR Spectroscopy of Adsorbed Species. *Angew. Chem. Int. Ed.* **2010,** *49* (4), 785-789.
88. Bisio, C.; Martra, G.; Coluccia, S.; Massiani, P., FT-IR evidence of two distinct protonic sites in BEA zeolite: consequences on cationic exchange and on acido-basic properties in the presence of cesium. *J. Phys. Chem. C.* **2008,** *112* (28), 10520-10530.
89. Hadjiivanov, K.; Klissurski, D.; Ramis, G.; Busca, G., Fourier transform IR study of NO_x adsorption on a Cu-ZSM-5 $DeNO_x$ catalyst. *Appl. Catal., B* **1996,** *7* (3-4), 251-267.
90. Descorme, C.; Gelin, P.; Primet, M.; Lécuyer, C., Infrared study of nitrogen monoxide adsorption on palladium ion-exchanged ZSM-5 catalysts. *Catal. Lett.* **1996,** *41* (3-4), 133-138.
91. Mihai, O.; Trandafilović, L.; Wentworth, T.; Torres, F. F.; Olsson, L., The Effect of Si/Al Ratio for Pd/BEA and Pd/SSZ-13 Used as Passive NO_x Adsorbers. *Top. Catal.* **2018**.
92. Hadjiivanov, K., Use of overtones and combination modes for the identification of surface NO_x anionic species by IR spectroscopy. *Catal. Lett.* **2000,** *68* (3-4), 157-161.
93. Hess, C.; Ozensoy, E.; Yi, C.-W.; Goodman, D. W., NO dimer and dinitrosyl formation on Pd (111): From ultra-high-vacuum to elevated pressure conditions. *J. Am. Chem. Soc.* **2006,** *128* (9), 2988-2994.
94. Khivantsev, K.; Jaegers, N. R.; Kovarik, L.; Prodinger, S.; Derewinski, M. A.; Wang, Y.; Gao, F.; Szanyi, J., Palladium/Beta zeolite passive NO_x adsorbers (PNA): Clarification of PNA chemistry and the effects of CO and zeolite crystallite size on PNA performance. *Appl. Catal., A* **2019,** *569*, 141-148.
95. Pommier, B.; Gelin, P., Infrared and volumetric study of NO adsorption on Pd-H-ZSM-5. *Phys. Chem. Chem. Phys.* **2001,** *3* (6), 1138-1143.
96. Pozdnyakov, D.; Filimonov, V., Infrared spectroscopic study of the chemisorption of nitric oxide and nitrogen dioxide on metal oxides. *Kinet. Catal.* **1973,** *14*, 760-766.
97. Theis, J. R.; Lambert, C., The Effects of CO, C_2H_4, and H_2O on the NO_x Storage Performance of Low Temperature NO_x Adsorbers for Diesel Applications. *SAE Int. J. Engines* **2017,** *10* (4), 1627-1637.
98. Ryou, Y.; Lee, J.; Cho, S. J.; Lee, H.; Kim, C. H.; Kim, D. H., Activation of Pd/SSZ-13 catalyst by hydrothermal aging treatment in passive NO adsorption performance at low temperature for cold start application. *Appl. Catal., B* **2017,** *212*, 140-149.
99. Pommier, B.; Gélin, P., On the nature of Pd species formed upon exchange of H-ZSM-5 with $Pd(NH_3)_4{}^{2+}$ and calcination in O_2. *Phys. Chem. Chem. Phys.* **1999,** *1* (7), 1665-1672.
100. Ryou, Y.; Lee, J.; Lee, H.; Kim, C. H.; Kim, D. H., Effect of various activation conditions on the low temperature NO adsorption performance of Pd/SSZ-13 passive NO_x adsorber. *Catal. Today* **2019,** *320*, 175-180.

101. Chen, H.-Y.; Mulla, S.; Weigert, E.; Camm, K.; Ballinger, T.; Cox, J.; Blakeman, P., Cold Start Concept (CSC™) A Novel Catalyst for Cold Start Emission Control. *SAE Int. J. Fuels* **2013,** *6* (2), 372-381.
102. Chen, H.-Y.; Collier, J. E.; Liu, D.; Mantarosie, L.; Durán-Martín, D.; Novák, V.; Rajaram, R. R.; Thompsett, D., Low Temperature NO Storage of Zeolite Supported Pd for Low Temperature Diesel Engine Emission Control. *Catal. Lett.* **2016,** *146* (9), 1706-1711.
103. Vu, A.; Luo, J.; Li, J.; Epling, W. S., Effects of CO on Pd/BEA Passive NO_x Adsorbers. *Catal. Lett.* **2017,** *147* (3), 745-750.
104. Yakerson, V.; Rozanov, V. V.; Rubinshtein, A., Thermodesorption studies on adsorbate-adsorbent interaction. *Surf. Sci.* **1968,** *12* (2), 221-246.
105. Sedlmair, C.; Gil, B.; Seshan, K.; Jentys, A.; Lercher, J. A., An in-situ IR study of the NO_x adsorption/reduction mechanism on modified Y zeolites. *Phys. Chem. Chem. Phys.* **2003,** *5* (9), 1897-1905.
106. Perdana, I.; Creaser, D.; Öhrman, O.; Hedlund, J., NO_x adsorption over a wide temperature range on Na-ZSM-5 films. *J. Catal.* **2005,** *234* (1), 219-229.
107. Gu, Y.; Zelinsky, R. P.; Chen, Y.-R.; Epling, W. S., Investigation of an irreversible NO_x storage degradation Mode on a Pd/BEA passive NO_x adsorber. *Appl. Catal., B* **2019,** *258*, 118032.
108. Ryou, Y.; Lee, J.; Kim, Y.; Hwang, S.; Lee, H.; Kim, C. H.; Kim, D. H., Effect of reduction treatments (H_2 vs. CO) on the NO adsorption ability and the physicochemical properties of Pd/SSZ-13 passive NO_x adsorber for cold start application. *Appl. Catal., A* **2019,** *569*, 28-34.
109. Gupta, A.; Kang, S. B.; Harold, M. P., NO_x uptake and release on Pd/SSZ-13: Impact Of Feed composition and temperature. *Catal. Today* **2020**.
110. Colombo, M.; Nova, I.; Tronconi, E., Detailed kinetic modeling of the NH_3–NO/NO_2 SCR reactions over a commercial Cu-zeolite catalyst for Diesel exhausts after treatment. *Catal. Today* **2012,** *197* (1), 243-255.
111. Lee, J.; Ryou, Y.; Cho, S. J.; Lee, H.; Kim, C. H.; Kim, D. H., Investigation of the active sites and optimum Pd/Al of Pd/ZSM–5 passive NO adsorbers for the cold-start application: Evidence of isolated-Pd species obtained after a high-temperature thermal treatment. *Appl. Catal., B* **2018,** *226*, 71-82.
112. Porta, A.; Pellegrinelli, T.; Castoldi, L.; Matarrese, R.; Morandi, S.; Dzwigaj, S.; Lietti, L., Low Temperature NO_x Adsorption Study on Pd-Promoted Zeolites. *Top. Catal.* **2018,** *61* (18-19), 2021-2034.
113. Theis, J. R.; Lambert, C. K., Mechanistic assessment of low temperature NO_x adsorbers for cold start NO_x control on diesel engines. *Catal. Today* **2019,** *320*, 181-195.
114. Di Iorio, J. R.; Gounder, R., Controlling the isolation and pairing of aluminum in chabazite zeolites using mixtures of organic and inorganic structure-directing agents. *Chem. Mater.* **2016,** *28* (7), 2236-2247.
115. Di Iorio, J. R.; Nimlos, C. T.; Gounder, R., Introducing catalytic diversity into single-site chabazite zeolites of fixed composition via synthetic control of active site proximity. *ACS Catal.* **2017,** *7* (10), 6663-6674.
116. Homeyer, S.; Sachtler, W., Oxidative redispersion of palladium and formation of PdO particles in NaY: An Application of High Precision TPR. *Appl. Catal.* **1989,** *54* (1), 189-202.

117. Omegna, A.; Vasic, M.; van Bokhoven, J. A.; Pirngruber, G.; Prins, R., Dealumination and realumination of microcrystalline zeolite beta: an XRD, FTIR and quantitative multinuclear (MQ) MAS NMR study. *Phys. Chem. Chem. Phys.* **2004,** *6* (2), 447-452.
118. Fickel, D. W.; Lobo, R. F., Copper coordination in Cu-SSZ-13 and Cu-SSZ-16 investigated by variable-temperature XRD. *J. Phys. Chem. C.* **2010,** *114* (3), 1633-1640.
119. Kappers, M.; Van der Maas, J., Correlation between CO frequency and Pt coordination number. A DRIFT study on supported Pt catalysts. *Catal. Lett.* **1991,** *10* (5-6), 365-373.
120. Kiricsi, I.; Flego, C.; Pazzuconi, G.; Parker, W. J.; Millini, R.; Perego, C.; Bellussi, G., Progress toward understanding zeolite Beta acidity: an IR and ^{27}Al NMR spectroscopic study. *J. Phys. Chem.* **1994,** *98* (17), 4627-4634.
121. Paolucci, C.; Parekh, A. A.; Khurana, I.; Di Iorio, J. R.; Li, H.; Albarracin Caballero, J. D.; Shih, A. J.; Anggara, T.; Delgass, W. N.; Miller, J. T., Catalysis in a cage: condition-dependent speciation and dynamics of exchanged Cu cations in SSZ-13 zeolites. *J. Am. Chem. Soc.* **2016,** *138* (18), 6028-6048.
122. Adelman, B.; Sachtler, W., The effect of zeolitic protons on NO_x reduction over Pd/ZSM-5 catalysts. *Appl. Catal., B* **1997,** *14* (1-2), 1-11.
123. Claydon, M.; Sheppard, N., The nature of "A, B, C"-type infrared spectra of strongly hydrogen-bonded systems; pseudo-maxima in vibrational spectra. *J. Chem. Soc., D* **1969,** (23), 1431-1433.
124. Tiznado, H.; Fuentes, S.; Zaera, F., Infrared Study of CO Adsorbed on $Pd/Al_2O_3-ZrO_2$. Effect of Zirconia Added by Impregnation. *Langmuir* **2004,** *20* (24), 10490-10497.
125. Vannice, M.; Wang, S., Determination of IR extinction coefficients for linear-and bridged-bonded carbon monoxide on supported palladium. *J. Phys. Chem.* **1981,** *85* (17), 2543-2546.
126. Wang, Z.; Li, B.; Chen, M.; Weng, W.; Wan, H., Size and support effects for CO oxidation on supported Pd catalysts. *Sci. China Chem.* **2010,** *53* (9), 2047-2056.
127. Bortnovsky, O.; Sobalík, Z.; Wichterlová, B.; Bastl, Z., Structure of Al–Lewis Site in beta zeolite active in the Meerwein–Ponndorf–Verley reduction of ketone to alcohol. *J. Catal.* **2002,** *210* (1), 171-182.
128. Vimont, A.; Thibault-Starzyk, F.; Lavalley, J., Infrared spectroscopic study of the acidobasic properties of beta zeolite. *J. Phys. Chem. B.* **2000,** *104* (2), 286-291.
129. Xu, L.; Li, X.-S.; Crocker, M.; Zhang, Z.-S.; Zhu, A.-M.; Shi, C., A study of the mechanism of low-temperature SCR of NO with NH_3 on MnO_x/CeO_2. *J. Mol. Catal. A: Chem.* **2013,** *378*, 82-90.
130. Toops, T. J.; Crocker, M., New sulfur adsorbents derived from layered double hydroxides: II. DRIFTS study of COS and H_2S adsorption. *Appl. Catal., B* **2008,** *82* (3-4), 199-207.
131. Maache, M.; Janin, A.; Lavalley, J.; Joly, J.; Benazzi, E., Acidity of zeolites Beta dealuminated by acid leaching: An FTi. r. study using different probe molecules (pyridine, carbon monoxide). *Zeolites* **1993,** *13* (6), 419-426.
132. Artioli, N.; Lobo, R. F.; Iglesia, E., Catalysis by confinement: Enthalpic stabilization of NO oxidation transition states by microporororous and mesoporous siliceous materials. *J. Phys. Chem. C.* **2013,** *117* (40), 20666-20674.

VITA

ROBERT B. PACE III

EDUCATION

B.S. CHEMISTRY • MAY 2011 • EASTERN KENTUCKY UNIVERSITY
Richmond, Kentucky. American Chemical Society Certified Degree.

HIGH SCHOOL DIPLOMA• MAY 2005 • GEORGE ROGERS CLARK HIGH SCHOOL
Winchester, Kentucky

PROFESSIONAL POSITIONS HELD

ASSISTANT RESEARCH SCIENTIST • UNIVERSITY OF KENTUCKY CENTER FOR APPLIED ENERGY RESEARCH • 2013– 2016

TECHNICIAN • UNIVERSITY OF KENTUCKY CENTER FOR APPLIED ENERGY RESEARCH • 2011 – 2013

HONORS

2018 University of Kentucky College of Arts and Sciences Outstanding Teaching Assistant Award

2018 National Science Foundation Graduate Research Fellowship Honorable Mention

PUBLICATIONS

1. Mazzotta, M. G.; Pace, R. B.; Wallgren, B. N.; Morton, S. A.; Miller, K. M.; Smith, D. L., Direct Analysis in Real Time Mass Spectrometry (DART-MS) of Ionic Liquids. *J. Am. Soc. Mass Spectrom.* **2013**, *24*, 1616-1619.
2. Harman-Ware, A.; Crocker, M.; Pace, R.; Placido, A.; Morton, S., III; DeBolt, S., Characterization of Endocarp Biomass and Extracted Lignin Using Pyrolysis and Spectroscopic Methods. *Bioenergy Res.* **2014**, *8*, 1-19.
3. Santillan-Jimenez, E.; Perdu, M.; Pace, R.; Morgan, T.; Crocker, M., Activated Carbon, Carbon Nanofiber and Carbon Nanotube Supported Molybdenum Carbide Catalysts for the Hydrodeoxygenation of Guaiacol. *Catalysts* **2015**, *5*, 424.
4. Yao, S. G.; Meier, M. S.; Pace III, R. B.; Crocker, M., A comparison of the oxidation of lignin model compounds in conventional and ionic liquid solvents and application to the oxidation of lignin. *RSC Adv.* **2016**, *6*, 104742-104753.
5. Santillan-Jimenez, E.; Pace, R.; Marques, S.; Morgan, T.; McKelphin, C.; Mobley, J.; Crocker, M., Extraction, characterization, purification, and catalytic upgrading of algae lipids to fuel-like hydrocarbons. *Fuel* **2016**, *180*, 668-678.

6. Ligaba-Osena, A.; Hankoua, B.; DiMarco, K.; Pace, R.; Crocker, M.; McAtee, J.; Nagachar, N.; Tien, M.; Richard, T. L., Reducing biomass recalcitrance by heterologous expression of a bacterial peroxidase in tobacco (Nicotiana benthamiana). *Sci. Rep.* **2017**, *7*, 17104.
7. Loe, R.; Huff, K.; Walli, M.; Morgan, T.; Qian, D.; Pace, R.; Song, Y.; Isaacs, M.; Santillan-Jimenez, E.; Crocker, M. Effect of Pt Promotion on the Ni-Catalyzed Deoxygenation of Tristearin to Fuel-Like Hydrocarbons. *Catalysts* **2019**, 9, 200.
8. Loe, R.; Lavoignat, Y.; Maier, M.; Abdallah, M.; Morgan, T.; Qian, D.; Pace, R.; Santillan-Jimenez, E.; Crocker, M. Continuous Catalytic Deoxygenation of Waste Free Fatty Acid-Based Feeds to Fuel-Like Hydrocarbons Over a Supported Ni-Cu Catalyst. *Catalysts* **2019**, 9, 123.
9. Santillan-Jimenez, E.; Pace, R.; Morgan, T.; Behnke, C.; Sajkowski, D. J.; Lappas, A.; Crocker, M. Co-processing of hydrothermal liquefaction algal bio-oil and petroleum feedstock to fuel-like hydrocarbons via fluid catalytic cracking. *Fuel Process. Technol.* **2019**, 188, 164-171.
10. Mohler, D.; Wilson, M. H.; Kesner, S.; Schambach, J. Y.; Vaughan, D.; Frazar, M.; Stewart, J.; Groppo, J.; Pace, R.; Crocker, M. Beneficial re-use of industrial CO_2 emissions using microalgae: Demonstration assessment and biomass characterization. *Biores. Technol.* **2019**, 293, 122014.
11. Silva, G.C.R.; Qian, D.; Pace, R.; Heintz, O.; Caboche, G.; Santillan-Jimenez, E.; Crocker, M. Promotional Effect of Cu, Fe and Pt on the Performance of Ni/Al_2O_3 in the Deoxygenation of Used Cooking Oil to Fuel-Like Hydrocarbons. *Catalysts* **2020**, 10, 91.
12. Ji, Y., Bai, S., Xu, D., Qian, D., Wu, Z., Song, Y., Pace, R., Crocker, M., Wilson, K., Lee, A., Harris, D., Scapens, D. Pd-promoted WO_3-ZrO_2 for low temperature NO_x storage. *App. Cat. B* **2020**, 264, 118499.
13. Pace, R., Kesner, S., Santillan-Jimenez, E., Morgan, T., Frazar, M., Kelly, V., Zeller, A., Crocker, M. Evaluation of Near-ambient Algal Biomass Fractionation Conditions for Bioproduct Development. Accepted to *Biomass Convers. Biorefin.*, **2020**.
14. Pace, R., Lardinois, T., Ji, Y., Gounder, R., Heintz, O., Crocker, M. Effects of treatment conditions on Pd speciation in CHA and Beta zeolites for passive NO_x adsorption. Preparing for re-submission to *J. Phys. Chem. C*, **2020.**